CFD AND TECHNO-ECONOMIC MODELLING OF THE EFFECT OF FEED SPACER ON REVERSE OSMOSIS MEMBRANE PERFORMANCE

TOH KANG YANG

MASTER OF SCIENCE

UNIVERSITI MALAYSIA PAHANG

UNIVERSITI MALAYSIA PAHANG

DECLARATION OF THESIS AND COPYRIGHT

Author's Full Name : TOH KANG YANG

Date of Birth : 24/07/1994

Title : CFD AND TECHNO-ECONOMIC MODELLING OF THE
EFFECT OF FEED SPACER ON REVERSE OSMOSIS
MEMBRANE PERFORMANCE

Academic Session : SEMESTER 1 2020/2021

I declare that this thesis is classified as:

☐ CONFIDENTIAL (Contains confidential information under the Official
Secret Act 1997)*

☐ RESTRICTED (Contains restricted information as specified by the
organization where research was done)*

☑ OPEN ACCESS I agree that my thesis to be published as online open access
(Full Text)

I acknowledge that Universiti Malaysia Pahang reserves the following rights:

1. The Thesis is the Property of Universiti Malaysia Pahang
2. The Library of Universiti Malaysia Pahang has the right to make copies of the thesis for
the purpose of research only.
3. The Library has the right to make copies of the thesis for academic exchange.

Certified by:

_____   _____
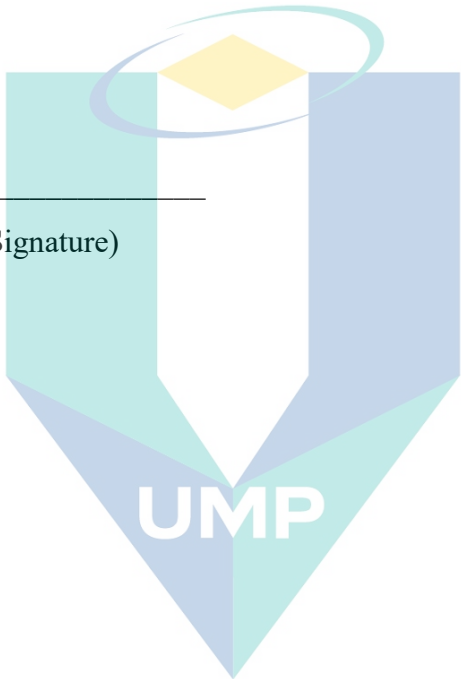(Student's Signature)   (Supervisor's Signature)

_____   _____
New IC/Passport Number   Name of Supervisor
Date: Date:

NOTE : * If the thesis is CONFIDENTIAL or RESTRICTED, please attach a thesis declaration letter.

SUPERVISOR'S DECLARATION

I hereby declare that I have checked this thesis and in my opinion, this thesis is adequate in terms of scope and quality for the award of the degree of Master of Science.

_____

(Supervisor's Signature)

Full Name   :

Position   :

Date   :

STUDENT'S DECLARATION

I hereby declare that the work in this thesis is based on my original work except for quotations and citations which have been duly acknowledged. I also declare that it has not been previously or concurrently submitted for any other degree at Universiti Malaysia Pahang or any other institutions.

_____

(Student's Signature)
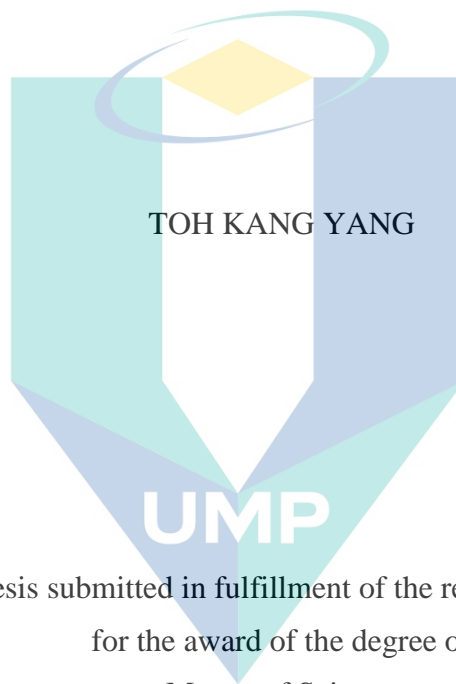
Full Name   :

ID Number   :

Date   :

CFD AND TECHNO-ECONOMIC MODELLING OF THE EFFECT OF FEED
SPACER ON REVERSE OSMOSIS MEMBRANE PERFORMANCE

TOH KANG YANG

Thesis submitted in fulfillment of the requirements
for the award of the degree of
Master of Science

College of Engineering

UNIVERSITI MALAYSIA PAHANG

OCTOBER 2020

ACKNOWLEDGEMENTS

I would like to thank the many people who made this thesis possible. First, I would like to thank my supervisor, Dr Liang Yong Yeow, for his great supervision and advice during my study. His knowledge and patience have inspired me a lot.

I would also like to thank my parents and friends for their support throughout my study. Through their encouragement, I can focus and complete this master study. I wish to thank Universiti Malaysia Pahang for their financial support throughout my study.
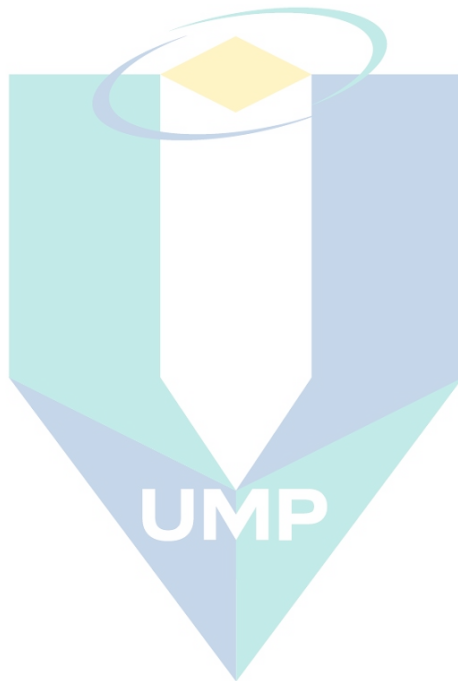
ABSTRAK

Proses osmosis berbalik (RO) merupakan salah satu cara penyahgaraman paling popular untuk air payau dan air laut. Salah satu isu utama dalam membran RO ialah polarisasi konsentrasi (CP). Memandangkan geometri peruang banyak mempengaruhi pengaliran air dan CP dalam membran *spiral wound* (SWM), usaha mengoptimumkan geometrinya tetap sebagai matlamat penyelidikan secara berterusan. Tesis ini mengkaji kesan geometri peruang kepada prestasi proses osmosis berbalik melalui Perkomputeran Dinamik Bendalir (CFD) dan pemodelan tekno-ekonomi. Bagi penyelidikan melalui CFD, dua reka bentuk geometri peruang telah dipertimbangkan, iaitu: 1) peruang berlubang dan 2) peruang dengan ciri-ciri "terapung". Hasil kajian utama daripada peruang berlubang adalah pendekatan ini tidak dapat meningkatkan fluks untuk semua kes simulasi menggunakan peruang konvensional. Analisis ini juga menunjukkan bahawa peruang yang berlubang lebih besar menurunkan pemindahan jisim melebihi 10% disebabkan oleh aliran kadar halaju yang lebih lemah dan penahanan penumpahan pusaran. Keputusan simulasi juga menunjukkan bahawa nisbah keapungan bukan faktor penentu bagi peningkatan pemindahan jisim. Ini adalah kerana mekanisme pemindahan jisim lebih bergantung pada ciri-ciri geometri yang lain, seperti reka bentuk peruang dengan 2 atau 3-lapisan. Simulasi tekno-ekonomi menunjukkan bahawa peruang maju lebih berkesan berbanding dengan peruang konvensional dalam meningkatkan fluks di kawasan berhampiran dengan salur masuk bagi membran berketertelapan tinggi. Ini adalah disebabkan oleh penurunan aliran air yang cepat sepanjang saluran. Tesis ini mendapati bahawa peningkatan ketertelapan membran (setinggi $10 \ \mathrm{L \ m^{-2} \ h^{-1} \ bar^{-1}}$) boleh mengurangkan jumlah kos pemprosesan untuk osmosis berbalik air laut (SWRO) dan air payau (BWRO) sebanyak 7.5% dan 32% masing-masing, tanpa mengira jenis peruang yang digunakan. Hasil kajian utama daripada analisis tekno-ekonomi adalah bahawa penambahbaikan reka bentuk peruang adalah lebih penting daripada peningkatan ketelapan membran pada pemulihan air yang sama.

ABSTRACT

Reverse osmosis (RO) processes are among the most popular solutions for brackish water and seawater desalination. One of the major issue faced in RO membrane is concentration polarisation (CP). As feed spacer geometry has major impacts on the flow and CP in the spiral wound membrane (SWM), optimizing its geometry remains an ongoing research goal. This thesis systematically investigates the effect of feed spacer geometry on RO membrane performance through computational fluid dynamics (CFD) and techno-economic modelling. For CFD study, two different spacer designs are considered: 1) spacer with perforations and 2) spacer with different floating characteristics. The main finding from the spacer perforation is that it does not improve mass transfer for the cases simulated using conventional spacers. It was also shown that spacers with larger perforation decrease mass transfer by over 10% due to weakening of the flow velocity and suppression of vortex shedding. The simulation results also reveal that the floating ratio (R_f) is not a determining factor for permeate flux enhancement. This is because the transport mechanism is more dependent on other geometric characteristics, such as a 2- or 3-layer design. The techno-economic modelling reveals that advanced spacers are more effective than conventional spacers in improving flux in the region close to the inlet for high-permeance membranes. This is due to the fast decrease in feed flow along the channel. This thesis found that an increase in membrane permeance (up to $10 \text{ L m}^{-2} \text{ h}^{-1} \text{ bar}^{-1}$) can reduce total processing cost of SWRO and BWRO by 7.5% and 32%, respectively regardless of spacer type used. The main finding from techno-economic analysis is that improving spacer design is more crucial than increasing permeance at same recovery.

TABLE OF CONTENT

LIST OF TABLES

LIST OF FIGURES

LIST OF SYMBOLS

LISTS OF SYMBOLS

A_m	Membrane area in module (m^2)
C_c	Capital unit cost ($/m^3)
C_{dp}	Pressure drop unit cost($/m^3)
C_{op}	Operating pressure unit cost ($/m^3)
C_{pt}	Pre-treatment unit cost($/m^3)
C_{total}	Total processing unit cost ($/m^3)
c_e	Energy cost ($/kWh)
c_m	Membrane cost ($/m^2)
c_{total}	Total processing cost ($)
D	Solute diffusivity (m^2/s)
d_f	Spacer diameter (m)
d_h	Hydraulic diameter (m)
d_{per}	Perforation size (m)
F_a	Amortisation factor (yr^{-1})
f_{form}	Form friction
$f_{glob} = \dfrac{d_h}{2\rho u_{eff}^2}\dfrac{\Delta p_{ch}}{L}$	Fanning friction factor
$\overline{f}_{skin} = \dfrac{\overline{\tau}_t}{\dfrac{1}{2}\rho u_{eff}^2}$	Skin friction coefficient
h_{ch}	Channel height (m)
J	Permeate mass flux (kg m^{-2} s^{-1}, L m^{-2} h^{-1})
J_w	Transmembrane water flux (m/s)
$k_{mt} = \dfrac{D}{w_w - w_b}\left(\dfrac{\partial w}{\partial y}\right)_w$	Mass transfer coefficient (m/s)
L	Membrane channel length (m)
l_m	Mesh length (m)
L_p	Membrane permeance (L m^{-2} h^{-1} bar^{-1})
l_m	Mesh length (m)
M_{loc}	Local mixing index (s^{-2})

N	Number of envelopes
n	Distance in surface-normal direction (m)
p	Pressure (Pa)
Q	Volumetric flow rate (L/s, L/h)
ΔQ	Permeate flow rate across membrane (m^3/s)
$\Delta p_{tm,in}$	Inlet transmembrane pressure (Pa)
$Pn = SPC\dfrac{\rho^2 h^4}{\mu^3}$	Power number
$\mathrm{Re}_h = \dfrac{\rho \cdot u_{eff} \cdot d_h}{\mu}$	Hydraulic Reynolds number
R_f	Floating ratio
$R_{\mathrm{int}} = 1 - \dfrac{w_p}{w_w}$	Membrane intrinsic rejection
$R_r = \dfrac{Q_p}{Q_{in}}$	Recovery rate
$Sc = \dfrac{\mu}{\rho \cdot D}$	Schmidt number
$Sh = \dfrac{k_{mt} \cdot d_h}{D}$	Sherwood number
$SPC = \dfrac{\Delta p_{ch} \cdot u_{eff}}{L}$	Specific energy consumption (W/m^3)
t_{op}	Operation time (h/yr)
u_{avg}	Inlet velocity (m/s)
$u_{eff} = \dfrac{u_{b,in}}{\varepsilon}$	Effective velocity (m/s)
$\bar{\mathbf{v}}$	Velocity vector (m/s)
w	Solute mass fraction
x	Distance in the bulk flow direction, parallel to membrane surface (m)
y	Distance from the bottom membrane surface, in direction normal to the surface (m)
z	Distance in the direction perpendicular to both x and y (m)

LIST OF GREEK LETTERS

α	Flow attack angle (°)
Δp_{ch}	Pressure drop (Pa)
δ_{ch}	Membrane channel width (m)
ε	Porosity
$\gamma = \dfrac{w_w - w_p}{w_b - w_p}$	Concentration polarisation modulus
λ_2	Lambda-2 vortex criterion (s^{-2})
μ	Dynamic viscosity ($\text{kg m}^{-1}\,\text{s}^{-1}$)
η_{pump}	Pump efficiency
$\eta_R = \dfrac{p_0 - p_a}{(p_0 - p_a)_{ideal}}$	Retentate pressure recovery efficiency
π	Osmotic pressure (Pa)
$\pi_{in} = \varphi \cdot w_{b,in}$	Inlet osmotic pressure (Pa)
ρ	Fluid density (kg/m^3)
$\bar{\phi} = \dfrac{1}{A}\int \phi\, dA$	Area-averaged variables (e.g., k_{mt}, Sh and τ_t)
σ	Reflection coefficient
φ	Osmotic pressure coefficient (Pa)
$\bar{\tau}_t = \mu \dfrac{\partial\left[\hat{\mathbf{n}} \times (\bar{\mathbf{v}} \times \hat{\mathbf{n}})\right]}{\partial n}$	Wall shear stress (Pa)
ψ	Ratio of volumetric flux to impermeable mass transfer coefficient

LIST OF SUBSCRIPTS

b	Value for the bulk flow
BW	Value for brackish water
f	Value for the feed
in	Value at the domain inlet
$middle$	Value at the middle of membrane channel
$near\ mem$	Value near membrane surface ($0.2h_{ch}$ from membrane surface)

out	Value at the domain outlet
p	Value for the permeate
SW	Value for seawater
TA	Time-averaged value of variable
w	Value on the feed side membrane surface (wall)
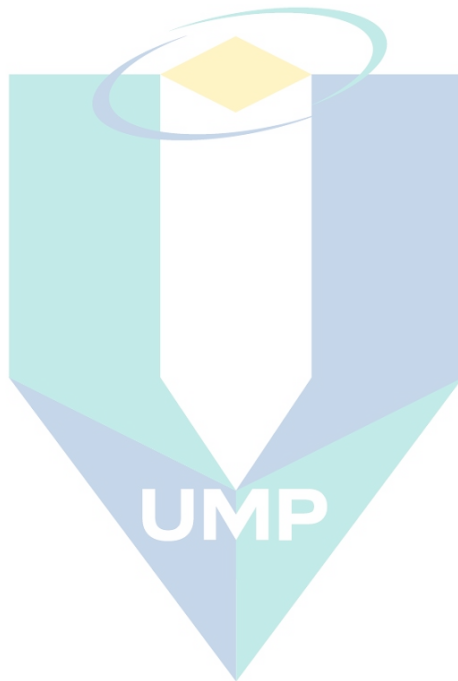
LIST OF ABBREVIATIONS

BWRO	Brackish water reverse osmosis
CAD	Computer aided design
CFD	Computational fluid dynamics
CP	Concentration polarisation
CT	Computed tomography
ERD	Energy recovery device
FO	Forward osmosis
GCI	Grid convergence indices
GO	Graphene oxide
OCT	Optical coherence tomography
PIV	Particle image velocimetry
PRO	Pressure retarded osmosis
RO	Reverse osmosis
SWM	Spiral wound membrane
SWRO	Seawater reverse osmosis
TDS	Total dissolved solid
TFC	Thin film composite
TFN	Thin film nanocomposite
TPMS	Triply periodic minimal surface
UF	Ultrafiltration

CHAPTER 1

INTRODUCTION

1.1   Research Background

Membrane-based desalination processes have gained global attention due to their simplicity and lower operating cost compared to thermal-based desalination processes (Qasim et al., 2019). For the desalination process using reverse osmosis (RO) membrane, spiral wound membrane (SWM) module is the standard configuration. For this module design two flat sheet thin film composite (TFC) RO membranes are sealed together with a permeate collection material placed between them. Feed spacers are then placed on the top selective layer of each membrane. It is followed by rolling the sandwiched sheets into a spiral format around a perforated central tube to complete the module fabrication.

SWM modules have been used for industrial applications since the 1960s for seawater RO (SWRO) (Glater, 1998) and further extended to nanofiltration (NF) in the early 1980s (Yang et al., 2019). Of the osmotic processes, RO has been the focus of much attention for six decades (Haidari et al., 2018b). RO technology is used in around 50% of desalination plants around the world (Qasim et al., 2019), with fresh water production over 90 million m^3/day (Goh et al., 2018). RO is a pressure-driven process which applies hydraulic pressure on a feed stream containing high solute concentration, forcing clean water with much lower solute concentration (in most of the cases, less than 150 ppm total dissolved solid (TDS)) to diffuse through a semi-permeable membrane. The RO process is similar to the other pressure-driven processes such as NF, with the main differences being in terms of membrane pore size and the ability to reject molecular or ionic species (Nagy, 2019). For example, RO membranes exhibit monovalent salt rejection (e.g., NaCl) above 95% while the larger pore size of NF membranes are only able to achieve between 30 and 90% of the salt rejection.

Some approaches to reduce the energy consumption and environmental impact of membrane-based desalination processes are: 1) employing high-permeance membranes to obtain larger permeate flows at the same operating pressure (Cohen-Tanugi et al., 2014;

Lim et al., 2018; Okamoto & Lienhard, 2019); 2) employing high-efficiency energy recovery devices (ERD) to recover energy from the retentate (Manth et al., 2003; Mirza, 2008; Qasim et al., 2019); 3) improving membrane module design and/or optimising operating conditions (Goh et al., 2018; Oh et al., 2009); and 4) utilizing advanced pre-treatment processes with minimum usage of chemicals for RO feed water to reduce membrane fouling in spiral wound membrane (SWM) modules (Anis et al., 2019; Lau et al., 2014; Qasim et al., 2019). Of these approaches, improving the water permeability of the membrane is given the most attention, mainly because it is the "heart" of the entire desalination process. However, at current membrane permeance levels, further improvements have shown an asymptotic curve in terms of the reduction in energy requirements due to thermodynamic and mass transfer limits. Nevertheless, further gains in terms of capital cost savings are achievable with the use of fewer pressure vessels when high-permeance membranes are employed (Cohen-Tanugi et al., 2014).

It has been shown in the literature that an understanding of hydrodynamics near the boundary layer in spacer-filled membrane channels is important for the design of spacer geometries (Fimbres Weihs & Wiley, 2010). However, the efforts to develop this understanding are hindered by the difficulties encountered to visualise the flow near the very thin boundary layer, which has a thickness of the order of 10^{-5} to 10^{-4} m. Despite recent advancements in Particle Image Velocimetry (PIV) for flow visualisation (Haidari et al., 2018a), one major issue encountered in PIV is the requirement of high resolution and expensive experimental set-up (Liu et al., 2010; Ryerson & Schwenk, 2011). Computational Fluid dynamics (CFD), on the other hand, offers flexibility in visualising flow at any points on the feed side of SWM regardless of operating conditions (Fimbres Weihs & Wiley, 2010). CFD also provides better prediction of the membrane performance for a range of membrane properties and operating conditions, and deeper understanding of the effects of flow dynamics and water transport mechanisms (Van der Bruggen, 2018).

The flow inside membrane channels can be modelled using either two-dimensional (2D) (Fimbres Weihs & Wiley, 2008; Hui et al., 2011; Y.-L. Li et al., 2012; Yazgan-Birgi et al., 2018) or three-dimensional (3D) CFD (Ali et al., 2019; Bucs et al., 2015; Fimbres Weihs & Wiley, 2007; Gu, Adjiman, et al., 2017; Haddadi et al., 2018; Kavianipour et al., 2017; F. Li et al., 2004, 2005; Saeed et al., 2012; Santos et al., 2007;

Shakaib et al., 2009). Although 2D simulations require relatively less computational load than 3D simulations, they do not fully capture the detailed flow structures present in 3D flow (Fimbres Weihs & Wiley, 2010; Haddadi et al., 2018). The main difference between 2D and 3D model is the presence of other flow structures such as lateral flow and streamwise vortices in the channels for 3D model. This raises the importance of 3D modelling for gaining insights into the local flow patterns and mass transfer that occur in the feed membrane channel.

1.2 Problem Statement

One of the major issue faced in RO membrane is concentration polarisation (CP) (Balster et al., 2006; Gu, Adjiman, et al., 2017). CP is the accumulation of rejected solute on membrane boundary surface, resulting in an increase of rejected solute concentration on membrane surface, which inhibits further mass transfer enhancement. Although spacers help to increase mass transfer by minimising the concentration polarisation (CP) effect (Kavianipour et al., 2019; F. Li et al., 2002; Sreedhar et al., 2018a), it at the same time compromises membrane performance by increasing pressure loss compared with the membrane without using spacers (Amokrane et al., 2015; Haidari et al., 2016; Kavianipour et al., 2017; Kerdi et al., 2018). A previous study reported that the pressure loss for an unobstructed channel is only one-fifth of that of the spacer-filled channel (Kavianipour et al., 2017). In addition, experimental studies performed by Haidari et al. (2016) found that spacer-filled channels show 2 to 8.5 times higher pressure loss than the empty channel owing to the porosity differences between the empty and spacer-filled channel.

One possible way to enhance membrane performance is through increasing channel porosity in spacer-filled channels by creating perforation within the spacer matrix. This is proven in study by Kerdi et al. (2018), where pressure loss can be reduced by 15% using perforated spacer filaments under typical feed velocity conditions. Although CFD simulations were conducted in that work, the authors only investigated hydrodynamic phenomena (fluid velocity and wall shear) without studying the changes in mass transfer. Thus, the distribution of local mass transfer rate for the membrane channel remains unclear.

3

It is also unclear whether perforations made at regions near to the membrane surface result in a greater disturbance to the fluid flow adjacent to the membrane surface than perforations made in the middle of the channel. Analogously, Nuntadusit et al. (2012) found that a perforation near to a surface shows superior heat transfer compared with perforation away from the surface. Liang et al. (2020) meanwhile revealed that flow mixing near the membrane wall is more important than mixing in the bulk flow. In view of this, the objective of this thesis is to compare the performance of spacers with perforation in the bulk flow with those of perforation near the membrane surface using CFD. More specifically, the effect of perforated spacers on mass transfer and pressure loss will be investigated.

The experimental study by Kerdi et al. (2018) is restricted to a single size of perforation (d_{per}/h_{ch} = 0.42). Analogously, Nanan et al. (2014) found that the heat transfer rate is lower when a larger perforation size is used. This is because for a larger perforation size, the fluid tends to flow more in the axial direction, therefore reducing the fluid-wall interaction. This clearly indicates that perforation size has significant impacts on the hydrodynamics and efficiency of membrane systems. Although Kerdi et al. (2018) found that pressure loss decreases with increasing number of perforations of a spacer, it is still unclear how the spacer perforation manipulates the local flow structure that consequently affects pressure loss. This thesis thus focuses on modifying conventional spacer geometry (i.e., dual-layer non-woven spacer) by perforating spacer filament and analyses the effect of different perforation aspects of spacers on the membrane performance via CFD.

It should be noted that pressure loss is not only the parameter to measure membrane module performance. A recent 3D CFD study showed that woven spacers outperform non-woven spacer geometries in terms of mass transfer enhancement and CP reduction (Gu, Adjiman, et al., 2017). However, that study only focused on dual-layer spacer configurations and a single Reynolds number. Given that the middle spacer in multi-layer spacer configurations exhibits "floating" characteristics (where the filaments do not make contact with the membrane) similar to those of the woven spacers, and has the ability to promote fluid flow toward the membrane surface without covering the membrane surface (Schwinge, Wiley, et al., 2004), it is possible that the combination of the features of multi-layer and woven spacer configurations may show greater potential in enhancing flow towards the boundary layer and result in greater mass transfer and

4

permeate flux performance than traditional multi-layer and woven spacers. Furthermore, it is unclear whether changes in Reynolds number (i.e. flow rate) could affect the degree of shear and mass transfer enhancement for woven spacers.

This thesis aims to investigate the effect of porosity and extent of "floating" characteristics of spacer on the mass transfer performance and friction (i.e., global friction factor and wall shear). Four different feed spacer geometries, namely 2-layer non-woven (2LNW), 2-layer woven (2LW), 3-layer non-woven (3LNW) and 3-layer woven (3LW), are considered. The mechanisms of shear and mass transfer enhancement for spacers with floating characteristics are investigated using 3D CFD simulations.

Given that a spacer with floating characteristics has less contact area with the membrane surface, this characteristic may lead to greater wall shear and potentially decrease the extent of CP and fouling propensity. However, to the best of our knowledge, no metric for the extent of "floating" for a spacer geometry has been reported in the literature. This thesis thus proposes a measure of floating characteristics, where spacers with higher floating characteristics has less contact area with the membrane surface, leading to greater wall shear and potentially decrease the extent of CP and fouling propensity.

Since the permeate flux in SWM is not only controlled by the driving force, but also by the degree of mixing or CP phenomenon caused by the advanced spacer, the extent to which an advanced spacer geometry would be more beneficial than their conventional spacer counterpart (i.e., 2-layer non-woven) for SWRO and BWRO is unclear. Although recent developments in proposed advanced/novel spacer geometries have shown significant improvement in terms of permeate flux, the tests for those new spacers have only been conducted either in small-scale CFD studies (Gu, Adjiman, et al., 2017; Han et al., 2018) or lab-scale experiments (Sreedhar et al., 2018a; Sreedhar et al., 2018b; Thomas et al., 2018, 2019). Hence, the relative benefit of advanced spacers on flux enhancement for a large-scale module in comparison with conventional spacer designs remains unclear. This thesis analyses the effect of implementing a hypothetical advanced spacer with higher mass transfer and lower pressure loss features in a full-scale membrane module, in order to compare its performance against a conventional spacer design. This study can therefore shed insights into whether future research directions should focus more on improving spacers or membrane permeance.

It is also worth noting that the performance of RO systems is sensitive to different operating and feed conditions (Oh et al., 2009). However, there is no clear understanding of the effects of operating and feed conditions on cost-effectiveness, especially for high-permeance membranes. Thus, this thesis also investigates the effects of advanced spacers as well as operating and feed conditions on permeate flux, mass transfer coefficient, CP index and on overall system performance (in terms of total water processing cost), in combination with high membrane permeance for both SWRO and BWRO.

A reliable model-based analysis is useful for designing and improving RO systems. Gastelum Reyes and Fimbres Weihs (2016) developed a multi-scale approach in which detailed results obtained for mass transfer and pressure drop from small-scale (i.e., sub-millimetre) CFD simulations are used to predict the overall performance for an actual size of SWM (i.e., a few metres in length). This mechanistic model thus captures important operating factors that interplay between the permeate flux, CP, recovery rate and pressure drop of an entire SWM module. In addition, the mass transfer coefficient alone may be insufficient to evaluate the efficiency of a spacer for RO systems.

There are several tools for evaluating membrane performance such as specific energy consumption (SEC) (Karabelas et al., 2018; Koutsou et al., 2020; Ruiz-García & Pestana, 2019), specific power consumption (SPC) (Kavianipour et al., 2017, 2019; F. Li et al., 2002; Saeed et al., 2015), spacer configuration efficacy (SCE) (Kavianipour et al., 2017, 2019; Saeed et al., 2015), spacer performance ratio (SPMP) (Kavianipour et al., 2019; Schwinge et al., 2002) and economic analysis (Im, Jeong, Jeong, & Jang, 2020). Of those, an economic analysis is a more appropriate tool because it can be used to evaluate the economic impacts of energy consumption, rather than inferring them from proxy indicators. However, an accurate economic analysis is very tedious (Al-Obaidi et al., 2019; Filippini et al., 2019). Despite this, it is possible to carry out an insightful membrane module efficiency comparison by using a simplified economic analysis that takes into account the most important relevant parameters, i.e., pre-treatment costs, operating pressure, pressure drop and capital costs. Hence, this work aims to use a simplified economic model to identify the most important factors driving the minimisation of the total water processing cost when using advanced spacers and high-permeance membranes under different operating conditions.

1.3   Objectives

The objectives of this thesis are:

i.   To analyse the effect of different perforation aspects of spacers on the membrane performance via CFD;

ii.   To investigate the mechanisms that result in shear stress and mass transfer enhancement for spacer with different degrees of "floating" characteristics;

iii. To perform techno-economic analysis that employs advanced spacer designs and high-permeance membrane for seawater RO (SWRO) and brackish water RO (BWRO).

1.4   Research Scope

The following scopes are proposed to meet the objectives in the present work.

i.   Investigation of different perforation aspects of spacers on conventional spacer (i.e., 2-layer non-woven) at the same flow attack angle (α), mesh length (l_m) and spacer diameter (d_f/h_{ch}) for the same channel height ($h_{ch} = 1$ mm), for a Reynolds number (Re_h) range of 50 – 200. The aspects investigated include location of spacer perforations, perforation sizes and number of perforations;

ii.   Study of "floating" characteristics and hydrodynamics in four spacer geometries: (a) conventional 2-layer non-woven spacer (2LNW); (b) 2-layer woven spacer (2LW); (c) 3-layer non-woven spacer (3LNW); and (d) 3-layer woven spacer (3LW) at the same flow attack angle (α), mesh length (l_m) and spacer diameter (d_f/h_{ch}) for the same channel height ($h_{ch} = 1$ mm), for a Reynolds number (Re_h) range of 50 – 200.

iii. Techno-economic study on RO process employing advanced spacer design and high-permeance membrane in large-scale model for both SWRO and BWRO under typical feed and operating conditions.

1.5   Novelty

The novelty points in this thesis includes:

i.   The extent of pressure loss reduction while maintaining mass transfer in the feed side of a membrane module is investigated by increasing channel porosity through perforating conventional spacer geometry Different aspects of perforation parameters (i.e., location of spacer perforations, perforation sizes and number of perforations) were also studied using CFD;

ii.   The degree of "floating" characteristics in spacer geometries are studied using CFD simulations to investigate the mechanisms that result in shear stress and mass transfer enhancement. The effect of porosity and extent of "floating" characteristics of spacer on the mass transfer performance and friction (i.e., global friction factor and wall shear) are also studied;

iii. A techno-economic case study for advanced spacer and high-permeance RO membrane are investigated.
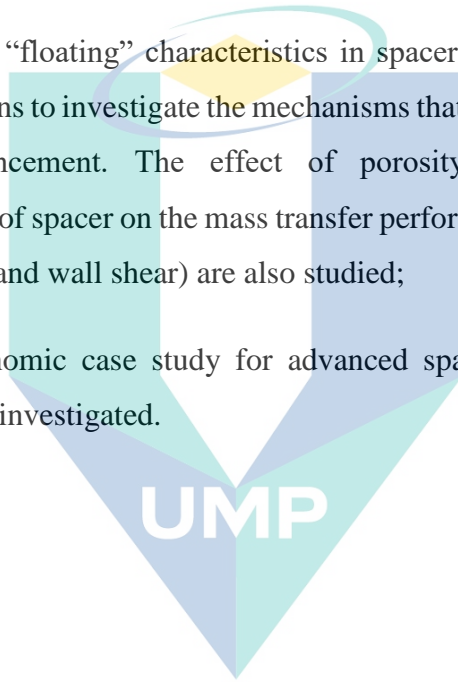
CHAPTER 2

LITERATURE REVIEW

2.1   Background of Spiral-Wound Membrane (SWM) Module

Membrane-based desalination processes have gained global attention due to their simplicity and lower operating cost compared with thermal-based desalination processes (Qasim et al., 2019). For the desalination using reverse osmosis (RO) membranes, spiral wound membrane (SWM) modules are the standard configuration. In this module design (as shown in Figure 2.1), two flat sheet thin film composite (TFC) RO membranes (labelled as "membrane leaf") are sealed together on three sides (forming a type of envelope sheet), with the membrane porous layers (a.k.a. substrate) facing each other and a permeate collection material placed between them. Feed spacers are then placed on top of the selective layer of each sheet, and this is followed by rolling the sandwiched sheets into a spiral format around a perforated central tube to complete the module fabrication.

Some of advantages in SWM module includes: 1) high-pressure durability; 2) highly compact; 3) minimum membrane contamination; and 4) minimum pressure drop in permeate channel (Ismail et al., 2019). SWM modules have been used for industrial applications of seawater RO (SWRO) since the 1960s (Glater, 1998), and their use has been further extended to nanofiltration (NF) in the early 1980s (Yang et al., 2019). For emerging osmotic membrane processes such as forward osmosis (FO) and pressure retarded osmosis (PRO), the development of SWMs is still at an early stage and is only limited to lab-scale studies (Im, Jeong, Jeong, Cho, et al., 2020; Qing et al., 2020; M. Xie et al., 2016; Xu et al., 2010). Although some researchers report that the hollow fibre membrane configuration is more suitable for FO and PRO processes due to its higher packing density, self-mechanical support properties and better flow control on both sides of the membrane (i.e., lumen and outer surface of fibre) (Cath et al., 2006; Sivertsen et al., 2013), a large number of studies published over the years have used flat sheet membranes for assessing FO and PRO processes (Achilli et al., 2009; Al-Anzi et al., 2016; D. I. Kim et al., 2015; Plata & Childress, 2019; Qing et al., 2020; Sharma et al., 2019; Suwaileh et al., 2020; Zhang et al., 2014).

Of the osmotic processes, RO has been the focus of much attention for six decades (Haidari et al., 2018b). More than 50% of the desalination plants installed in the world are based on RO technology (Goh et al., 2018; Qasim et al., 2019). RO is a pressure-driven process which applies hydraulic pressure on a feed stream containing high solute concentration, forcing clean water with much lower solute concentration (in most of the cases, less than 150 ppm total dissolved solids, TDS) to diffuse through a semi-permeable membrane. The RO process is similar to other pressure-driven processes such as NF, with the main differences being in terms of membrane pore size and the ability to reject molecular or ionic species (Nagy, 2019). For example, RO membranes exhibit monovalent salt rejection (e.g., NaCl) above 95%, while the larger pore sizes of NF membranes are only able to achieve between 30 and 90% rejection of that salt.

Nonetheless, it must be pointed out that RO is an energy-intensive process; thus, reduction in energy consumption remains one of the main research priorities to date. Numerous studies have been conducted to reduce the energy consumption of RO processes, and they can be classified into: 1) developing ultra-high permeance membrane using advanced materials, e.g., graphene oxide (GO) membranes (Hu & Mi, 2013; Mi, 2014); 2) using high efficient energy recovery devices (Alsarayreh et al., 2020); and 3) using optimisation-based control systems (Bartman et al., 2010). Despite these efforts, advances in reduction of energy consumption have almost plateaued or reached a flat curve. For example, improvements in membrane permeability have only led to an asymptotic change in flux and energy consumption due to the high concentration polarisation that occurs at higher fluxes (McGovern & Lienhard V, 2016; Shi et al., 2017).

Membrane processes have traditionally been analysed using mathematical modelling. This allows researchers to describe and analyse real membrane problems, either from first principles or black-box modelling approaches. There are several main benefits when employing a mathematical modelling approach for performance analysis of RO membranes (Van der Bruggen, 2018). These include better prediction of the membrane performance for a range of membrane properties and operating conditions, and deeper understanding of the effects of flow dynamics and water transport mechanisms. Thus, mathematical modelling is an important element which can complement experimental studies in designing optimal operating conditions or configurations.
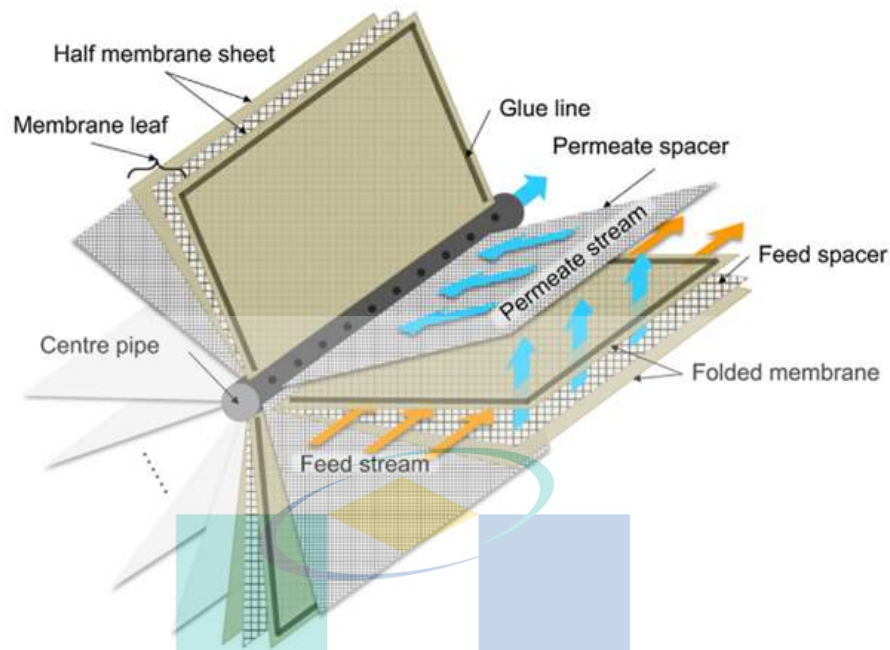
Figure 2.1   SWM module.

Source: Gu, Xu, et al. (2017)

2.2   **Development of New Spacer Designs**

SWMs consist of a sandwich of flat sheet membranes, spacer filaments and porous permeate flow material, wrapped around a central permeate collecting tube (Scott, 1995). The presence of spacers in the feed channels of the SWM helps improve permeate flux by promoting fluid mixing that enhances mass transfer and reduces concentration polarisation (Kavianipour et al., 2019; F. Li et al., 2002; Sreedhar et al., 2018a), albeit at the cost of an increased pressure loss (Amokrane et al., 2015; Haidari et al., 2016; Kavianipour et al., 2017; Kerdi et al., 2018). As spacer geometry has a large impact on the flow distribution (and hence on mass transfer), spacer modification remains an active and ongoing research field aiming to improve on three important issues: 1) flux enhancement (Gu, Adjiman, et al., 2017; Koutsou & Karabelas, 2015; Sreedhar et al., 2018a), 2) pressure loss reduction (Ali et al., 2019; Kerdi et al., 2018; Koutsou & Karabelas, 2015; Sreedhar et al., 2018a), and 3) mitigating the fouling caused by the spacer whereby some regions experience low levels of fluid mixing (Kerdi et al., 2018; Koutsou & Karabelas, 2015; Sreedhar et al., 2018a). This section reviews some of the latest proposed novel spacer designs and compares their performance for desalination.

11

The most commonly used spacer geometries in SWM modules comprise two layers of non-woven spacer filaments (Figure 2.2a) with differing cross section shapes, sizes and flow attack angles (Haidari et al., 2019; Kavianipour et al., 2019; Thomas et al., 2019). Given the current advances in CFD and 3D printing technologies, many hurdles in the design and manufacture of novel spacers with complicated configurations have been overcome. Nonetheless, 3D printing technologies of spacer are still relatively less explored by researchers, though current technologies (viz. Additive Manufacturing, AM (Lee et al., 2016) show potential in manufacturing small scale prototypes in sizes of the order of microns. There is a significant research gap to produce a more intricate spacer prototypes using 3D printing technologies. Furthermore, such intricate prototypes are generally not able to be manufactured in large scale using traditional spacer manufacturing technique. This is because 3D printing of spacer meshes requires a very high printing resolution (normally of the order of hundreds of microns) (Lee et al., 2016) and would result in high manufacturing costs for industrial applications (Balogun et al., 2019). In view of this, CFD modelling is often preferred over experimental tests for predicting the performance of novel spacer geometric designs. Hence, numerical studies of several complex spacer geometries can be found in the literature, such as the triply periodic minimal surface (TPMS) structure (Figure 2.2b) (Castillo et al., 2019; Sreedhar et al., 2018a; Sreedhar et al., 2018b; Thomas et al., 2018, 2019), perforated spacer geometries (Figure 2.2c) (Kerdi et al., 2018) and submerged spacers with column nodes (Figure 2.2d) (Ali et al., 2019; Han et al., 2018; Koutsou & Karabelas, 2015). Although a previous review (Haidari et al., 2018b) has discussed the criteria for optimising spacer design, most designs are still restricted to simple cylindrical or two-layer spacer geometries. Table 2.1 summarises some of the most important CFD and experimental works related to novel spacer development.

The TPMS spacers make use of fluid dynamics principles by interlinking the flow channels to reduce restrictions to axial feed flow (Castillo et al., 2019; Sreedhar et al., 2018a; Sreedhar et al., 2018b; Thomas et al., 2018, 2019). The lack of sharp edges in the TPMS spacer also minimises pressure drop through gradual enlargement or contraction of the flow path (Al-Shemmeri, 1988). This novel spacer design was found to outperform the permeate flux induced by commercial feed spacers in brackish water RO by 15.5% and reduce pressure drop by more than 5% (Sreedhar et al., 2018a). In addition, its

12

proponents claimed that the TPMS design is capable of reducing biofouling by at least 45%.

Another strategy to improve spacer geometry is by perforating the spacer filaments (Kerdi et al., 2018), as this has the potential to enhance permeate flux and minimise pressure drop. This strategy clearly highlights that proper modification of spacer geometry has direct effects on the hydrodynamics of the feed channel, reducing not only pressure loss but also enhancing mass transfer. In another study, Ali et al. (Ali et al., 2019) found that a submerged design with column nodes is potential to cut pressure drop to a third of that of a thicker spacer filament diameter. However, the base case selected in that study is not a typical two-layer spacer geometry. Hence, it is unclear how the proposed novel submerged geometry with column nodes performs when compared with a conventional spacer geometry.

Although several novel spacer geometries have been proposed, none of the previously mentioned studies have performed a CFD analysis of mass transfer phenomena, and only some of them included a numerical analysis of the hydrodynamics in the spacer-filled channels (Ali et al., 2019; Kerdi et al., 2018). This may be related to the high mesh refinement requirement near the surface of the intricate or sharp features of the proposed novel spacers, so as to precisely capture the hydrodynamics and mass transfer near the spacer and membrane surfaces. For example, at least 20 cells within the boundary layer in the vicinity of the spacer and membrane surfaces are required, in order to accurately resolve the wall shear and mass transfer coefficient, and to obtain grid convergence indices (GCI) of below 2.5%.
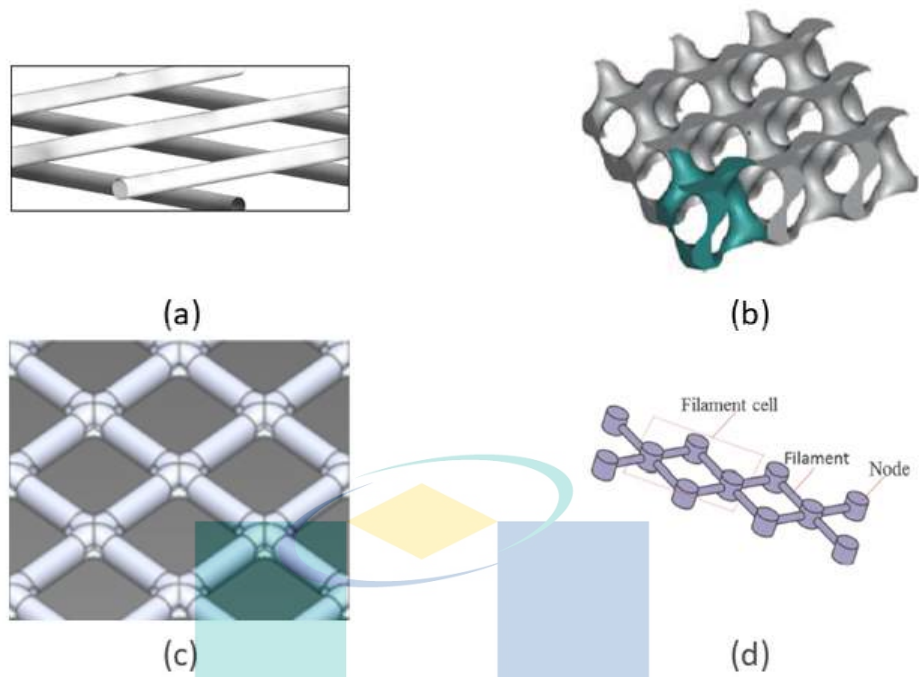
Figure 2.2 Spacer geometry configuration of (a) conventional spacer, (b) TPMS spacer (Sreedhar et al., 2018a), (c) perforated spacer (Kerdi et al., 2018) and (d) submerged spacer with nodes (Ali et al., 2019).

Source: Sreedhar et al. (2018a), Kerdi et al. (2018), Ali et al. (2019)

Table 2.1 Summary of important findings on novel spacer geometry.

Authors	Research type	Geometry analysed	Main findings	Observations
Koutsou and Karabelas (2015)	CFD and experimental	Submerged spacer with circular node with varying mesh length and attack angle.	• Novel spacers show 15% better performance in terms of SCE compared to conventional spacers. • Novel spacers show potential for lower pressure loss compared to conventional spacer under high Reynolds number ($Re_{ch} \approx 200$).	• No detail on meshing was provided.
Han et al. (2018)	CFD	Net type symmetric spacer with different diameter and pillar shape nodes.	• Higher porosity results in lower pressure drop and wall shear stress. • Proposed a modified friction factor to calculate area average shear stress.	• Mass transfer phenomena were not studied.
Kerdi et al. (2018)	CFD and experimental	Effect of spacer perforation on hydrodynamics.	• Perforations introduce jet-effect, thus eliminate recirculation zones and hamper growth of fouling. • 1-hole spacer results in greatest flux enhancement of 75% with pressure drop reduction of 15%. • OCT scans show that 1-hole spacer exhibits the lowest fouling degree. • 3-hole spacer results in the highest pressure drop reduction of 54% with 17% flux enhancement.	• The 3D unsteady CFD is only limited to hydrodynamics, mass transfer not included.
Ali et al. (2019)	CFD and experimental	Net-type symmetric spacer with small diameter ($d_f/h_{ch} = 0.42$) and column shape nodes.	• CFD simulation shows that proposed spacer reduced pressure drop by 3×. • Proposed spacer is able to reduce fouling and SEC by 79% and 50%, respectively. Besides, it improves average flux by 100%.	• The base case of comparisons is not a typical or conventional spacer geometry (i.e., dual-layer spacer geometry).

Table 2.2 Continued

Authors	Research type	Geometry analysed	Main findings	Observations
Sreedhar et al. (2018a), (2018b)	Experimental	3 TPMS-based spacers for UF and RO processes.	• All TPMS spacers improve flux (15.5%), reduce pressure drop (5-12.5%).	• No CFD modelling of mass transfer was conducted, hence no details on the local flow and mass transfer.
	Experimental	6 TPMS spacers for UF, and the effect of grading spacer voidage on one of TPMS spacers.	• All TPMS spacers show mass transfer enhancement and lower CP. • Change of TPMS spacer directionality has significant impact on system performance. • Functionally graded spacer porosity does not improve system performance. • Higher spacer voidage improves mass transfer, reduces pressure loss and manufacturing materials.	• Only applicable to lab scale and questionable implementation for large scale SWM module due to sharp edges of spacer.

2.3   Existing CFD Models and Their Challenges

Several CFD software packages are available and commonly used for CFD modelling of membrane channels in the literature, including commercial CFD suites such as ANSYS-CFX, ANSYS-FLUENT, COMSOL Multiphysics, as well as open source software such as OpenFOAM. Several exhaustive reviews focusing on CFD modelling of spacer-filled channels are documented in the literature (Fimbres Weihs & Wiley, 2010; Karabelas et al., 2015), this thesis thus discusses some of the recommendations proposed in recent years (2015 to date) and evaluates their relevance. From the previous relevant reviews, several recommendations are proposed for future work. These include: 1) coupling mass transfer with fouling models (Fimbres Weihs & Wiley, 2010), 2) validating CFD through experimental work, such as particle image velocimetry (PIV) for flow visualisation (Fimbres Weihs & Wiley, 2010), and 3) developing robust and reliable SWM module-scale models (Karabelas et al., 2015).

In CFD modelling of RO process, there are two most common boundary condition can be used, namely impermeable wall and permeable wall boundary conditions (Fimbres Weihs & Wiley, 2010). Impermeable wall (*viz.* dissolving wall) boundary conditions treat membrane wall as non-slip condition with constant solute mass fraction on membrane. On the other hand, permeable wall boundary conditions consider fluid extraction normal to membrane wall

For simplicity of computation, CFD modelling of RO processes usually focuses on fluid flow modelling on the feed side without taking into consideration the permeate channel. This is because there is a very small pressure drop on the permeate channel and concentration polarisation (CP) on the permeate side is negligible. The permeate pressure at any point within the SWM module can be assumed at about 1 bar. For these reasons, only the water flux and solute rejection that take place on the feed side of the membrane are investigated in CFD modelling of RO.

The reliability and applicability of CFD as a prediction tool in terms of feed conditions (e.g., seawater salinity and feed flow rate) have been well discussed and validated in the literature (Gill et al., 1988; Wiley & Fletcher, 2002). For example, the reliability of CFD simulations is not greatly affected by the inclusion of density variations, as buoyancy effects do not dominate (Fletcher & Wiley, 2004). Similarly,

viscosity does not play a big role in the main mass transfer mechanisms that drive concentration polarisation and performance decrease due to that phenomenon (Gill et al., 1988). Nonetheless, care must be taken when modelling high salinity conditions, as the membrane surface concentration may increase above the saturation limit for salt precipitation, in which case scaling modelling should be included.

At the time of writing, CFD studies of RO processes have mainly focused on either 2D unsteady state (Foo et al., 2020; Liang et al., 2018; Liang, Fimbres Weihs, Setiawan, et al., 2016; Liang, Fimbres Weihs, & Wiley, 2016; Su et al., 2018, 2019) or 3D steady state (Gu, Adjiman, et al., 2017; Haddadi et al., 2018; Han et al., 2018; Kavianipour et al., 2017, 2019; Mansouri et al., 2019; Usta et al., 2017). It is worth noting that the ability of 2D and 3D CFD modelling for predicting mass transport and concentration polarisation has been well established in the literature (Foo et al., 2020). While 3D unsteady models would provide more insights than 2D unsteady or 3D steady studies, they require very significant computational power and time to converge. To the best of our knowledge, the works conducted by Kerdi et al. (2018) and Koutsou et al. (2007) are the only studies that simulated 3D unsteady flow in spacer-filled channels. However, these works are limited to analysing hydrodynamics, without including mass transfer. This is because mass transfer would require computational resources several times larger than hydrodynamic-only studies.

Another important growing trend in modelling RO membrane channels is the emergence of different types of fouling models (Bucs et al., 2018; Jeong et al., 2020; Radu et al., 2014; Su et al., 2019; Uppu et al., 2019). Of the different types of fouling, biofouling modelling perhaps is gaining the most attention (Bucs et al., 2018; Choi et al., 2020; Jeong et al., 2020) as it is the type of fouling that has the largest effect on RO membrane performance due to excessive accumulation of biomass on the membrane surface. Nevertheless, developing a good biofouling model requires information of biofilm properties, which can only be obtained through experimental studies (Bucs et al., 2018). Biofilm mechanical properties, for instance, can be obtained from a combination of numerical modelling and data obtained from optical coherence tomography (OCT) scans (Picioreanu et al., 2018). Most 2D and 3D CFD studies of biofouling have been validated experimentally (Radu et al., 2010, 2012; Vrouwenvelder et al., 2010), and this gives confidence in the prediction of biofouling on the membrane surface. However, one

of the main issues associated with this kind of modelling is that it requires a significant amount of computational resources, and often necessitates the integration of a collection of software packages due to the very different length scales involved: unsteady hydrodynamics requires time steps of the order of microseconds, whereas fouling in the feed channel occurs over long time scales of the order of days or weeks.

Besides biofouling in actual RO practice, other types of fouling such as scaling, particulate and organic fouling can occur simultaneously and interact with each other (Tang et al., 2011). To our best knowledge, currently only one work conducted by Radu et al. (2015) has numerically modelled the interaction between scaling and biofouling. It must be emphasised that modelling the interaction between different types of fouling, and the effects of the interaction between hydrodynamics and mass transfer on fouling is very challenging, mainly due to the lack of understanding and knowledge of the first principles associated with those interactions. More efforts towards these research directions are therefore required.

A recent review by Bucs et al. (2018) highlighted that a complete computational technique should take into account not only unsteady flow, but also the fluid-biofilm interaction, in order to investigate both permeation and biofilm removal. In addition, the authors proposed a possible optimisation loop which used X-ray computed tomography (CT scanning step) to obtain a more accurate spacer geometry measurement for computer aided design (CAD) and CFD simulation analysis. They claimed that X-ray computed tomography is useful in resolving the over-simplified spacer geometry in CFD simulations (Haaksman et al., 2017; Horstmeyer et al., 2018). This is because real spacer meshes have some deformed features due to the polymer extrusion fabrication technique (Haaksman et al., 2017). On the other hand, Horstmeyer et al. (2018) found that a cylindrical spacer structure overestimates CP when compared to the geometries measured by CT scans. This is because the flow distribution and shear stress are incorrectly predicted when the narrow flow sections formed between spacer filaments and membrane are not taken into consideration.

Although the most common water sources considered as feed for RO systems (such as seawater and brackish water) contain multiple ionic solutes, previous modelling studies have assumed a single type of solute in the system. To the best of our knowledge, no study has been carried out so far to evaluate the effects of interactions between

19

different solutes on the membrane performance. This can be due to the lack of numerical tools for implementing them in CFD, because the mass transport equations become extremely stiff when including the electric field effects related to the solute charges. The modelling of multiple ionic solvents has only been performed for electrodialysis studies, and it has been limited to 1D studies (Guo et al., 2019). Modelling in 2D or 3D results in a high degree of stiffness in the mass transport equations, making the diffusion term non-homogenous if simple CFD techniques are used. Therefore, there are opportunities for future CFD work which can take into account multiple solute interactions in RO systems.

A commonly raised issue regarding CFD studies is the lack of or difficulty associated with obtaining data suitable for validation. In order to verify and validate CFD results, PIV provides a direct and high resolution technique to visualise flow (Haidari et al., 2019; Haidari et al., 2016, 2018a). However, it is important to note that the density of particles that are tracked with the laser needs to approximate that in the fluid in order to accurately predict the flow behaviour. This is because the particle movement will be affected by buoyant forces if their density is not equal to that of the fluid. In addition, flow field measurements can also be affected if there is a significant change in density due to sharp changes in concentration, or by shear forces such as shear-induced diffusion. Another major limitation of this technique is the requirement of a very high resolution camera in order to capture time- and spatially-varying flow velocity (Liu et al., 2010). Although some progress has been made in using PIV for studying membrane channels, only a handful of studies are available in the literature (Bucs et al., 2015; Haidari et al., 2019; Haidari et al., 2016, 2018a; Liu et al., 2010). Figure 2.3 shows the PIV experimental setup reported in the work of Haidari et al. (2019). That setup was developed to measure pressure loss and visualise the temporal and spatial velocity variations inside a spacer-filled channel. Examples of velocity vector fields at the centre of membrane channel for different orientations are shown in Figure 2.4. However, the authors of that work (Haidari et al., 2019) acknowledge that further study is required to evaluate the effect of z-velocity on the u- and v-velocities.
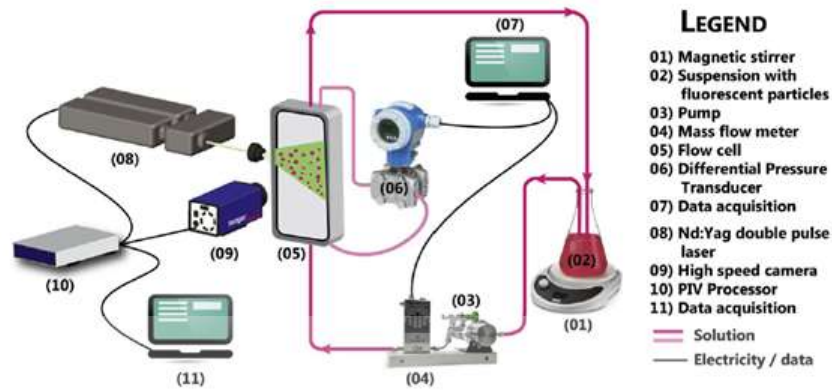
Figure 2.3   Experimental setup for flow visualization of PIV.

Source: Haidari et al. (2019)

Figure 2.4   Velocity vector obtained from PIV imaging at center of membrane channel for (a) ladder orientation and (b) normal orientation.

Source: Haidari et al. (2019)

Although several novel spacers have been proposed in the literature (Gu, Adjiman, et al., 2017; Kerdi et al., 2018; Koutsou & Karabelas, 2015; Sreedhar et al., 2018a; Sreedhar et al., 2018b), those studies have been limited to either lab scale experiment (i.e., test section of order of centimetre) or small scale simulation (i.e., a few unit cells in millimetre-scale). Real RO membrane desalination systems are in fact in several meters in length (Karabelas et al., 2018; Ruiz-García & Pestana, 2019). Thus, multi-scale models are required to predict the effectiveness of a novel spacer in full-length SWM desalination systems (Cohen-Tanugi et al., 2014; Guillen & Hoek, 2009; Karabelas et al., 2018). These models refer to the combination of the small-scale details of the spacer geometry with the large-scale RO module. More specifically, small-scale CFD simulations can be used to generate correlations for predicting the Sherwood number and friction factor dependence

on Reynolds number. These predictions can be subsequently used to determine the mass transfer coefficient and pressure drop, which are then used as inputs to solve ordinary differential equations (ODEs) for flux, salt and pressure drop along the membrane module in a large-scale module. Several small-scale CFD studies have included fouling effects during analysis (Koutsou et al., 2018; Su et al., 2019; Uppu et al., 2019), but until now robust multi-scale models incorporating fouling phenomena are yet to be developed. Future work on this is thus highly recommended for accurate prediction of long run membrane system performance.

2.4   Module Performance Metrics

An ideal SWM desalination system is the one which shows superior permeation flux, low propensity to fouling and low energy consumption. This highlights the need for critical criteria to assess the efficiency of a SWM desalination system from a selection of best spacer geometries, operating conditions and module configurations. It is worth noting that a number of module performance metrics are commonly used in the literature and, thus, this section of the review discusses their relevance in the context of membrane-based desalination.

High energy consumption remains an important issue that needs to be overcome for membrane-based desalination applications. Energy loss across the membrane is inevitable, and this represents the largest portion of energy losses in the membrane separation process. Karabelas et al. (2018) suggested that energy consumption across the membrane (i.e., energy consumption to overcome osmotic pressure and membrane resistance) accounts for 77% and 72% of energy losses for seawater RO and brackish water RO, respectively. This suggests that most of the energy consumption mentioned earlier, of the order of 2.2 kWh/m^3, is due to the pressure loss across the membrane, not along the channel. Furthermore, at a higher rate of recovery (that is higher flux), less energy can be recovered because the flow of retentate decreases.

Given that energy consumption remains an important issue for RO, many energy performance metrics have been proposed. These include 1) specific power consumption ($SPC = \dfrac{\Delta P \cdot u_{eff}}{l}$) (Kavianipour et al., 2017, 2019; F. Li et al., 2002; Saeed et al., 2015), 2) spacer configuration efficacy ($SCE = \dfrac{Sh}{Pn}$) (Kavianipour et al., 2017, 2019; Saeed et

22

al., 2015), 3) spacer performance ratio ($SPMP = \dfrac{\Delta w_{spacer}/\Delta w_{slit}}{\Delta p_{spacer}/\Delta p_{slit}}$) (Kavianipour et al.,

2019; Schwinge et al., 2002) and 4) specific energy consumption ($SEC = \dfrac{W_{TOTAL}}{Q_p}$)

(Karabelas et al., 2018; Koutsou et al., 2020; Ruiz-García & Pestana, 2019). Of these, SEC is the most commonly cited indicator for measuring SWM performance. The main advantage of SEC is that it considers all the energy consumption contributions in the membrane unit (e.g. permeance) as well as the energy recovered through energy recovery devices (ERD), whereas other performance metrics such as SPC, SCE and SPMP only consider pressure loss along the membrane channel.

While the above-mentioned parameters are useful to describe module performance, they do not explicitly address the economic impacts of energy consumption, especially for a large-scale system. Despite previous studies having evaluated the economic impacts (J. E. Kim et al., 2018; Kook et al., 2018; Sarai Atab et al., 2016) or total cost (Im, Jeong, Jeong, & Jang, 2020) of large-scale desalination systems, only a handful of studies have evaluated the impact of spacer design on total cost (Schwinge, Wiley, et al., 2004).

It should be noted that economic analysis requires not only the operating conditions but also other information such as costs of electricity, equipment, labour and land. Gastelum Reyes and Fimbres Weihs (2016) recently described a simplified economic model to evaluate a RO process with respect to the cost per unit volume of water treated. The main parameters involved in that analysis are the cost of pre-treatment, the operating pressure, the pressure drop along the membrane channel and the membrane unit capital cost. The simplified economic assessment eliminates many complexities for the sake of facilitating the comparison of the effect of spacer design on the cost of desalination. In that sense, it does not evaluate the whole RO process, but only the aspects affected by the spacer configuration.

The modelling of membrane processes can involve different ranges for both the spatial (length) and temporal scales of interest. In terms of length scales, membrane models can be categorised into "unit cell" (of the order of several millimetres) or module-scale (of the order of several meters). It is notable that attempting to resolve both the small and large spatial scales of a RO process simultaneously is nearly impossible, because it

23

would require very large computational loads, making the model intractable, or significant simplifications that would trivialise the inclusion of the small-scale model. A 3D CFD model consisting of several unit cells or several millimetres in length, for instance, would require several tens of millions of discretised elements to resolve the local flow and mass transfer precisely; hence, the detailed modelling of a full-scale module would be thousands of times that size. To overcome this challenge, the performance of module-scale RO can be evaluated using a multi-scale approach in which correlations for mass transfer and pressure drop obtained by data fitting the results of small-scale models are used (Okamoto & Lienhard, 2019). In terms of temporal scales, models can be categorised into either steady (aiming to selecting best module design) or transient flow simulation (aimed at understanding how the solutes or fouling components interact with the membrane surface). For transient simulation, the time scale can be categorised into short and long time scales, where the short scale refers to the transient simulations that resolve individual vortices as they travel through the membrane channel and affect mass transfer. On the other hand, the long scale simulations aim at resolving the evolution of fouling, for example biofouling, which evolve at much longer time scales.

Nevertheless, the understanding of the interactions between the local spatial and temporal variations in flow and mass transfer fields is crucial in order to design a better SWM geometry. For these reasons, this section first discusses the metrics that can be obtained from CFD simulation to measure the local performance at the unit cell scale. Generally, CFD simulations can provide data such as the local flow velocity, mass transfer coefficient (k_{mt}), water flux (J_w), solute concentration distribution (e.g. CP modulus) as well as the pressure drop (or Fanning friction factor, f_{glob}). These parameters are useful in visualising the local hydrodynamics and mass transfer performance. By analysing flow velocity and solute profiles in 2D unsteady CFD simulations, Fimbres Weihs et al. (2006) found that there are two main mechanisms responsible for mass transfer enhancement, namely increased wall shear and flow of lower concentration fluid into the concentration boundary layer. In terms of measuring vortex strength, the lambda-2 (λ_2) criterion from CFD can be used to identify vortices that are responsible for pressure loss and fluid mixing (Foo et al., 2020).

Despite the availability of performance metrics for RO, most of these are only applicable for steady state operating conditions, without taking into consideration the effects of membrane fouling. It must be emphasised that membrane fouling tends to have a significant impact on the SEC and total processing cost over long periods of operation, and future work on the analysis of this issue are therefore highly recommended.

Table 2.3 summarizes the performance metrics for small- and large-scale typically used for osmotic membrane processes. Of these indicators, SEC is perhaps the most commonly cited indicator that can be used to compare different osmotic membrane processes. However, care should be given when using this metric, because the resulting SEC can vary depending on inlet concentration, recovery, pump efficiency and model equations employed (Okamoto & Lienhard, 2019). It is very likely that no performance metric can be considered universal for comparing all osmotic membrane processes. Nevertheless, the performance metrics used for evaluating membrane processes at the small-scale can be used to understand the flow field, which is important for determining the best condition or configuration and optimising large-scale osmotic membrane processes.

Table 2.3 List of metric indicators used for membrane processes

Indicator metric	Mathematical description	Unit	Description	Observation
Concentration polarisation (Matthiasson & Sivik, 1980)	$\gamma = \dfrac{w_w}{w_{b,in}}$	-	Ratio of solute concentration at the membrane wall to the concentration at the inlet bulk.	The formulation of CP index varies depending on the choice of membrane processes used (viz. RO vs FO).
Ideal energy efficiency of desalination (Fane, 2018)	$\eta_{id} = \dfrac{\Delta G_{mix}}{SEC}$	-	Ratio of Gibbs free energy of mixing of salt/water mixture versus specific energy consumption for desalination.	Current technologies have efficiencies just below 50% of the ideal thermodynamic limit.
Fanning friction factor (Holland & Bragg, 1995)	$f_{glob} = \dfrac{d_h}{2\rho u_{eff}^2}\dfrac{\Delta p_{ch}}{L}$	-	Dimensionless measurement of pressure loss across the membrane channel.	Only related to hydrodynamics, not mass transfer.
Local mixing index (Ouyang et al., 2013)	$M_{loc} = \left(\dfrac{\partial u_p}{\partial x}\right)^2 + \left(\dfrac{\partial u_p}{\partial y}\right)^2 + \left(\dfrac{\partial v_p}{\partial x}\right)^2 + \left(\dfrac{\partial v_p}{\partial y}\right)^2$	s^{-2}	Mixing dependence on fluid stretching and folding.	The relationship between the degree of stretching and folding measured, and mass transfer enhancement is unclear.
Mass transfer coefficient (Seader & Henley, 1998)	$k_{mt} = \dfrac{D}{w_w - w_b}\left(\dfrac{\partial w}{\partial y}\right)_w$	m/s	Diffusion rate constant of water through membrane wall.	Give quick prediction of the degree of mass transfer enhancement. Typically the values are of the order of 10^{-5} m/s.
Mass transfer enhancement factor (Liang et al., 2014)	$\Phi = 1 - \dfrac{\gamma_E}{\gamma_{NE}}$	-	Relative change in concentration polarisation due to enhancement techniques.	Positive values indicate increased mass transfer, whereas negative values indicate a decrease in mass transfer and flux.
Recovery rate (Lim et al., 2018)	$R_r = \dfrac{Q_p}{Q_{in}}$	-	Ratio of volumetric permeate to feed flow rate.	Provides quick prediction of total water produced depending on types of feed water used (viz. brackish vs seawater).
Sherwood number (Sherwood et al., 1975)	$Sh = \dfrac{k_{mt} d_h}{D}$	-	Ratio of mass transfer by convection to mass transfer by diffusion.	Only diffusivity term that reflects the solute characteristics and does not take into consideration other membrane properties parameters (e.g., surface charge).

Table 2.4 Continued

Indicator metric	Mathematical description	Unit	Description	Observation
Spacer configuration efficacy (Saeed et al., 2015)	$SCE = \dfrac{Sh}{Pn}$	-	Ratio of mass transfer increment by spacer filaments to power consumption.	The limitation of this concept is that it does not show much dependence on Reynolds number.
Specific energy consumption (Bartman et al., 2010)	$SEC = \dfrac{W_{TOTAL}}{Q_p}$	kWh/m^3	Ratio of energy consumption to volumetric permeate flow rate.	Most commonly used for predicting energy usage but does not reflect the actual processing cost.
Wall shear stress (Day, 1990)	$\tau_t = \sqrt{\tau_x^2 + \tau_y^2 + \tau_z^2 - \left(\mu \dfrac{\partial \vec{v}}{\partial n} \cdot n \right)^2}$	Pa	Rate of change of velocity near the membrane surface.	Proxy indicator for anti-fouling tendencies.

27

2.5   Gap analysis

One way to increase channel porosity in spacer-filled channels is to create perforation within the spacer matrix. As mentioned in Section 1.2, Kerdi et al. (2018) reported the advantages using perforated spacer filaments, but the study did not compare the effect with conventional spacer (i.e., 2-layer non-woven spacer). This thesis thus employed CFD simulations to study different aspects of spacer perforation (i.e., location, diameter and number of perforation) for a conventional spacer geometry (i.e., dual-layer non-woven spacer) and their effects on the hydrodynamics and mass transfer under both steady and unsteady flow conditions.

A recent 3D CFD study showed that woven spacers outperform non-woven spacer geometries in terms of mass transfer enhancement and CP reduction (Gu, Adjiman, et al., 2017).In addition, Schwinge et al. (2004) have also shown that multi-layer spacer configurations show a promising economic advantage when compared with conventional dual-layer spacers. It is possible that the combination of the features of multi-layer and woven spacer configurations may show greater potential in enhancing flow towards the boundary layer and result in greater mass transfer and permeate flux performance than traditional multi-layer and woven spacers. This thesis thus investigates the effect of porosity and extent of "floating" characteristics of spacer on the mass transfer performance and friction (i.e., global friction factor and wall shear). The mechanisms of shear and mass transfer enhancement for spacers with floating characteristics are investigated using 3D CFD simulations.

It shall be noted that the relative benefit of advanced spacers on flux enhancement for a large-scale module in comparison with conventional spacer designs remains unclear. Thus, this thesis uses a simplified economic analysis to investigate the effect of implementing a hypothetical advanced spacer with higher mass transfer and lower pressure loss features in a full-scale membrane module, in order to compare its performance against a conventional spacer design. The simplified economic analysis is also used to investigate the effects of advanced spacers as well as operating and feed conditions on permeate flux, mass transfer coefficient, CP index and on overall system performance (in terms of total water processing cost), in combination with high membrane permeance for both SWRO and BWRO.

CHAPTER 3

METHODOLOGY

3.1   Basic Principles of CFD Study

The numerical solution of the governing equations of continuity, momentum and mass transfer (Equations 3.1 to 3.3) are solved using ANSYS CFX 18.2 software package.

$$\nabla \cdot \vec{\mathbf{v}} = 0 \qquad\qquad 3.1$$

$$\rho \frac{\partial \vec{\mathbf{v}}}{\partial t} + \rho \left(\vec{\mathbf{v}} \cdot \nabla \right) \vec{\mathbf{v}} = \mu \nabla^2 \vec{\mathbf{v}} - \nabla p \qquad\qquad 3.2$$

$$\frac{\partial w}{\partial t} + \nabla \cdot \left(w\vec{\mathbf{v}} \right) = D\nabla^2 w \qquad\qquad 3.3$$

where $\vec{\mathbf{v}}$ represents the velocity vector, p the pressure, ρ and μ refer to the fluid density and dynamic viscosity, respectively, D denotes the solute diffusivity, and w refers to the solute mass fraction. It should be noted that for 3D steady simulations, the first term (temporal dependent variable) in Equations (2) and (3) is not present.

The effect of buoyancy is considered to be negligible when the flow direction is perpendicular to gravity (Fletcher & Wiley, 2004). Constant fluid properties (i.e., dynamic viscosity, $\mu = 0.001$ kg/m.s and diffusivity, $D = 1.67 \times 10^{-9}$ m^2/s (Liang, Fimbres Weihs, & Wiley, 2016)) assumption can be made because the CP occurring in the RO process is much lower than those of high-flux microporous membrane process (Gill et al., 1988). A Schmidt number (Sc) of 600 is also considered as this corresponds to that for a typical NaCl concentration encountered in the RO process (Liang, Fimbres Weihs, Setiawan, et al., 2016). As RO membrane is typically characterised by dense membrane, the mass transport phenomena can thus be modelled by solution-diffusion mechanism (Baker, 2004).

29

3.1.1   Steady-state Flow

For steady-state flow simulation, three repeating unit cells are modelled in the simulations. As the inlet and outlet boundary conditions tend to create some effects on the hydrodynamics and mass transfer, the middle unit cell is selected for measuring performance metrics (e.g., Sherwood number, Fanning friction coefficient and skin friction coefficient) (Fimbres Weihs & Wiley, 2007). The spacers are treated as no-slip walls, whereas the membrane surfaces (top and bottom surface) are treated as impermeable dissolving wall. For impermeable dissolving wall, the solute concentration is fixed at a constant value ($w = w_w$). However, it is unclear whether the choice of w_w has significant impacts on mass transfer coefficient $\left(k_{mt} = \dfrac{D}{w_w - w_b} \left(\dfrac{\partial w}{\partial y} \right)_w \right)$ or dimensionless mass transfer $\left(Sh = \dfrac{k_{mt} d_h}{D} \right)$. For simplicity of investigation, a 2D empty channel (without spacer) using the boundary condition described in the literature (Fimbres Weihs et al., 2006) at Re_h of 200 is used to investigate whether different value of w_w has an impact on Sh. These findings are discussed in section 4.3.

The main benefits of using an impermeable dissolving wall is that it uses less computational load compared with the cases with permeation due to the interaction between CP and permeate flux. In addition, it was previously reported that the k_{mt} from impermeable-dissolving wall can be used to estimate the mass transfer when permeation is present (Geraldes & Afonso, 2006). As impermeable wall does not consider coupling between concentration and velocity profile in feed channel, the velocity profile in the membrane boundary layer is thus not affected by mass transfer (Liang, Fimbres Weihs, & Wiley, 2016). Due to this, impermeable-dissolving wall can be used for predicting flux. The inlet, outlet and side boundaries are treated as being translationally periodic.

The flow in all spacer geometries under consideration is studied across a range of hydraulic Reynolds number (Re_h) between 50 and 200. At these Re_h, the flow can be assumed to be laminar, as Bucs et al. (Bucs et al., 2015) found that the flow condition change from laminar to transitional flow occurs only for $Re_h > 300$ and the geometry parameter used in this study (d_f/h_{ch}) is close to those in their study (i.e., $d_f/h_{ch} = 0.6$ vs 0.57).

It must be noted that ANSYS-CFX 18.2 is not capable of solving fully-developed mass transfer boundary conditions, thus a two-step approach proposed by Fimbres-Weihs and Wiley (2007) is used to provide the mass transfer solutions in this study for 3D CFD simulation. The periodic boundary condition for mass transfer wraps the scaled mass fraction from the outlet to the inlet of the flow domain, as described in Equation 3.4:

$$\left(\frac{w_w - w}{w_w - w_b}\right)_{in} = \left(\frac{w_w - w}{w_w - w_b}\right)_{out} \qquad 3.4$$

where w_w and w_b denotes the mass fraction at the membrane surface and in the bulk flow, respectively.

3.1.2 Unsteady Flow

A 2D unsteady flow simulation is conducted to study the effect of perforated spacer under unsteady state. This is because 3D unsteady flow simulations require significantly larger computational resources than steady-state flow (Fimbres Weihs & Wiley, 2007),. However, it must be pointed out that 2D and 3D results cannot be quantitatively compared. Thus, the main point of 2D unsteady simulations is to investigate whether perforation can significantly enhance flow mixing.

Similar to the approach proposed in the literature (Fimbres Weihs et al., 2006), a total of 6 unit cells with dissolving-wall ($w = w_w$) are implemented. For details on the other boundary conditions (i.e. inlet, outlet and wall), the readers can refer to related literature (Fimbres Weihs et al., 2006). It is worth noting that the flow becomes fully-developed after about 5 or 6 spacers (Foo et al., 2020). Therefore, all the analysis of flow and mass transfer are reported based on the 9th and 10th spacer unit cell. It was found in the literature that the flow becomes unsteady after $Re_h > 500$ (Liang, Fimbres Weihs, & Wiley, 2016) under the same spacer diameter ($d_f/h_{ch} = 0.6$) considered in this work. For this reason, Re_h of 600 is considered for investigating the impact of spacer perforation on the fluid and mass transfer profile under unsteady flow conditions.

3.2 Feed Spacer Geometries

3.2.1 Perforated Spacer

Figure 3.1 shows a schematic representation of the feed spacer under consideration for first part of thesis, where there is a small degree of inter-penetration between spacer filaments to fit all spacer filaments in the membrane channel (See Figure 3.1b).
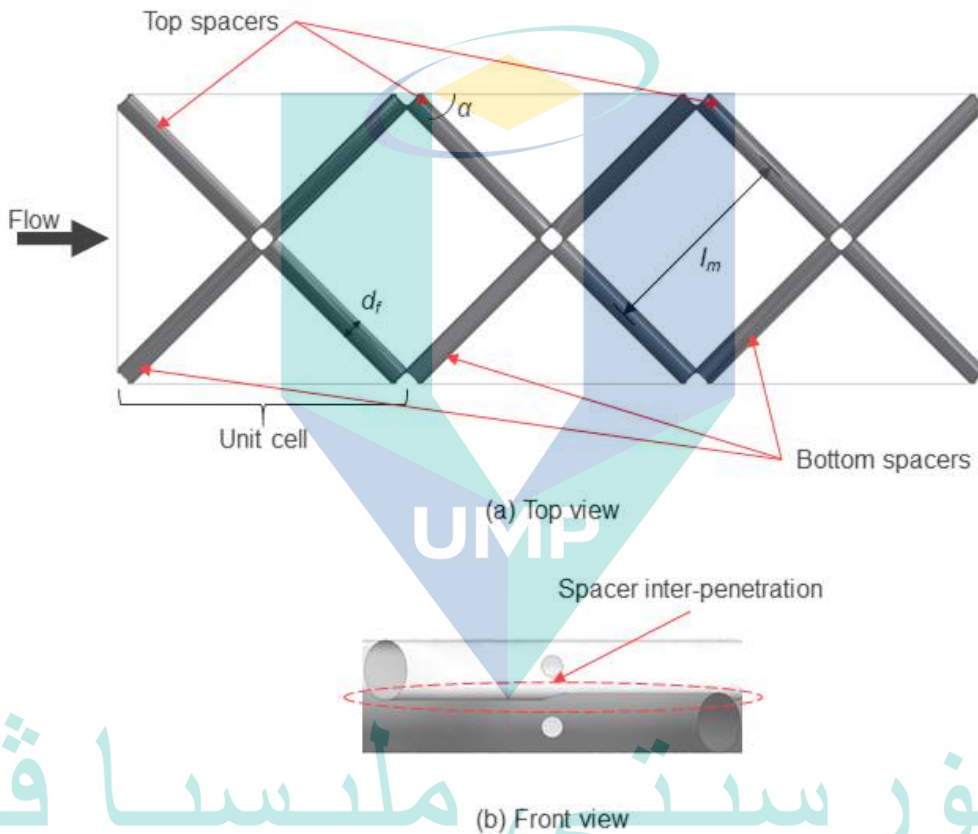
Figure 3.1 Schematic representation of the feed spacers: (a) Top view and (b) Front view.

The dimensionless parameters of the spacer geometry and perforation are shown in Table 3.1. The performance of all the spacer geometries are compared at the same flow attack angle (α), mesh length (l_m) and spacer diameter (d_f/h_{ch}) for the same channel height ($h_{ch} = 1$ mm). In order to compare the membrane performance between perforation of the spacer near the membrane with those in the middle channel (e.g., bulk flow), the total perforation area in both spacer configuration are kept the same by adjusting the perforation size ($d_{per,middle} = \sqrt{2}\, d_{per,near\ mem}$) (Figure 3.2). Since the size and number of perforations could play significant roles in affecting flow intensity (Kerdi et al., 2018;

32

Nanan et al., 2014), these factors are also taken into consideration in this study. Figure 3.3 and Figure 3.4 show the geometries of spacers with different size and number of perforations, respectively. A typical 2D unit cell geometry for perforated spacers used for study of unsteady flow is shown in Figure 3.5.
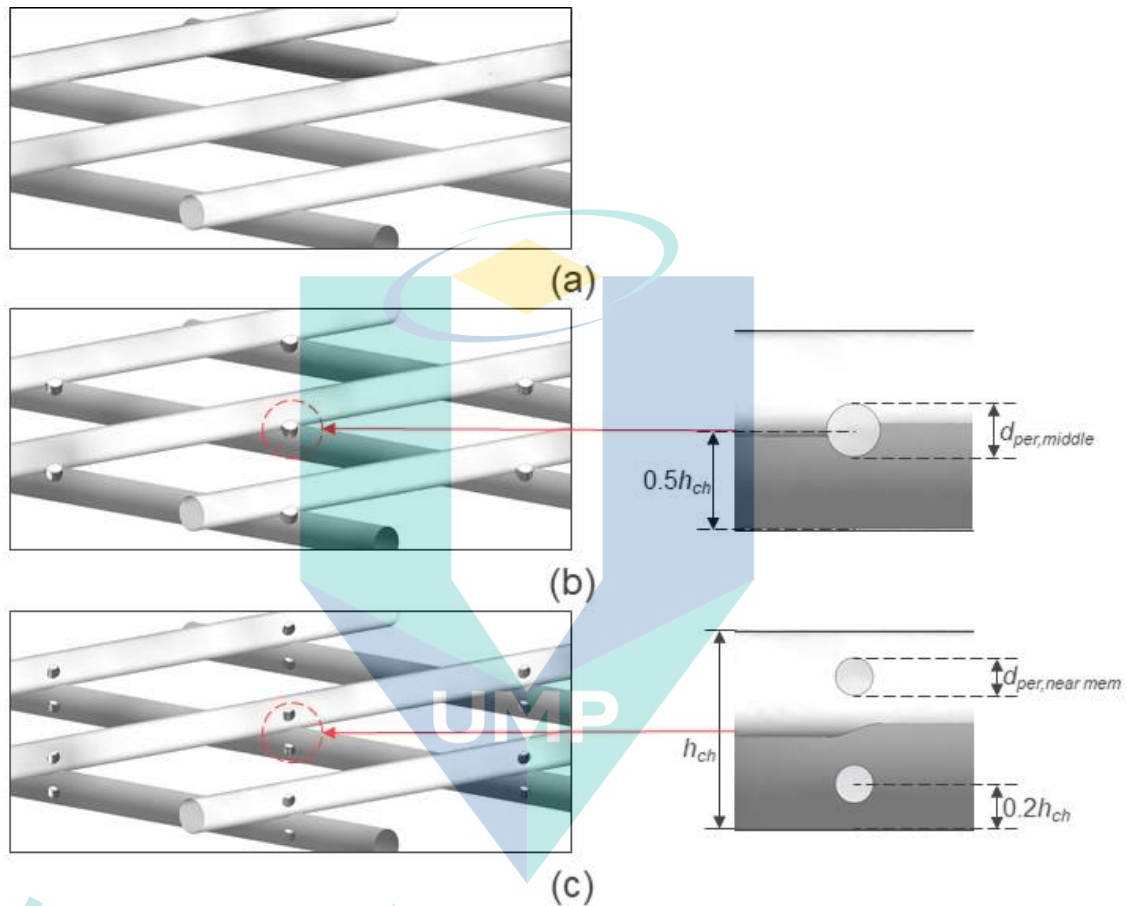
Figure 3.2 Geometries of a) non-perforated spacer, (b) spacer with perforations in the middle of the channel (i.e., bulk flow) and (c) spacer with perforations near the membrane wall. The spacer with perforation in the bulk flow is compared with those near the membrane wall at the same surface area of spacer perforation.

Table 3.1 Parameters for the perforated feed spacers considered.

Parameter	Value
Spacer diameter (d_f/h_{ch})	0.6
Mesh length (l_m/h_{ch})	5.66
Flow attack angle (α)	45°
Number of perforations	2, 4 or 6
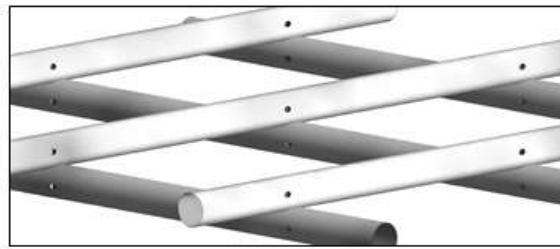
(a) Spacer with $d_{per}/h_{ch} = 0.1$
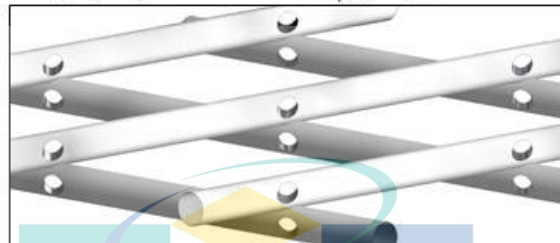
(b) Spacer with $d_{per}/h_{ch} = 0.35$

Figure 3.3 Geometries of spacer with perforation size of a) dper/hch = 0.1 and (b) dper/hch = 0.35
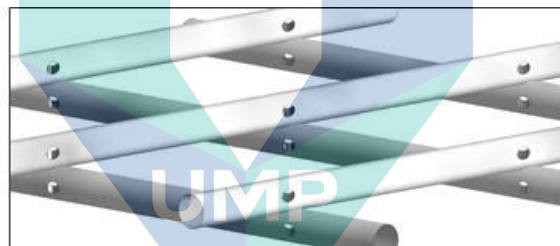
(a) 2-hole spacer
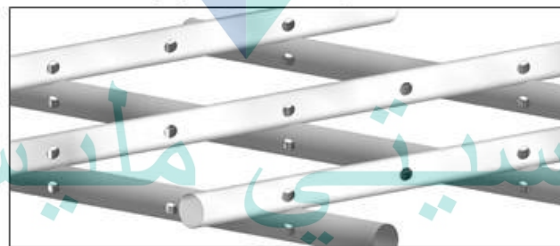
(b) 4-hole spacer
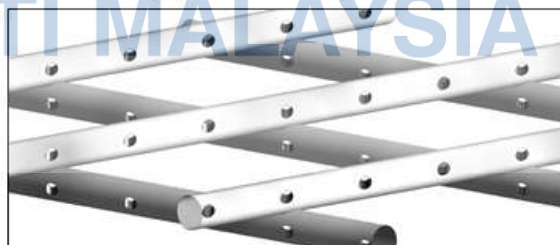
(c) 6-hole spacer

Figure 3.4 Geometries of spacer with a different number of perforations, (a) 2-hole spacer, (b) 4-hole spacer and (c) 6-hole spacer
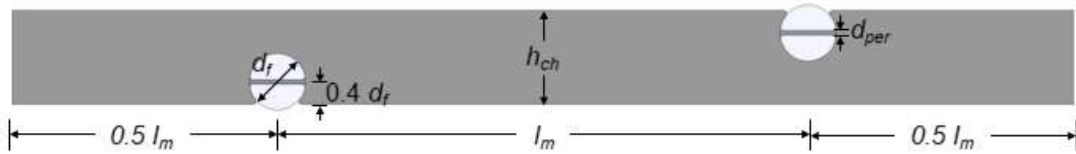
Figure 3.5 Geometry of the zig-zag spacer unit cell with spacer perforations for 2D unsteady simulation.

3.2.2 Spacer with Different Floating Characteristics
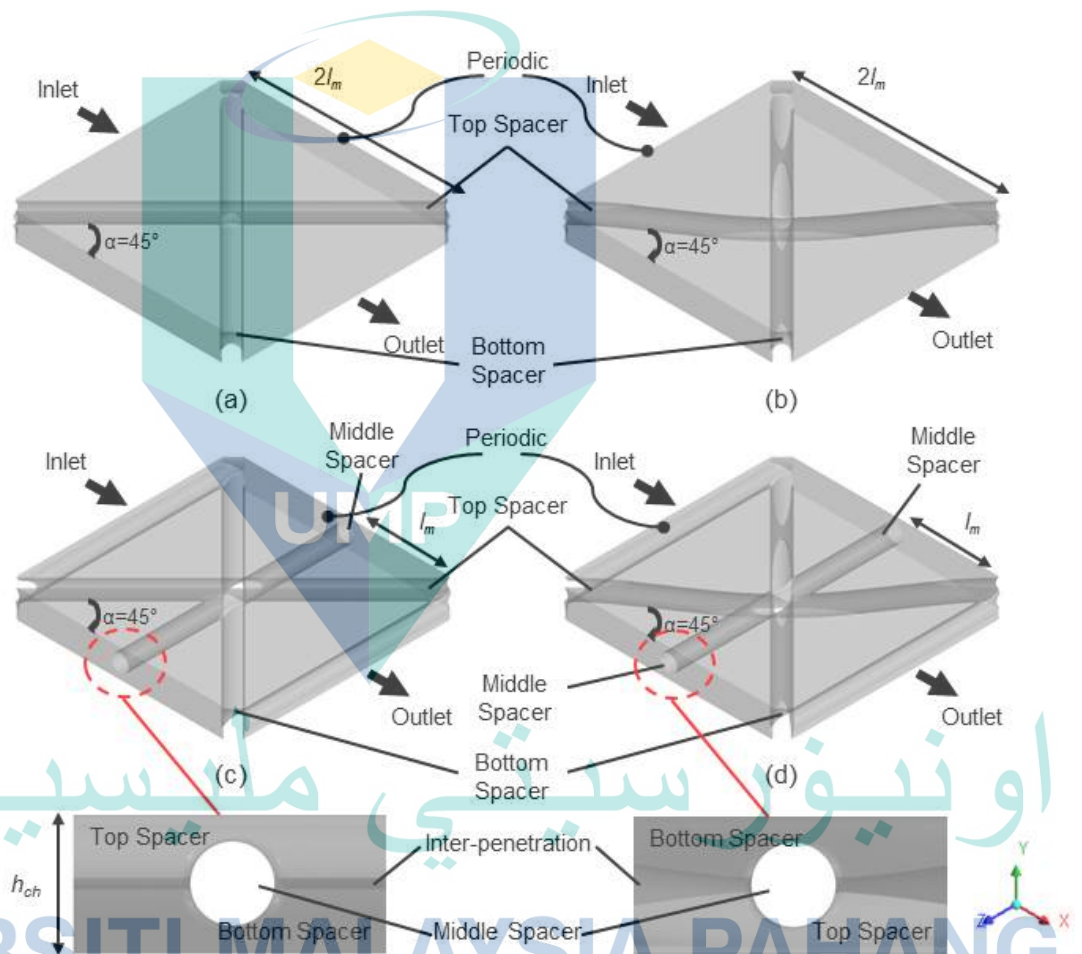
Figure 3.6 3D geometries of the spacer configurations modelled: (a) 2LNW; (b) 2LW; (c) 3LNW and (d) 3LW.

In this part, four types of spacer geometries are modelled, as illustrated in Figure 3.6: (a) conventional 2-layer non-woven spacer (2LNW); (b) 2-layer woven spacer (2LW); (c) 3-layer non-woven spacer (3LNW); and (d) 3-layer woven spacer (3LW). The 2LW, 3LNW and 3LW spacers are selected because they present woven and/or multi-

layer features, which are simple and commonly studied in the literature (Balster et al., 2006; Gu, Adjiman, et al., 2017; F. Li et al., 2005; Schwinge, Wiley, et al., 2004). Due to the filament diameter being more than half the channel height for the spacers simulated here, a small amount of intersection between filaments is required in order to ensure the spacer fits within the channel height (h_{ch}) of 1 mm (see Figure 3.6c and d).

3.3   Analysis of Results

For steady flow simulation, the area-averaged variables ($\bar{\phi}$) are calculated after the simulations have converged. As dimensionless numbers represent all identical physical system, reporting data in dimensionless form provides an easy way to change from one scale to another (scale up/down) (Ghernaout et al., 2018), thus in this study all data are reported in dimensionless form.

Of the important dimensionless variables used for RO system, the Sherwood number, Fanning friction factor and skin friction coefficient are the most relevant. The mass transfer can be expressed in dimensionless form using the hydraulic diameter and diffusivity as Sherwood number $\left(Sh = \dfrac{k_{mt} d_h}{D} \right)$, which represents the ratio of convective to diffusive mass transfer. The importance of wall shear stress in terms of fouling minimisation has been shown in the literature (Abid et al., 2017), and it can be defined as $\vec{\tau}_t = \mu \dfrac{\partial \left[\hat{\mathbf{n}} \times \left(\bar{\mathbf{v}} \times \hat{\mathbf{n}} \right) \right]}{\partial n}$. In terms of dimensionless wall shear stress, it can be reported as a skin friction coefficient $\left(\bar{f}_{skin} = \dfrac{\bar{\tau}_t}{\dfrac{1}{2} \rho u_{eff}^2} \right)$. In terms of dimensionless pressure drop, it can be evaluated using the Fanning friction factor $\left(f_{glob} = \dfrac{d_h}{2 \rho u_{eff}^2} \dfrac{\Delta p_{ch}}{L} \right)$. It should be noted that the friction factor is described by $f_{glob} = \dfrac{A}{\mathrm{Re}_h{}^n}$, where A and n depends on the spacer geometry and the flow condition.   For channel without spacer (empty channel), the

exponent *n* for laminar flow condition is 1. However, for channel with spacer, the exponent n is less than 1 (Alexiadis et al., 2007).

For unsteady flow simulations, the time-averaged Sherwood number ($\overline{Sh_{TA}}$) and Fanning friction factor ($f_{glob,TA}$) are measured as membrane performance indicators. In order to measure vortex strength, the λ_2 criterion is used where a more negative λ_2 value indicates stronger vortices that cause higher pressure loss (P. Xie et al., 2014).

In study of "floating" spacer, a parameter to measure the extent of the "floating" characteristics of the spacer, the floating ratio (R_f), is proposed and can be expressed by:

$$R_f = \frac{\text{Surface area of spacer not touching the membrane}}{\text{Total surface area of spacer}} \qquad 3.5$$

The total surface area in equation 3.5 takes into account the surface area of the spacer that is in contact with water as well as the spacer surface area that intersects the membrane surface.

3.4   Techno-Economic Model

3.4.1   Multi-scale Modelling

A multi-scale modelling approach solves multiple models at different scales (sizes or reference lengths) simultaneously to describe a system. In this work, correlations for the dependence of Sherwood number (dimensionless measure for mass transfer) and Fanning friction factor (dimensionless measure for pressure loss) on Reynolds number are taken from a small scale model (sub-millimetre) solved using CFD. These correlations are used to solve a large-scale model of the full-sized SWM module (i.e., a few metres in length) in order to predict the overall membrane module performance with respect to permeate flux and pressure drop.

Despite numerous spacer optimisation studies have been studied, it is difficult to increase mass transfer and reduce pressure drop simultaneously. However, some researchers (F. Li et al., 2005; Sreedhar et al., 2018a) argued that certain spacer geometries have promising results in terms of flux enhancement and pressure drop reduction. For instance, an optimal multi-layer structure (i.e., twisted spacer as middle spacer and non-woven net as outer layer) shows a Sherwood number approximately 30%

higher than an optimal non-woven spacer at the same energy consumption, and only about 40% of the energy consumption of the optimal non-woven spacer at the same Sherwood number (F. Li et al., 2005). Another recent study is the 3D advanced spacer based on triply periodic minimal surfaces (TPMS) proposed by Sreedhar et al. (Sreedhar et al., 2018a) who found 15.5% flux improvement for BWRO and up to 12.5% pressure drop reduction when compared to conventional spacer geometry. Thus, this paper explores the best-case scenario, and examines possible consequence of such development, by comparing the performance of a hypothetical advanced spacer that can consistently achieve a 50% higher Sherwood number (Sh) and a 50% lower Fanning friction factor (f_{glob}) than the conventional 2-layer non-woven spacer simulated.

The dependencies of Sh and f_{glob} on Reynolds number for the conventional spacer are obtained from Sections 3.2.1 and 3.2.2, and are as shown in Table 3.2. Those correlations are multiplied by factors of 1.5 and 0.5, respectively to yield the correlations for Sh and f_{glob} of the hypothetical advanced spacer as shown in Table 3.2.

Table 3.2   Correlations for the dependence of Sh and f_{glob} on Re_h for the conventional and advanced spacer configurations.

Spacer	Correlations	
Conventional spacer (2LNW)	$Sh = 2.44\,\mathrm{Re}_h^{0.61}$	$f_{glob} = 8.76\,\mathrm{Re}_h^{-0.62}$
Advanced spacer	$Sh = 3.66\,\mathrm{Re}_h^{0.61}$	$f_{glob} = 4.38\,\mathrm{Re}_h^{-0.62}$

It is important to note that the correlations for the conventional spacer (2LNW) were developed under the condition of impermeable wall. Nevertheless, it is possible to convert the data for an impermeable dissolving wall to a permeable membrane case under conditions where the ratio (ψ) of volumetric flux to impermeable mass transfer coefficient is below 20 (Geraldes & Afonso, 2006). Given that the values of ψ for all permeances considered in this paper are below 2, it is safe to assume that this correlation is valid for calculating the permeable wall mass transfer coefficient, for the conditions simulated in this paper.

The large-scale model solves a system of coupled 1D ordinary differential equations (ODEs) for the global and salt mass balances, as well as an ODE for pressure drop along the membrane module length:

$$\frac{dQ}{dx} = -\frac{A_m J}{\rho L}$$ 3.6

$$\frac{dw_b}{dx} = \frac{A_m J}{\rho Q L}\left(w_b - w_p\right)$$ 3.7

$$\frac{dp}{dx} = \frac{2\rho u_{eff}^2}{d_h} f_{glob}$$ 3.8

It shall be noted that the 1D ODE model in Equations (1) to (3) are derived based on first principle equation (viz. mass balance and fanning friction). These equations can be solved using a Runge-Kutta type method but require inputs such as permeate flux (J) and f_{glob}. In order to obtain these inputs for the different points along the SWM module, the k_{mt} and f_{glob} values are calculated from the correlations in Table 3.2, and then used to calculate the local flux values (Cohen-Tanugi et al., 2014; Mazlan et al., 2016; McGovern & Lienhard V, 2016; Shi et al., 2017; Wei et al., 2017; Werber et al., 2016). The details of the flux calculation methodology have been previously reported (Fimbres Weihs & Wiley, 2008), and can be found in Appendix A. Finally, the total volumetric flow rate for the permeate (Q_p) is calculated by integrating the flux along the module:

$$Q_p = \delta_{ch}\int_0^L \frac{J}{\rho}dx$$ 3.9

For simplicity, the flow is assumed to be isothermal and only the feed side is modelled, rather than both feed and permeate channel. This is because the permeate pressure is relatively small (i.e., 0.1 to 1 bar) compared to the inlet transmembrane pressure ($\Delta p_{tm,in}$) (i.e., of the order of 10 bar). In addition, Karabelas et al. (2018) found that the friction losses in the permeate channel only contributed about 0.1–0.4% of the total SEC. In terms of mass transfer, Avlonitis et al. (Avlonitis et al., 2007) found good agreement between their one-dimensional mass transfer model prediction and data obtained from operating RO seawater desalination plant. Thus, the assumption of 1D ODEs, that is, Equations 3.6, 3.7 and 3.8 is justifiable given that the pressure drop and

39

mass transfer vary mostly in the feed flow direction (Cohen-Tanugi et al., 2014). The results of the large-scale model are used to predict the total permeate flow rate and pressure drop, which are then used in the economic part of the model.

Table 3.3   Parameters for the cases modelled in this paper.

Parameter	Value for SW	Value for BW
Feed velocity, u_{avg} (m/s)	0.07−0.135	
Intrinsic rejection, R_{int} (%)	99.6	97
Membrane permeance, L_p (L m^{-2} h^{-1} bar^{-1})	1–10	3–10
Feed mass fraction, $w_{b,in}$	0.035–0.041	0.002–0.0035
Inlet transmembrane pressure, $\Delta p_{tm,in}$ (MPa)	6.5–8	1.5–2

The parameters used for the cases that are simulated using the large-scale model are tabulated in Table 3.3. In order to evaluate the cost-effectiveness of high permeance membranes, permeance ranges between 1 and 10 L m^{-2} h^{-1} bar^{-1} for seawater (SW), and between 3 and 10 L m^{-2} h^{-1} bar^{-1} for brackish water (BW) are considered. The choice of these ranges is justifiable following the remarkable progress in advanced materials for constructing membranes with high-permeance properties (Hu & Mi, 2013; Mi, 2014). The effect of membrane permeance on membrane performance is further discussed in section 6.1.

Since the $\Delta p_{tm,in}$ and feed flow conditions have notable effects on mass transfer and concentration polarisation (Lim et al., 2018), the conditions for optimising high permeance membrane performance may be different compared to the case using typical permeance membranes. Addressing these research questions is important in order to improve module design and develop membranes/spacers with better anti-fouling properties for desalination processes. In this work, $\Delta p_{tm,in}$ values in the range of 6.5–8 MPa and 1.5–2 MPa are used for SW and BW desalination, respectively. A lower $\Delta p_{tm,in}$ is used for BW desalination due to lower osmotic pressure of the feed solution in comparison to SW.

With respect to feed velocities, values between 0.07 and 0.135 m/s are considered for both SW and BW desalination. This range is within the flow velocities used in practice

(0.07–0.2 m/s (Bucs et al., 2015)) for a typical channel height ($\approx$ 1 mm). In addition, the highest value of flow velocity considered (i.e., $u_{avg} = 0.135$ m/s) is the value recommended by SWM manufacturers (DOW, 2018). This value corresponds to a Reynolds number (Re_h) of about 200. It is important to note that feed flow velocities in this range can be safely considered as laminar steady, as experimental studies based on Particle Image Velocimetry (PIV) show that flow unsteadiness only occurs for cross-flow velocities above 0.3 m/s (Bucs et al., 2015). Furthermore, the typical Reynolds number encountered in SWM feed channel is usually of the order of 100 (Horstmeyer et al., 2018; Jeong et al., 2020; Kavianipour et al., 2019; Qamar et al., 2019), which reinforce the laminar flow assumption used in this paper. The choice of feed water concentration for SW and BW shown in Table 3.3 is justifiable, given that seawater has an average total dissolved solid (TDS) of about 35,000 ppm, whereas brackish water has a concentration that is about one magnitude smaller than seawater (Greenlee et al., 2009). The effects of $\Delta p_{tm,in}$ and feed conditions (i.e., inlet velocity and concentration) are respectively discussed in sections 6.2 and 6.3.

Constant properties (i.e., viscosity and diffusivity) can be assumed for RO given that the flux and concentration polarisation for RO is much lower than for ultrafiltration (UF) (Gill et al., 1988). The diffusivity value used corresponds to a Schmidt number of about 600, which is representative of NaCl, the most abundant solute usually encountered in RO systems (Liang et al., 2018; Liang, Fimbres Weihs, Setiawan, et al., 2016), and which has been shown to be a good approximation for modelling the behaviour of seawater in desalination processes (Mistry & Lienhard, 2012).

3.4.2 Theoretical Background of Techno-economic Analysis

3.4.2.1 Techno-economic Analysis in a Typical RO Desalination Process

Figure 3.7 shows a schematic representation of a typical single-stage RO desalination process with 4 membrane elements per vessel. The feed solution (seawater or brackish water) is first treated (typically via a coagulation/flocculation process followed by media filtration) to reduce its turbidity level before being delivered to the membrane desalination process. In the desalination process, the water is pressurised to pass through the RO membrane to produce water of high purity (i.e., permeate). The rejected solution with much higher solute concentration (i.e., brine) is then passed through an energy recovery device (ERD) in which some of solution pressure is recovered. No

41

post-treatment is shown in Figure 3.7 because the cost associated with post-treatment is significantly lower than that of pre-treatment in a desalination process (Elazhar et al., 2015) and can thus be neglected. Overall, only three important processes, namely pre-treatment, pressurisation and membrane separation, are considered in this work for the simplified economic analysis of a typical RO desalination process.
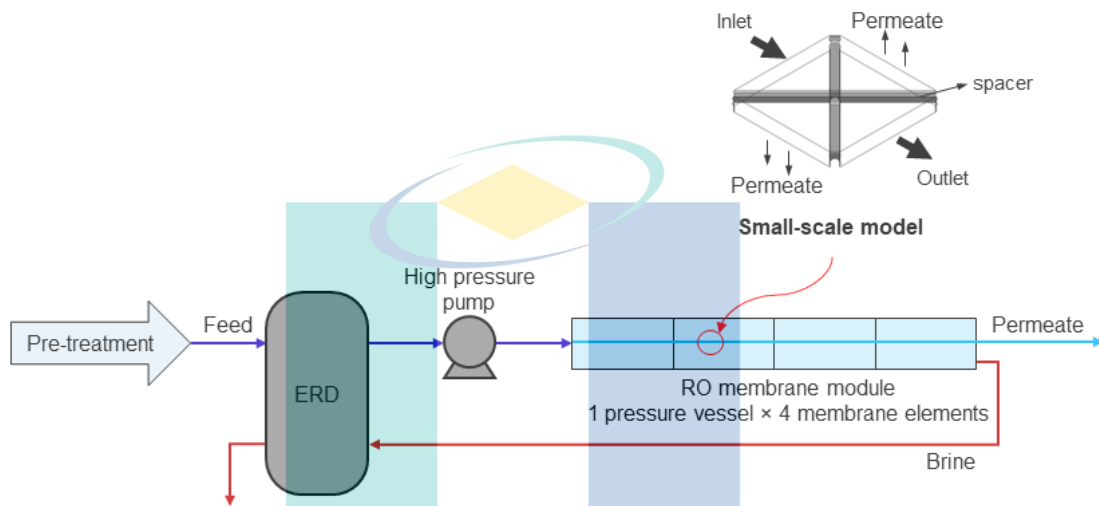
Figure 3.7   Schematic representation of typical RO desalination process

Techno-economic analysis is a crucial tool to analyse the cost-effectiveness of modifications to a process, by estimating the product selling price through consideration of engineering-based process design, economic computations and financial assessment (Quinn & Davis, 2015). An ideal techno-economic analysis would require a series of detailed calculations of material and energy balances, unit operational capital and operating cost estimations. Hence, a complete economic analysis would consider the costs of the entire desalination plant as well as several other parameters (e.g., salaries and interest rate) to determine the total water production cost. However, carrying out a complete economic analysis is very complicated because it can be greatly affected by geographical and time factors including human resources, equipment costs and interest rates. Nevertheless, simplifications to a complex economic analysis can be used to compare cost trends. The analysis proposed in this paper considers several key parameters in quantifying water cost, namely pre-treatment, operating pressure, pressure drop and capital expenses, in order to gain valuable insights into the effect of using advanced spacer geometries and high-permeance membranes.

3.4.2.2 Techno-economic Modelling

The cost of fouling and cleaning are usually proportional to the membrane area. Thus, these costs can be assumed to be included in the membrane cost (Fimbres Weihs & Wiley, 2008). Although the thin film nanocomposite (TFN) RO membranes manufactured by LG Chem (Verma et al., 2020) perform better than those of conventional TFC RO membranes, their market selling price is very close to each other to make them commercially competitive. In view of this, the cost of conventional and advanced RO membranes are assumed to be the same during analysis. The cost of the spacer mesh is also assumed to be included in the membrane cost given that the spacer is an inexpensive part of the SWM (Haidari et al., 2018b). As spacers are typically made of polypropylene (Balogun et al., 2019; Thomas et al., 2019), the cost between regular and advanced spacer design is assumed to be very similar. It should be noted that the simplified economic model used here only considers the changes in operational costs related to different spacers, i.e., conventional vs advanced spacer, and membrane permeance used by assuming all other costs such as pre-treatment, membrane capital and costs related to elevating the pressure to the operating condition remain constant. In this manner, this simple economic model can be used to compare different spacer designs in a like-for-like basis.

The simplified total processing cost (c_{total}) can be expressed as follows.

$$c_{total} = \frac{F_a}{t_{op}} A_m c_m + c_{pt} Q_f + \frac{c_e}{\eta_{pump}} \left[Q_f \left(p_{in} - p_a \right) - \eta_R Q_r \left(p_r - p_a \right) \right] \qquad 3.10$$

where the right-hand side terms of the equation are the amortised membrane capital cost, the feed pre-treatment cost and the pumping energy cost. In particular, energy recovery is taken into account by subtracting the recovered energy, that is the product of the retentate flow rate (Q_r), the retentate gauge pressure ($p_r - p_a$) and the pressure recovery efficiency (η_R) from the pumping energy required at the feed ($Q_f \Delta p_{tm,in}$). Dividing Equation 3.10 by the permeate flow rate (Q_p) and making use of the definitions for recovery rate ($R_r = Q_p/Q_f$), retentate flow rate ($Q_r = Q_f - Q_p$), inlet transmembrane pressure ($\Delta p_{tm,in} = p_{in} - p_a$) and channel pressure drop ($\Delta p_{ch} = p_{in} - p_r$), we obtain an equation for the total unit processing cost per unit permeate flow rate (C_{total}) as follows.

$$C_{total} = \frac{A_m c_m F_a}{Q_p t_{op}} + \frac{c_{pt}}{R_r} + \frac{c_e}{R_r \eta_{pump}} \left[\Delta p_{tm,in} - \eta_R (1 - R_r)(\Delta p_{tm,in} - \Delta p_{ch}) \right] \tag{3.11}$$

where the first term on the right-hand side of Equation 3.11 is the annualised capital cost of the membrane per unit of permeate (C_c), the second term is the pre-treatment cost per unit permeate (C_{pt}), and the last term is the energy cost per unit permeate. The last term can be further rearranged to identify the contributions to the energy cost due to the inlet operating pressure (C_{op}) and the pressure drop along the membrane module (C_{dp}):

$$C_{op} = \frac{c_e}{R_r \eta_{pump}} \left[1 - \eta_R (1 - R_r) \right] \Delta p_{tm,in} \tag{3.12}$$

$$C_{dp} = \frac{c_e}{R_r \eta_{pump}} \eta_R (1 - R_r) \Delta p_{ch} \tag{3.13}$$

The simplified total unit processing cost then becomes:

$$C_{total} = C_c + C_{pt} + C_{op} + C_{dp} \tag{3.14}$$

The typical parameters (Gastelum Reyes & Fimbres Weihs, 2016) used for the techno-economic analysis are summarised in Table 3.4.

Table 3.4 Case study parameters used for the techno-economic analysis.

Parameter	Values
Membrane area of module (A_m)	28 m^2
Number of envelopes (N)	14
Module length (L)	1 m
Channel width per membrane sheet (δ_{ch})	1 m
Number of modules per pressure vessel	4 units
Channel height (h_{ch})	1 mm
Energy cost (c_e)	$0.15/kWh
Membrane cost (c_m)	$40/m^2
Amortisation factor (F_a)	0.15/yr
Pump efficiency (η_{pump}) (Karabelas et al., 2018)	0.85
Operation time (t_{op})	7,500 h/yr
Retentate pressure recovery efficiency (η_R) (Cohen-Tanugi et al., 2014; Karabelas et al., 2018)	0 for BW, 0.95 for SW
Pre-treatment cost per unit feed (c_{pt})	$0.03/m^3

It shall be noted that the recovery rate obtained depends on the operating condition and intrinsic membrane permeance used. The range of recovery rate used in this study for SWRO and BWRO are 33−65% and 60−93%, respectively, which is similar to those used currently in the literature, i.e., 35−50% and 50−85% for standard SWRO and BWRO, respectively (Okamoto & Lienhard, 2019).

3.4.3 Comparison between Techno-economic Analysis and Specific Energy Consumption (SEC)

The available data for SEC in the literature (Cohen-Tanugi et al., 2014; Shrivastava et al., 2015) were used to compare with the results obtained from the techno-economic analysis in this work in order to establish confidence in the model prediction. This comparison is justified, given that the main component of the total processing cost (C_{total}) is the operating pressure cost, which contributes around 70–90% of the simplified total cost. Two cases from the literature which were examined under similar operating conditions as our work (i.e., $w_{b,in} = 0.032$ with $\eta_{pump} = 0.85$ for SWRO (Shrivastava et al., 2015) and $w_{b,in} = 0.002$ with $\eta_{pump} = 0.75$ for BWRO (Cohen-Tanugi et al., 2014)) are selected for comparison purpose. The main findings reported in the literature in terms of SEC (Cohen-Tanugi et al., 2014; Shrivastava et al., 2015) can be used to validate the trends for the economic analysis presented in this work, as highlighted in section 6.1.

CHAPTER 4

CFD STUDY ON THE EFFECT OF PERFORATED SPACER ON PRESSURE LOSS AND MASS TRANSFER IN SPACER-FILLED CHANNELS

4.1 Validation

Validation is an important step for the numerical approach presented in this paper before drawing conclusions on important mechanisms from this work. Data for perforated spacers are limited in the literature. To our best knowledge, only Kerdi et al. (2018) had studied perforated spacers numerically and experimentally. However, a direct validation against their work is not possible because of the use of different geometries. Nevertheless, some findings from their work can be used to confirm the trends observed for results of this work (Section 4.4.3).

4.2 Mesh Independence Study

To ensure a smooth mesh and avoid skewed mesh regions, the sharp edges in geometries modelled are smoothened using the blend function in ANSYS Workbench. A fine discretisation mesh in spacer geometries consisting of at least 20 inflation layers near the membrane and spacer surfaces are employed in this study. In addition, the minimum and maximum size of non-structured elements of the order of 0.1% and 1% of the channel height (h_{ch}), respectively are used.

The Grid Convergence Index (GCI) is used to estimate the discretization error considering the global variables (Fanning friction factor and mass transfer coefficient) used for measuring membrane performance. For 2D analysis, three meshes (1.6, 2 and 2.5 million) with a refinement ratio of 1.25 are considered. 3D analysis, on the other hand, requires significantly larger meshes than their 2D counterpart due to an additional dimension, and three different meshes (67, 78 and 97 million) are considered. It is worth noting that the total number of cells needed for 3D CFD analysis is more than 90 million and this requires 120 GB of memory (RAM) on an 8-core Xeon processor workstation

for each 3D steady state simulation. The mesh independence study reveals that a mesh comprised ~2.5 million cells for 2D, and ~90 million mesh for 3D is needed to achieve a GCI below 5% for both the Fanning friction factor and mass transfer coefficient. This gives an acceptable mesh resolution; hence this potential source of numerical errors can be safely ignored.

4.3 Effect of Wall Solute Concentration (w_w) on Mass Transfer (Sh)

Figure 4.1 shows the effect of wall solute concentration (w_w) on mass transfer (Sh) for 2D empty channel at Re_h of 200. A range of w_w from 0.01 to 0.1 is tested which corresponds to the typical solute concentration (of the order of 0.01 (Liang, Fimbres Weihs, Setiawan, et al., 2016)) at the membrane surface encountered for reverse osmosis operation. The result shows that the value of Sh at any location is very similar despite different value of w_w being used. Hence, this shows that the choice of w_w for impermeable-dissolving wall model is not important for calculation of Sh, and any value of w_w can be used for obtaining mass transfer results shown in sections 4.4.2 and 4.4.3.
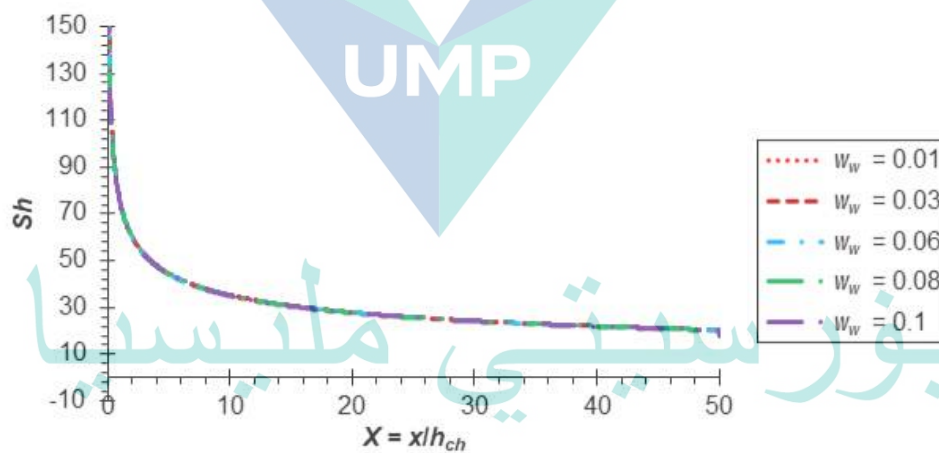
Figure 4.1 Effect of w_w on the computed Sh for 2D empty channel simulations.

4.4 3D Steady-state Flow Simulations

4.4.1 Comparison between Perforations of a Spacer Located in the Middle of the Channel against Perforations Near the Membrane Wall

Figure 4.2 compares the performance of spacer with perforation near the membrane wall with the perforation in the bulk flow for the same surface area of

perforation in terms of $\overline{Sh}$, f_{glob} and f_{skin} for different Re_h. The results show that perforated spacers yield similar $\overline{Sh}$, Fanning friction factor and skin friction coefficient to non-perforated spacers for all Re_h under consideration. This shows that the jet effect resulting from spacer perforations is insufficient to enhance the mixing effect of the flow under steady flow conditions. These data are further supported by the local mass transfer illustrated in Figure 4.3, where the mass transfer (Sh) distribution between non-perforated and perforated spacers is very similar regardless of jet effects caused by the perforated spacers.
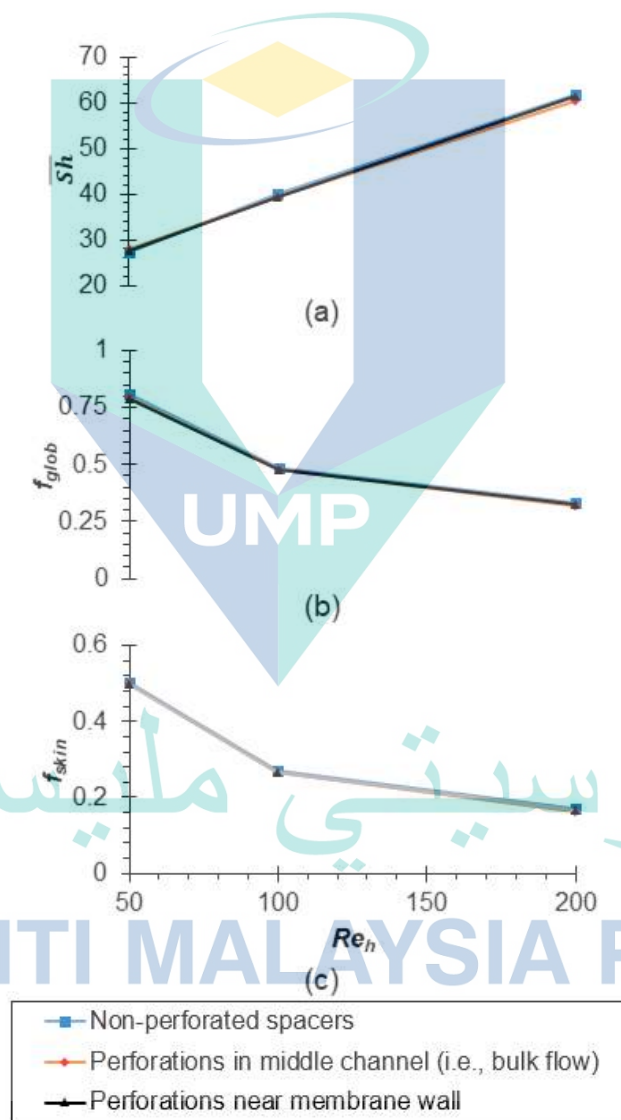
Figure 4.2 Effect of Re_h for different spacer geometries on (a) $\overline{Sh}$, (b) f_{glob} and (c) f_{skin}.
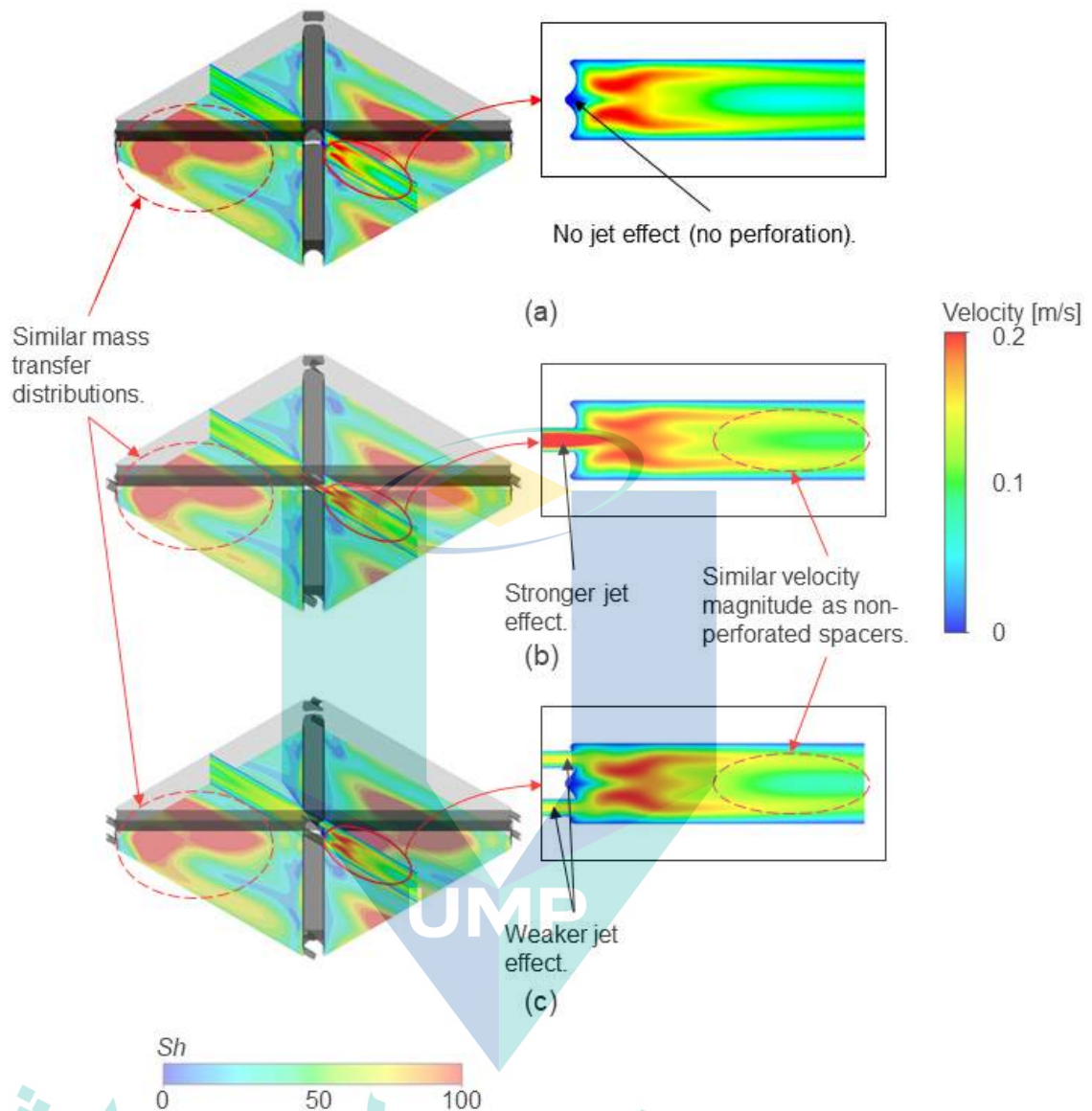
Figure 4.3   Surface profiles of *Sh* (*ZX*-plane) and plot of flow velocity (*XY*-plane) for spacers with (a) non-perforation, (b) perforations at middle of the channel and (c) perforations near the membrane wall for $Re_h = 200$

4.4.2   Effect of Perforation Size

Figure 4.4 shows that $\overline{Sh}$, f_{glob} and f_{skin} tend to decrease as perforation size (d_{per}/h_{ch}) increases. The significant decrease in mass transfer (by 14%) is supported by the results illustrated in Figure 4.5, where a lower mass transfer rate is observed on the membrane wall near the spacer for a larger perforation size. This is mainly because a larger perforation size weakens the flow velocity near the membrane surface (Figure 4.6). It is also interesting to note that there is a larger mass transfer near the perforation for the system with larger perforation (Figure 4.5), despite the decrease in overall mass transfer.
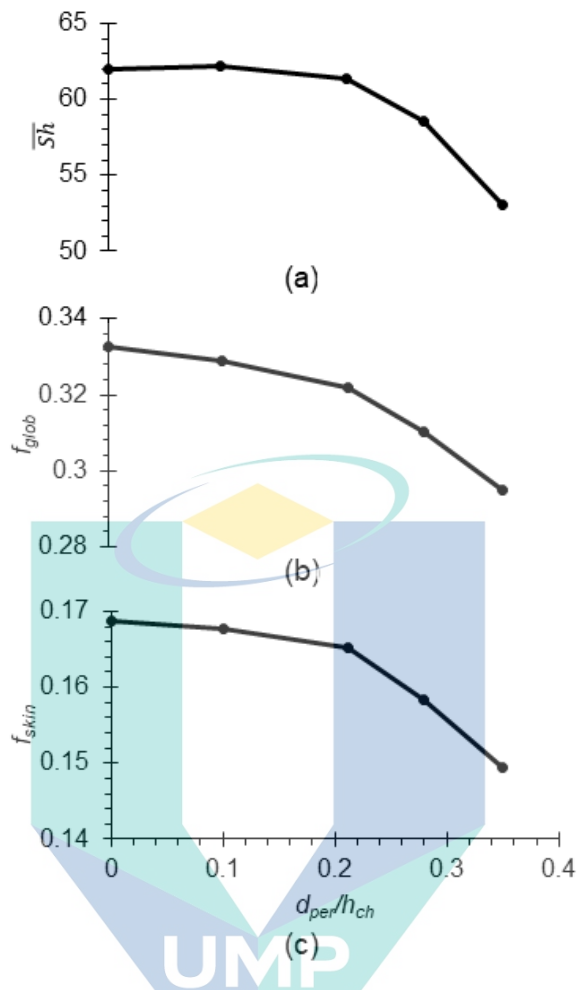
Figure 4.4   Effect of perforation size on spacer performance with respect to (a) $\overline{Sh}$,
(b) f_{glob} and (c) f_{skin}.

As shown in Figure 4.6, the decrease in flow velocity by large spacer perforation also causes less wall scouring, reducing the skin friction coefficient by 11% as perforation size increases (Figure 4.7). The decrease in f_{glob} with an increase in perforation size can be explained using the λ_2 plot shown in Figure 4.6, where it can be seen that the strength of vortices decreases, leading to a smaller pressure loss as perforation size increases. When the perforation size of a spacer is small or without perforation, recirculation regions are found downstream of the spacer and the streamlines within the recirculation regions form closed loops. However, when the perforation size becomes larger, the streamlines are not closed because of the incoming flow caused by the perforation. This phenomenon has weakened the vortices.
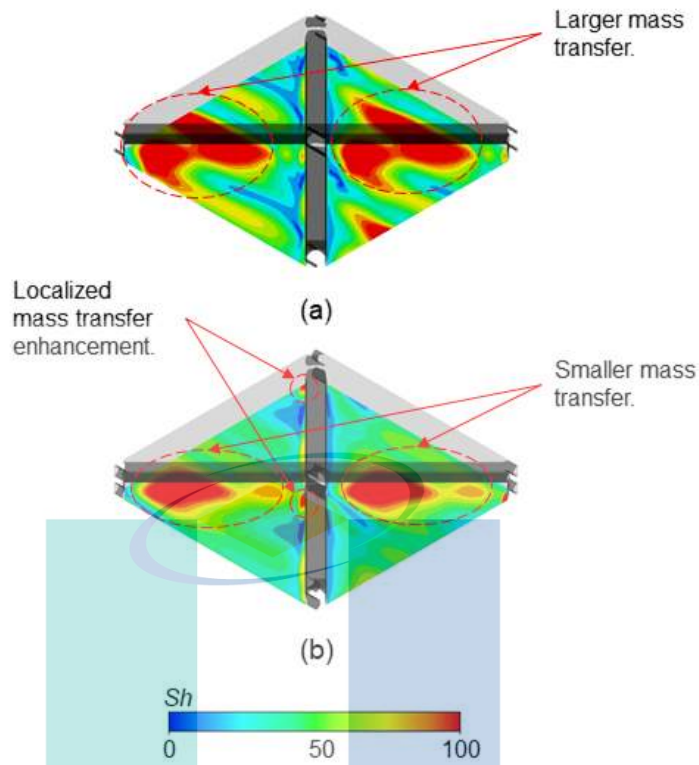
Figure 4.5 Surface profiles of *Sh* for spacers with (a) $d_{per}/h_{ch} = 0.1$ and (b) $d_{per}/h_{ch} = 0.35$.
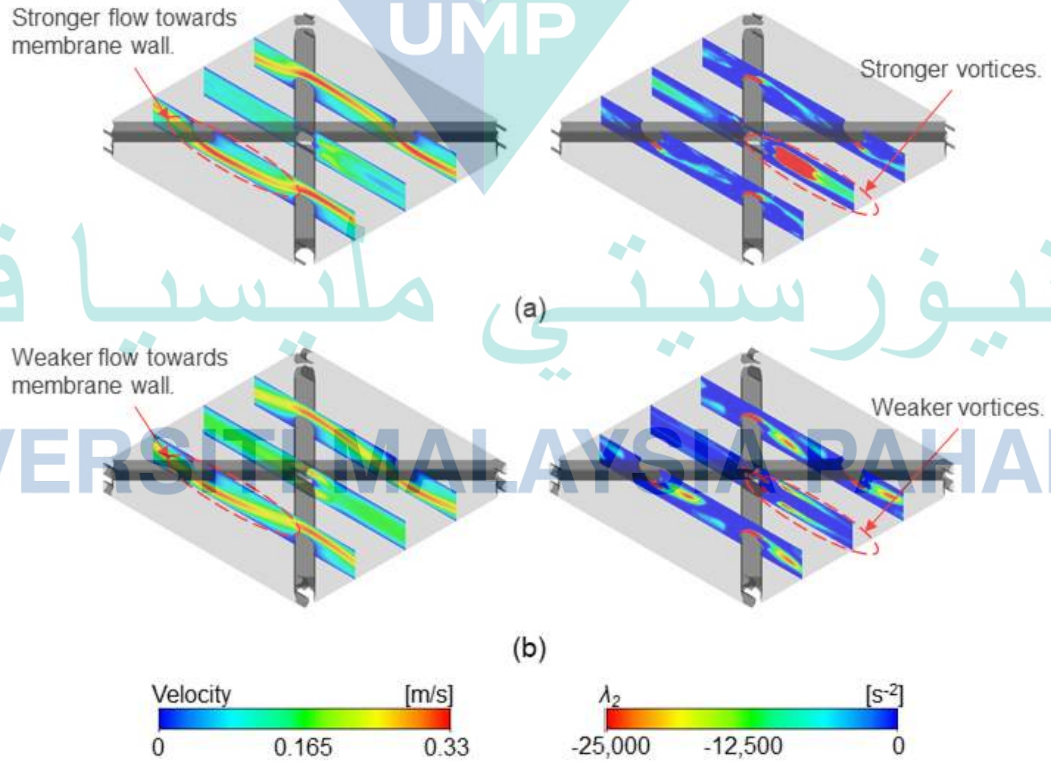
Figure 4.6 Plot of flow velocity and λ_2 for spacers with (a) $d_{per}/h_{ch} = 0.1$ and (b) $d_{per}/h_{ch} = 0.35$.
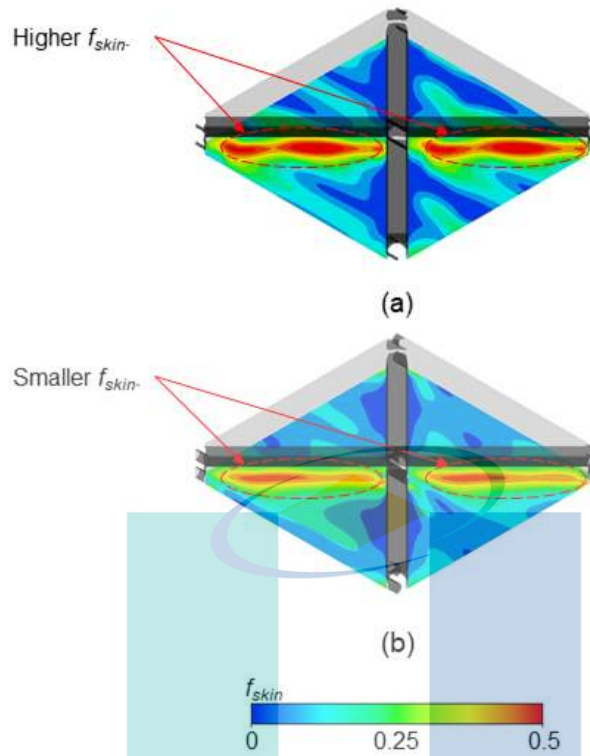
Figure 4.7 Surface profiles of f_{skin} for spacers with (a) $d_{per}/h_{ch} = 0.1$ and (b) $d_{per}/h_{ch} = 0.35$.

4.4.3 Effect of the Number of Spacer Perforations

Figure 4.8 shows that, under steady flow, the number of spacer perforations has a negligible effect on the $\overline{Sh}$ and f_{skin} of the membrane channel. Nevertheless, it must be pointed out that a larger number of spacer perforations tends to decrease the Fanning friction factor by 6% and thus reduce the pressure loss. The result is similar to the findings reported in the experimental work of Kerdi et al. (2018) in which the authors found that the pressure loss decreases as the number of perforations increases. This can be explained by the results shown in Figure 4.9, where the strength of the vortices downstream of the spacers decreases when more perforations are present.
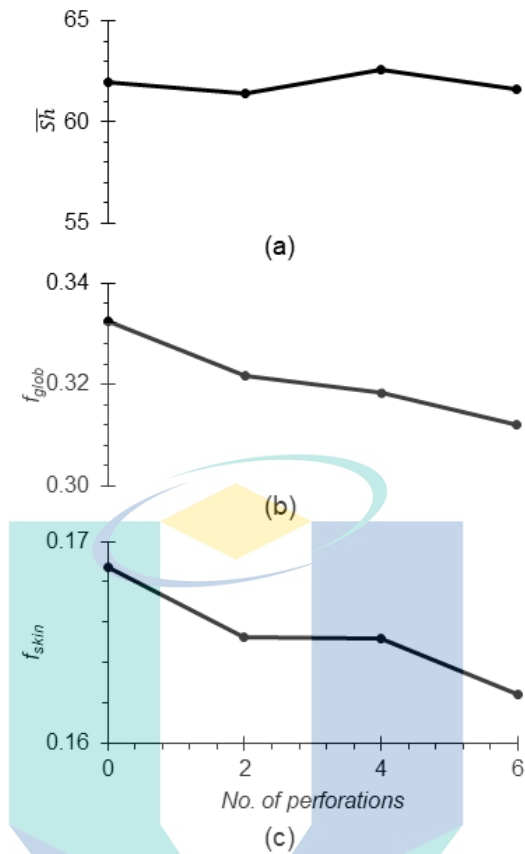
Figure 4.8   Effect of number of perforations on spacer performance with respect to (a) $\overline{Sh}$, (b) f_{glob} and (c) f_{skin}.
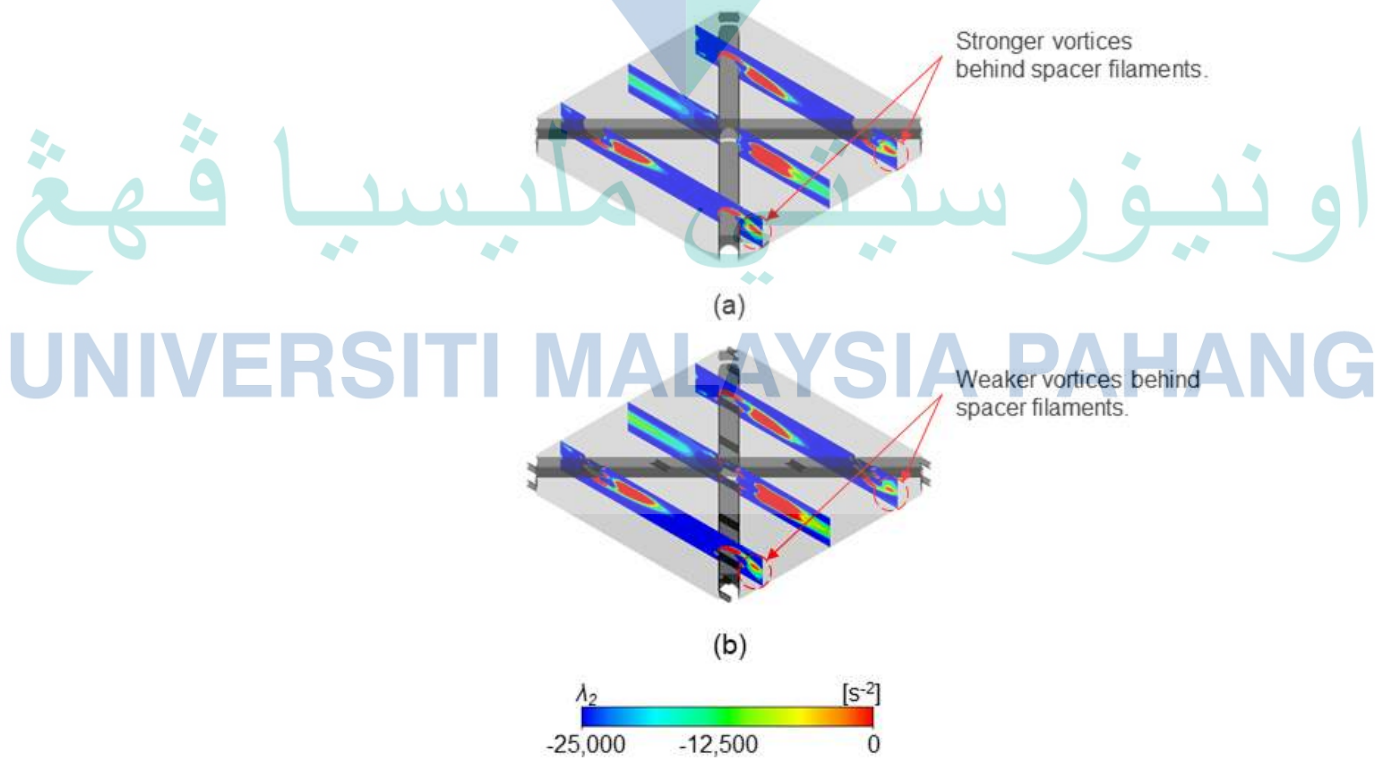

Figure 4.9   Plot of λ_2 for (a) 0-hole and (b) 6-hole spacer.

4.5   2D CFD Study on the Effect of Perforation Size on Membrane Performance Under Unsteady Flow
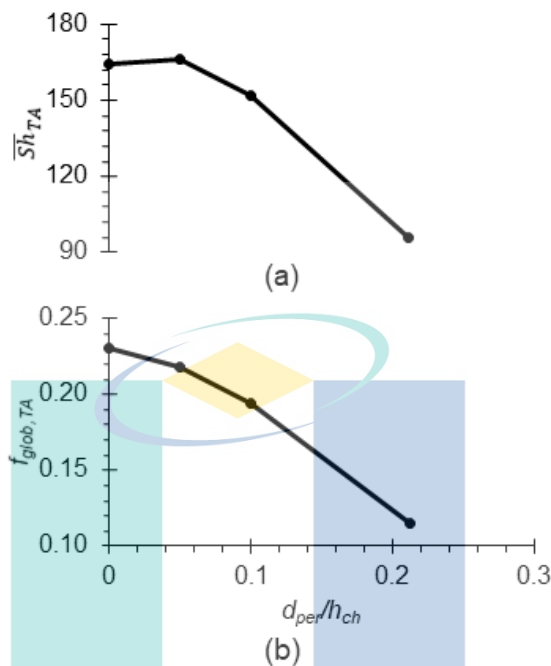
Figure 4.10   Effect of perforation size on 2D spacer performance with respect to (a) $\overline{Sh}_{TA}$ and (b) $f_{glob,TA}$.

Since spacer perforation size has a large impact on the mass transfer and pressure loss, this parameter was selected as the main parameter for the unsteady flow simulations. Figure 4.10 shows that time-averaged mass transfer ($\overline{Sh}_{TA}$) increases marginally by 1.4% by varying d_{per}/h_{ch} from zero to 0.05. However, at a larger d_{per}/h_{ch}, $\overline{Sh}_{TA}$ decreases dramatically by more than 40%. This can be explained by a relatively weaker λ_2 shown in Figure 4.11, where a larger d_{per}/h_{ch} suppresses the occurrence of vortex shedding, resulting in a significant reduction in boundary layer renewal and mixing (Figure 4.12). Nevertheless, it is possible to achieve a reasonable reduction in Fanning friction factor ($f_{glob,TA}$) by 5.6% at $d_{per}/h_{ch} = 0.05$ while showing a slightly higher $\overline{Sh}_{TA}$.
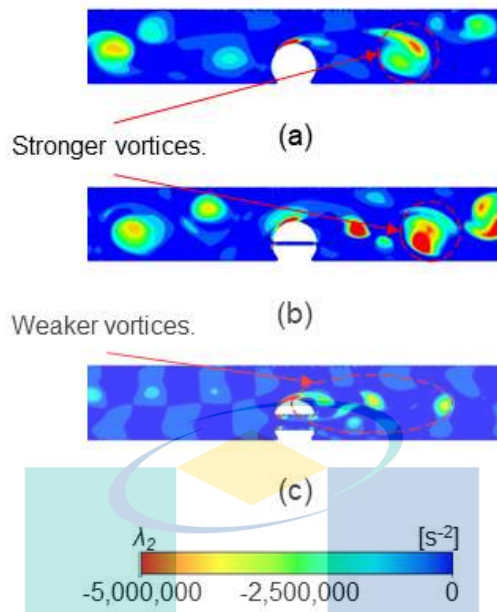
Figure 4.11 Plot of λ_2 for 2D spacers with (a) $d_{per}/h_{ch} = 0$ (no perforation), (b) $d_{per}/h_{ch} = 0.05$ and (c) $d_{per}/h_{ch} = 0.21$.
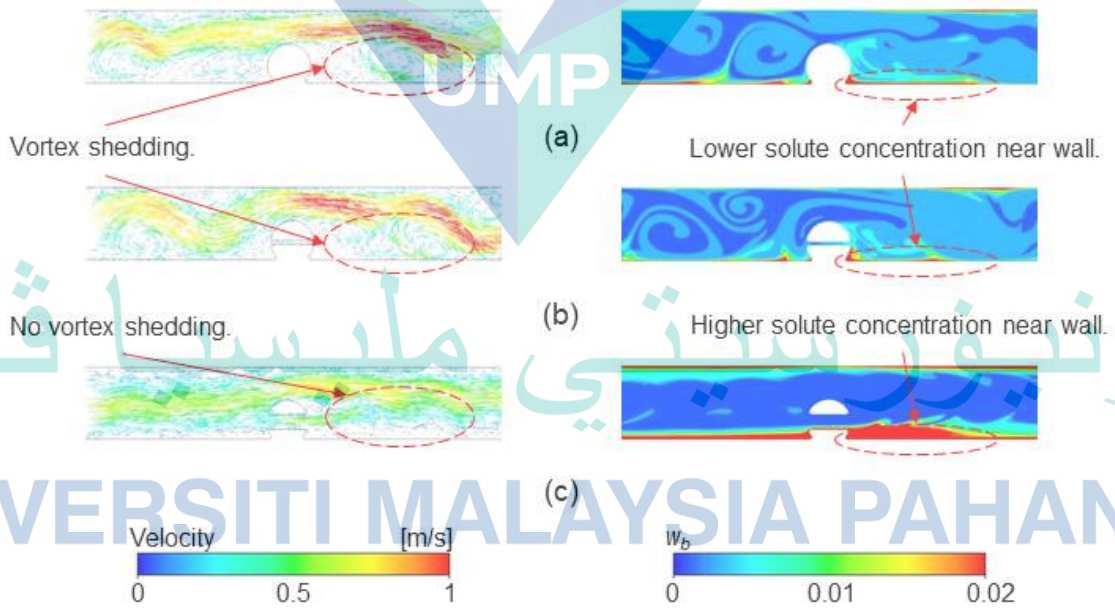
Figure 4.12 Plot of flow velocity and salt distribution for 2D spacers with (a) $d_{per}/h_{ch} = 0$ (no perforation), (b) $d_{per}/h_{ch} = 0.05$ and (c) $d_{per}/h_{ch} = 0.21$.

4.6   Conclusion

This thesis employed CFD simulations to study different aspects of spacer perforation (i.e., location, diameter and number of perforation) for a conventional spacer geometry (i.e., dual-layer non-woven spacer) and their effects on the hydrodynamics and mass transfer under both steady and unsteady flow conditions. It is found that spacer perforation does not improve mass transfer for the cases under consideration in this work. Our analysis shows that the effect of perforation location with the same surface area of perforation has insignificant impact on the dimensionless mass transfer (i.e., Sherwood number) and friction parameters (i.e., Fanning friction factor and skin friction coefficient).

A larger perforation size, however, could significantly decrease mass transfer by over 10% through weakening of flow velocity and suppression of vortex shedding. This is corroborated by a lower Fanning friction factor and skin friction coefficient as perforation size increases. Our simulation also found that a larger number of spacer perforations tends to decrease the Fanning friction factor by 6%, leading to reduced pressure loss. It is worth noting that the pressure loss reduction due to spacer perforation is associated with weaker vortices at the downstream of the spacer filaments.

CHAPTER 5

3D CFD STUDY ON HYDRODYNAMICS AND MASS TRANSFER PHENOMENA FOR SWM FEED SPACER WITH DIFFERENT FLOATING CHARACTERISTICS

5.1   Validation

Validation is a very important step for CFD simulations in order to provide confidence in the numerical results before important conclusions based on transfer mechanisms can be drawn. The importance of implementing a fine mesh near the surface of the spacer filaments as well as near the membrane surfaces for complex spacer geometries should be underlined, in order to capture the intricate velocity profiles. As only limited experimental data for woven and floating spacer configurations are available in the literature (Gu, Adjiman, et al., 2017; Schwinge, Wiley, et al., 2004), a direct validation against published results is thus not possible. This is mainly because the geometries considered in this work are different to those used elsewhere (Gu, Adjiman, et al., 2017; Schwinge, Wiley, et al., 2004). However, the main trends found in the literature (Gu, Adjiman, et al., 2017; Schwinge, Wiley, et al., 2004; Siddiqui et al., 2017) can be used to validate the trends for mass transfer and hydrodynamics for the woven and floating spacer geometries used in this work.

5.2   Mesh Independence Study

The discretisation meshes used in this study (see Figure 5.1) resulted in grid convergence indices (GCI) below 5% for both friction factor and mass transfer coefficient. In general, the meshing consists of two key features: 1) at least 20 inflation layers near the membrane and spacer surfaces and 2) minimum and maximum size of non-structured elements of the order of 0.1% and 1% of the channel height, respectively. The resulting GCI means that the grid resolution falls within an acceptable range (normally between 5% and 10%) (Fimbres Weihs & Wiley, 2010) and, therefore, this potential source of numerical error can be safely ignored.

Table 5.1   Meshing parameters.

Parameter	Value
Cell layers near spacer and membrane surfaces	30
Ratio of mesh minimum size to channel height	0.1%
Ratio of mesh maximum size to channel height	3 – 4%
Number of finite volumes (cells)	92 to 102.8 million
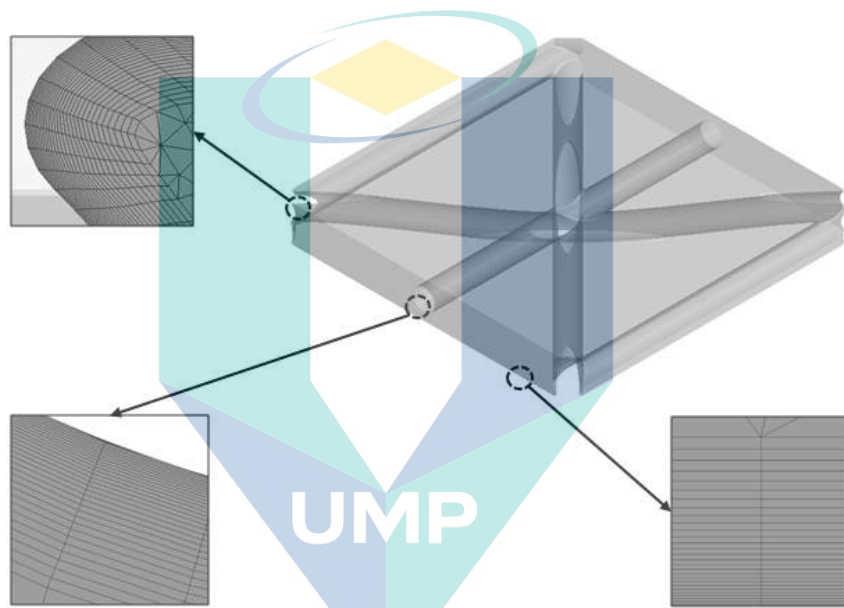
Figure 5.1   Example of surface discretisation mesh around spacer and membrane surfaces for 3LW spacer

5.3   Effect of Spacer Geometry

Table 5.2 Characterisation of the spacer geometries in terms of floating ratio (R_f), porosity (ε) and correlations for the dependence of Sherwood number (Sh) and global friction factor (f_{glob}) on Reynolds number (Re_h) for the same channel height (1 mm).

Spacer	R_f	ε	Correlations	
2LNW	0.7924	0.9036	$Sh = 2.44\,Re_h^{0.61}$	$f_{glob} = 8.76\,Re_h^{-0.62}$
2LW	0.9401	0.8989	$Sh = 2.97\,Re_h^{0.60}$	$f_{glob} = 12.38\,Re_h^{-0.62}$
3LNW	0.8692	0.8396	$Sh = 4.78\,Re_h^{0.50}$	$f_{glob} = 29.20\,Re_h^{-0.69}$
3LW	0.9632	0.8350	$Sh = 4.92\,Re_h^{0.49}$	$f_{glob} = 26.49\,Re_h^{-0.66}$

Table 5.2 shows the effect of spacer design under the same characteristic lengths ($\alpha = 45°$, $d_f/h_{ch} = 0.6$ and $l_m/h_{ch} = 4$), on floating ratio (R_f), porosity and the correlations obtained for the dependence of Sh and f_{glob} on Re_h. The correlations for the friction factor and Sherwood number are obtained based on Re_h in the range of 50 to 200.

Table 5.2 shows that, for the same geometric characteristics (α, d_f/h_{ch} and l_m/h_{ch}), the 3LW spacer shows the largest R_f and smallest ε. This is expected, given that the 3LW geometry exhibits the highest spacer volume inside the membrane channel in comparison to other spacer designs considered in this work. The filaments in this geometry also overlap the least with the membrane surface. The 2LW spacer, on the other hand, shows a larger R_f than the 3LNW spacer despite also having a larger ε. This is because the filaments in 2LW exhibit less intersection with the membrane, when compared to the 3LNW.

Table 5.2 also suggests that the dependence on Re_h for mass transfer is weaker for 3LW and 3LNW spacers than for the 2LW and 2LNW spacers. This can be beneficial for high-permeance membranes, where large permeate fluxes can lead to high recovery (Lim et al., 2018), greatly reducing the flow rate in the feed channel and negatively impacting mass transfer. A combination of a smaller exponent and a larger coefficient in the Sh dependence of Re_h for 3-layer spacers can therefore lead to relatively sustained mass transfer enhancement despite lower flow rates.

Figure 5.2 shows the dependency of mass transfer, wall shear and friction factors on R_f and ε for Re_h from 50 to 200. The straight lines in Figure 5.2 refer to the respective trendlines (with certain R-squared values). It is interesting to note that the slope for the change in k_{mt}, f_{glob} and τ_t with respect to changes in R_f when going from a non-woven to a woven structure, is steeper for the 2-layer spacers than for the 3-layer spacers for all Re_h. This indicates that the performance of 2-layer spacer in terms of mass transfer and friction parameters (i.e., f and τ_t) is more sensitive to the change in its woven structure than the 3-layer spacer. In addition, higher k_{mt}, τ_t and friction factors are found for lower ε or higher R_f The trend for f_{glob} shown in Figure 5.2 agrees with the trend observed by Siddiqui et al. (2017) who found that pressure loss decreases as ε increases. This confirms that an increase in ε generally reduces k_{mt}, τ_t and friction factors under the same geometric characteristics. The results in Figure 5.2 also show a much higher R-squared correlation

coefficient on ε ($0.71 < R^2 < 0.97$) than on R_f ($0.27 < R^2 < 0.67$). This means that the membrane performance is more likely to depend on ε than on R_f.
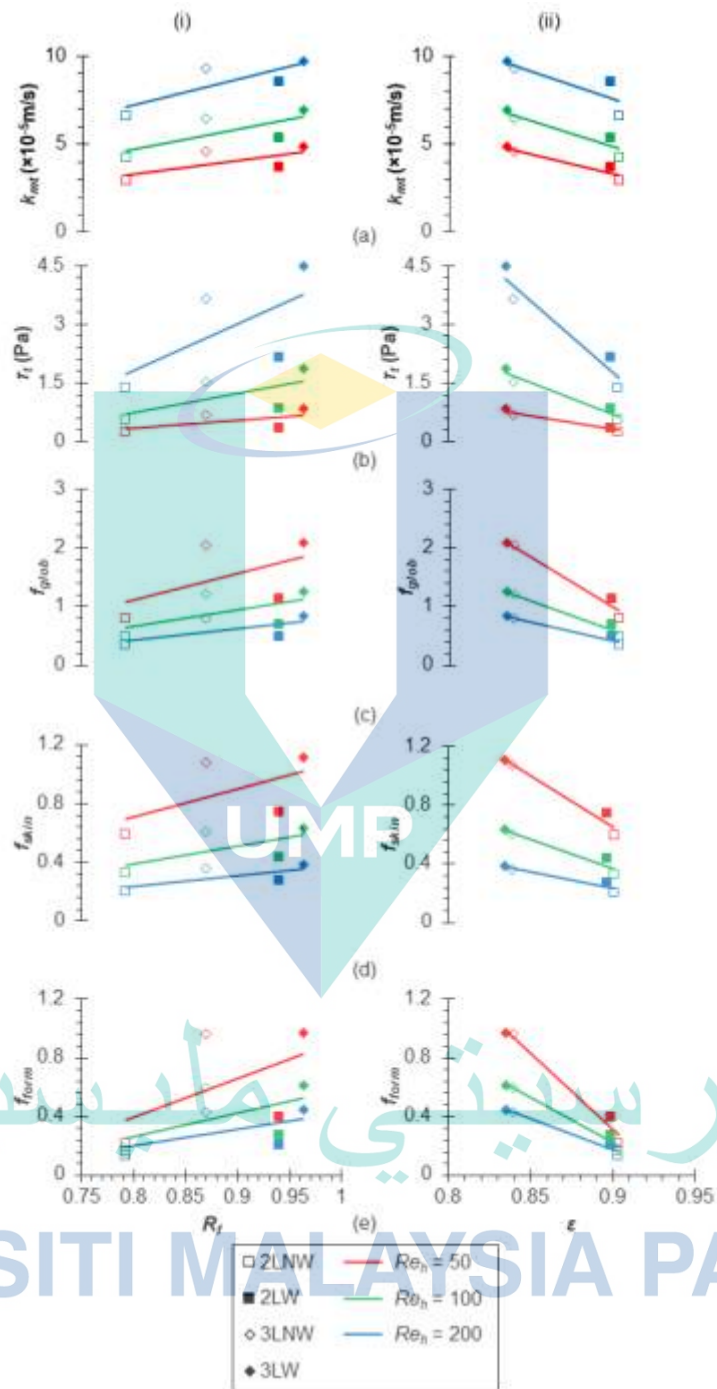
Figure 5.2   Effect of (i) floating ratio (R_f) and (ii) porosity (ε) on (a) mass transfer coefficient (k_{mt}), (b) wall shear stress (τ_t), (c) global friction factor (f_{glob}), (d) skin friction (f_{skin}), and (e) form friction (f_{form}) for different spacer geometries at different Re_h.
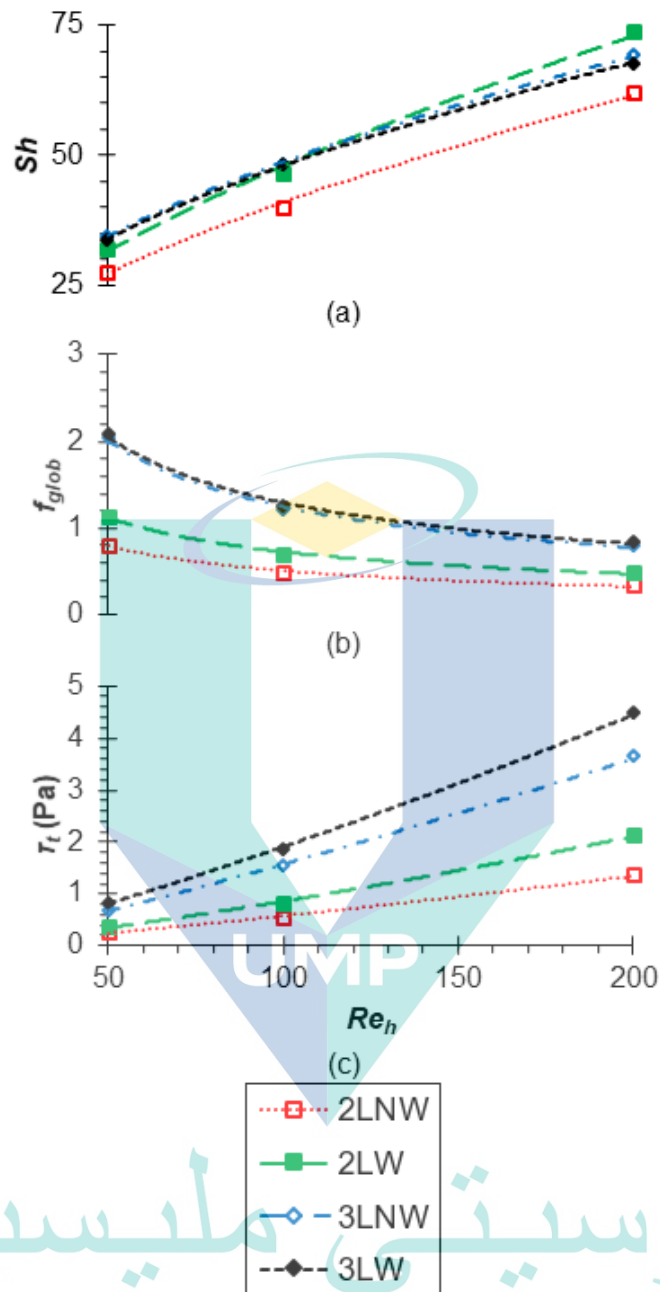
Figure 5.3   The impact of Re_h for different spacer geometries on (a) Sh, (b) f_{glob}, and (c) τ_t.

Figure 5.3 shows the dependency of Sh, fglob and τt on Reh for different spacer geometries. As can be seen, the 2LW spacer performs better at a higher Reh of 200 in terms of dimensionless mass transfer (i.e., Sh) than the 3-layer spacer geometries, but shows lower mass transfer at a lower flow (Reh < 100). This trend can be explained by ehe solute concentration distribution (XY-plane) as presented in Figure 5.4, where at a higher flow rate (Re_h = 200), the woven structure of 2LW spacer promotes the flow of low concentration fluid towards the membrane surfaces due to a stronger streamwise

61

vortex downstream from the filament intersection (as indicated in Figure 5.4 by larger magnitude of λ_2 in streamwise direction). This, as a result, leads to greater boundary layer disruption and mass transfer than for the other spacer geometries under consideration.

Although 3LW also exhibits woven characteristics, the middle layer of 3LW restricts the occurrence of strong streamwise vortex downstream from the filament intersection. Hence, the 3LW spacer shows less mass transfer enhancement than the 2LW geometry. This agrees with our previous observation (see Figure 5.2) that R_f is not the determining factor that drives mass transfer enhancement. It must be noted that 3LW does not perform well as expected because the benefits offered by the woven structure in promoting the large streamwise vortex are limited by its middle layer filament. The λ_2 data in Figure 5.4 confirms this analysis since no streamwise vortex is formed downstream from the intersection of the top and bottom filaments.

On the other hand, at a lower flow rate ($Re_h = 50$) the occurrence of vortical flow in the 2LW spacer is rather weak (Figure 5.5). This is because creeping flow dominates the membrane channel at low values of Re_h, causing less occurrence of fluid mixing near the membrane. Hence, 3-layer spacers (3LNW and 3LW) show more mass transfer enhancement than the 2LW geometry. Figure 5.4 and Figure 5.5 also show comparably less solute accumulation near the spacer filaments for the 2LW geometry than for 2LNW. This observation agrees with the results of Gu, Adjiman, et al. (2017), for which the woven spacers show less contact with the membrane surface, hence resulting in a smaller solute accumulation near the spacer and CP.

Figure 5.3 also shows that the 3LW spacer presents the highest f_{glob}, followed by 3LNW, 2LW and finally 2LNW spacer. This is because woven and/or 3-layer spacers occupy more volume in membrane channel than the 2-layer non-woven spacers, leading to more obstacles in the path of the fluid flow and resulting in higher pressure loss due to form drag. The result is further supported by the data shown in Figure 5.54, where 3LW spacer shows the largest regions of high λ_2, followed by 3LNW, 2LW and 2LNW spacer. Our results are also in line with the outcomes reported in the work of Gu, Adjiman, et al. (2017) and Schwinge, Wiley, et al. (2004) in which both studies report that woven and middle spacers result in greater pressure drop than non-woven spacers.
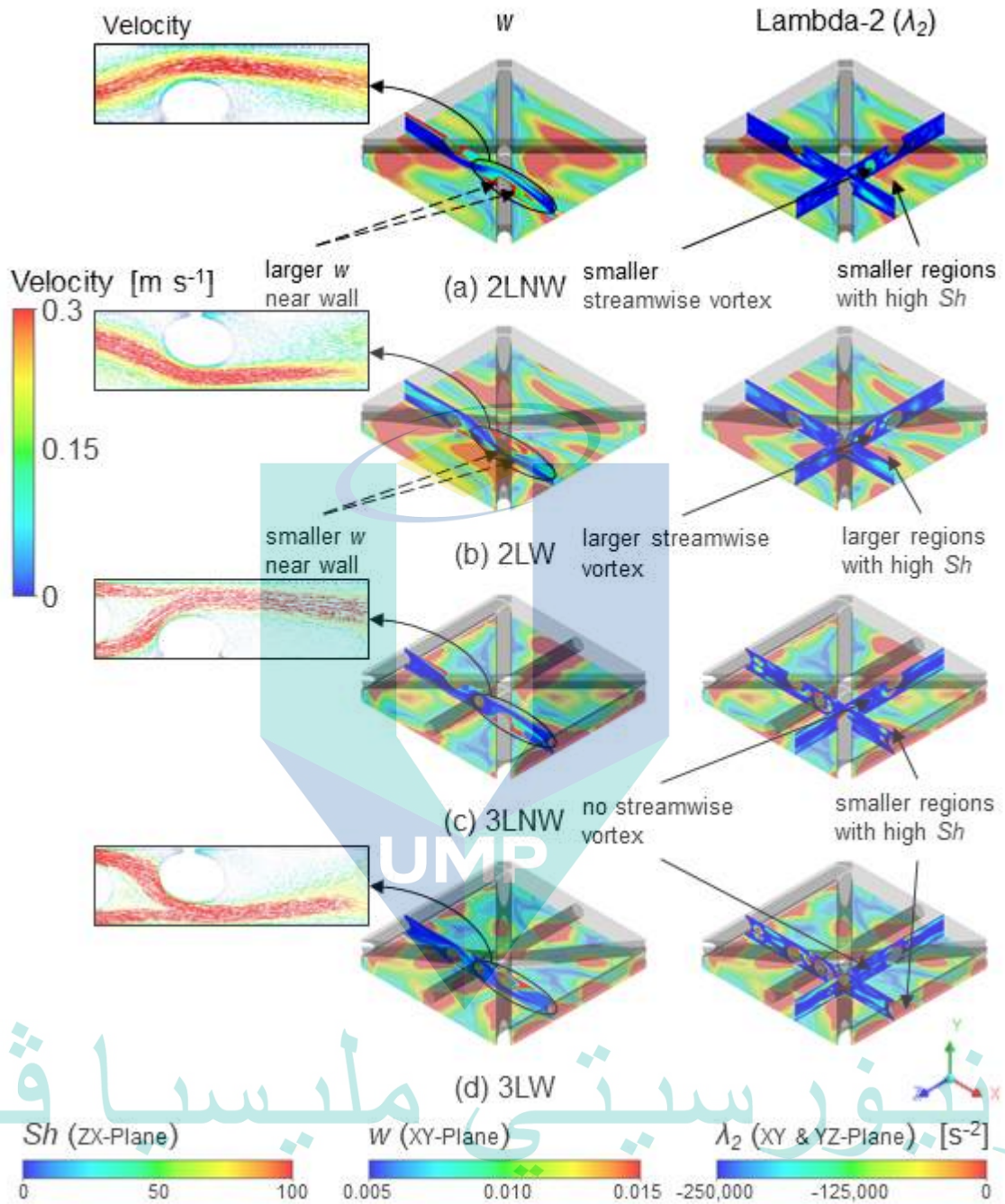
Figure 5.4   Vector plot of velocity, contour plot of salt concentration (w) and Lambda-2 (λ_2), and surface profile of dimensionless mass transfer (Sh) for the different spacer geometries analysed at $Re_h = 200$: (a) 2LNW; (b) 2LW; (c) 3LNW and (d) 3LW.
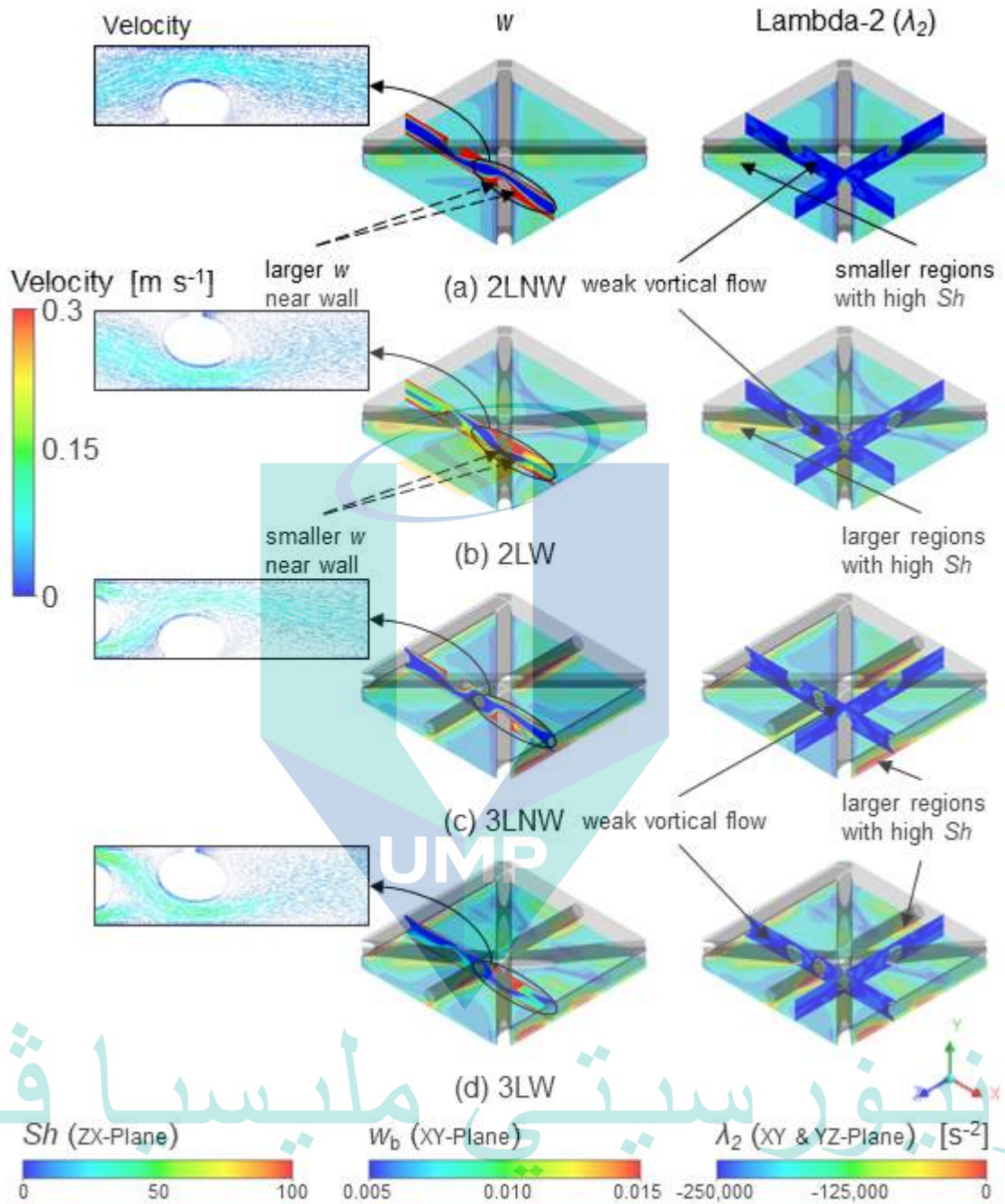
Figure 5.5   Vector plot of velocity, contour plot of salt concentration (w) and Lambda-2 (λ_2), and surface profile of dimensionless mass transfer (Sh) for the different spacer geometries analysed at $Re_h = 50$: (a) 2LNW; (b) 2LW; (c) 3LNW and (d) 3LW.
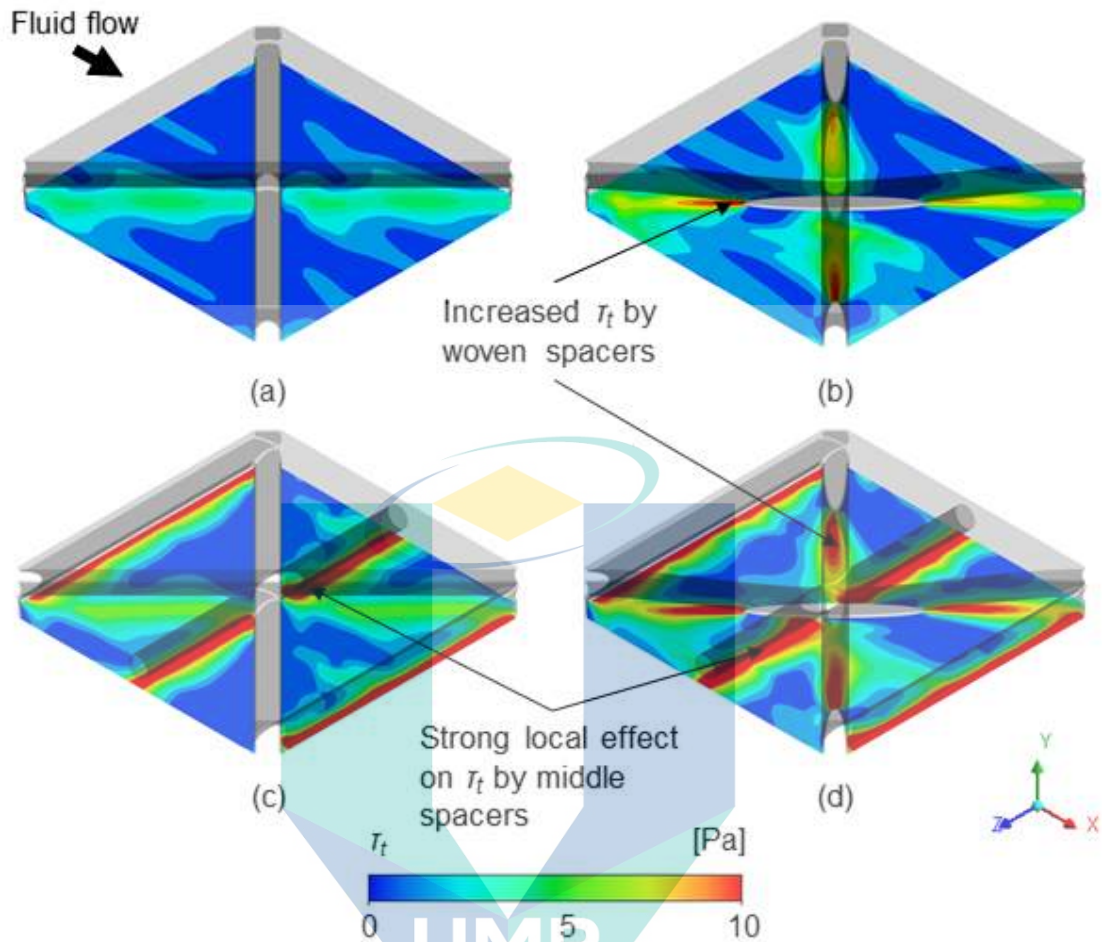
Figure 5.6   Surface profiles of τ_t, for the different spacer geometries analysed at Re_h = 200: (a) 2LNW; (b) 2LW; (c) 3LNW and (d) 3LW

The large pressure loss for the 2LW, 3LNW and 3LW spacers is also corroborated by higher wall shear. This is shown in Figure 5.6, where the obstructions to fluid flow presented by the woven or/and middle spacers create a larger scouring effect, leading to stronger wall shear and potential of reducing membrane fouling. Interestingly, the results show that the 3-layer spacers exhibit a significantly larger wall shear (i.e., over one order of magnitude) than any 2-layer spacer under consideration at any Re_h (Figure 5.3). In addition, Figure 5.3 shows that a significantly larger wall shear can be achieved when using a 3-layer spacer (i.e. > 160% increase compared to 2LNW spacer) than using a woven structure (i.e. > 40% increase compared to 2LNW spacer).

65

5.4   Conclusion

This thesis investigates the measure of "floating" characteristics as a measure to increase shear stress and enhance transport phenomena in spacer-filled channel. The simulated data presented in this work suggest that the performance of 2-layer spacers with respect to mass transfer and friction parameters is more sensitive to the changes in the physical structure (i.e., from non-woven to woven) compared to the 3-layer geometries. The results also suggest that R_f is not a determining factor that drives SWM mass transfer enhancement. Rather, it is the geometry (2- or 3-layer spacer) that plays the key role. The λ_2 analysis suggests that the 3-layer spacer (3LNW and 3LW) did not perform as good as expected because the middle filament layer tends to disrupt the formation of a large streamwise vortex downstream of the intersection between top and bottom filaments at Re_h 200, hence showing smaller mass transfer than the 2LW geometry.

At a lower flow rate ($Re_h < 100$), vortical flow in the 2LW spacer is rather weak because creeping flow dominates, causing less occurrence of membrane region with fluid mixing. Thus, 3-layer spacers (3LNW and 3LW) show more mass transfer enhancement than 2-layer spacers (2LNW and 2LW). Nevertheless, 3-layer spacers outperformed 2-layer counterparts in terms of wall shear by at least one order of magnitude, showing a larger potential for long-term fouling reduction albeit at the expense of a larger pumping energy. The analysis also revealed that a significantly larger wall shear could be attained if a 2-layer spacer structure is replaced by a 3-layer spacer compared to changing the design from non-woven to woven.

CHAPTER 6

THE TECHNO-ECONOMIC CASE FOR COUPLING ADVANCED SPACERS TO HIGH-PERMEANCE RO MEMBRANES FOR DESALINATION

6.1 Effect of Intrinsic Membrane Permeance

Figure 6.1 shows the local permeate flux values along the membrane module for SWRO and BWRO, at the lower and upper limit of permeance, for conventional (CS) and advanced spacers (AS). For the region close to the inlet of the membrane module (i.e., $x < 0.6$ m for SWRO and $x < 2$ m for BWRO) for a high-permeance membrane, the advanced spacer shows the largest permeate flux because it yields the largest Sh and a lower pressure drop at a given Reynolds number (as predicted by the expressions in Table 3.2). However, the large flux also results in a quick reduction of the Reynolds number along the module, which leads to a reduction in mass transfer. The fast decrease in Reynolds number along the channel explains why the conventional spacer (2LNW) shows greater flux than the advanced spacer closer to the module outlet (i.e., $x > 0.6$ m for SWRO and $x > 2$ m for BWRO) for the high-permeance membranes. A similar trend is also observed for the low-permeance membranes, albeit at a larger membrane length (i.e., $x > 4$ m for SWRO and $x > 5$ m for BWRO, not shown in Figure 6.1).

It is also important to note that the permeate flux for a high-permeance membrane approaches zero at a shorter module length (i.e., $x \approx 2$ m for SWRO and $x \approx 4$ m for BWRO) than for the low-permeance membrane. This means that a careful selection of module length for high-permeance membranes is paramount, because the membrane area is wasted in the downstream region where flux is near-zero. It has been reported that the SEC for BWRO remains unchanged when the number of membrane modules exceeds 4 units (Qiu & Davies, 2012). Thus, for simplicity of analysis, 4 modules (or an effective membrane length of 4 m in a single pressure vessel) is used for the techno-economic analysis for both BWRO and SWRO in the latter part of this study.
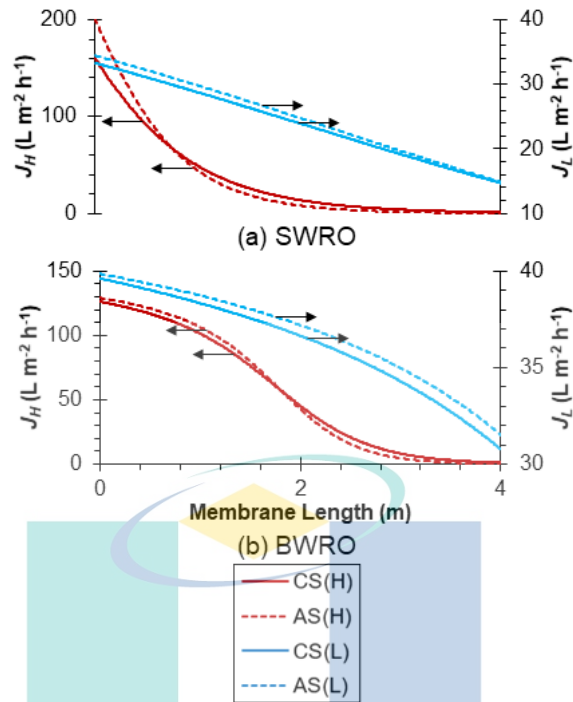
Figure 6.1 Local permeate flux along membrane module for the conventional (CS) and advanced spacers (AS), for (a) SWRO and (b) BWRO at the same inlet TMP ($\Delta p_{tm,in,\,SW}$ = 6.5 MPa and $\Delta p_{tm,in,\,BW}$ = 1.5 MPa). 'L' and 'H' in the figure legend denote low (L_{p},SW = 1 L m^{-2} h^{-1} bar^{-1} and L_{p},BW = 3 L m^{-2} h^{-1} bar^{-1}) and high (L_{p},SW = L_{p},BW = 10 L m^{-2} h^{-1} bar^{-1}) intrinsic membrane permeance, respectively

For a given membrane length (i.e., 4 m as indicated in Table 3.4), Figure 6.2 shows the effect of the advanced spacer on total processing cost (C_{total}) and recovery rate (R_r) as the membrane permeance is varied. It can be observed that the advanced spacer considered reduces C_{total} by only 1–2% at a low-permeance for both SWRO and BWRO. At a larger membrane permeance, on the other hand, advanced spacer shows negligible changes in C_{total} and R_r compared to the conventional spacer for both SWRO and BWRO. This is because of the trade-off between local flux and mass transfer along the membrane channel, as shown in Figure 6.1. However, the data suggest that an advanced spacer would result in a larger average flux if a shorter membrane length is used and can therefore lower processing costs compared with the conventional spacer.
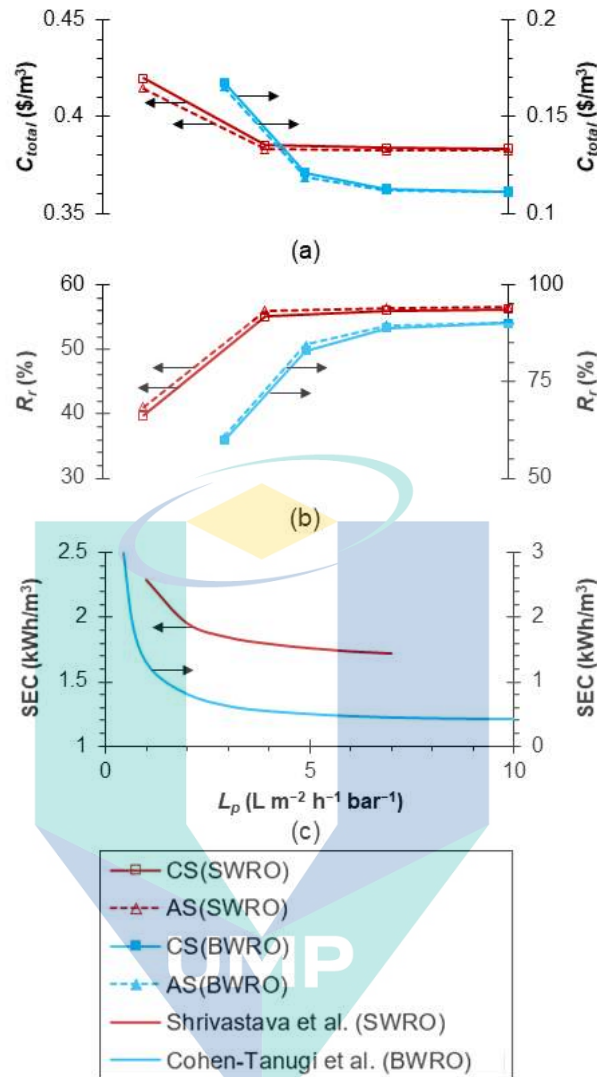
Figure 6.2 Effect of intrinsic membrane permeance on (a) total processing cost (C_{total}), (b) recovery rate (R_r) and (c) specific energy consumption (Cohen-Tanugi et al., 2014; Shrivastava et al., 2015) at the same inlet TMP ($\Delta p_{tm,in,\ SW} = 6.5$ MPa and $\Delta p_{tm,in,\ BW} = 1.5$ MPa)

When the feed flow rate is substantially decreased along the membrane channel due to a larger permeate flux, a tapered-array configuration might be the best configuration for high-permeance membrane. In such an array, there would be more modules in parallel in the first section, followed by subsequent sections with less modules in parallel. Higher recovery is attainable because a tapered-array configuration allows a reduction in cross-sectional area over the series array configuration; hence, it is more suitable for systems with a significant reduction in cross-flow due to permeation (Schwinge, Neal, et al., 2004). The key challenge in optimising such a design is identifying the critical cross-flow velocity at which it is not economical or viable to

69

increase the membrane module length. However, this could be achieved using the multi-scale modelling analysis presented in section 3.4.1.

Figure 6.2 also shows that the total processing cost for brackish water and seawater can be significantly reduced by 32% and 7.5%, respectively, when the L_p is increased to 10 L m^{-2} h^{-1} bar^{-1}. These results agree with the simulation findings reported in the work of Cohen-Tanugi et al. (Cohen-Tanugi et al., 2014) in which the energy savings for brackish water (46%) are greater than that of seawater (15%) when L_p is tripled. This is because the recovery rate (or flux) for BWRO (61% to 90%) increases at a faster rate than for SWRO (40% to 56%). However, the total cost remains unchanged at a higher L_p (> 4 L m^{-2} h^{-1} bar^{-1} for seawater and > 7 L m^{-2} h^{-1} bar^{-1} for brackish water), suggesting there is no benefit in increasing L_p in the case where module length increases beyond 4 m. This trend is similar to findings reported by Shrivastava et al. (Shrivastava et al., 2015) and Cohen-Tanugi et al. (Cohen-Tanugi et al., 2014) (Figure 6.2c) in which they found that energy savings are negligible when L_p exceeds 4 and 5 L m^{-2} h^{-1} bar^{-1} for seawater and brackish water, respectively. Thus, this provides confidence in the techno-economic model predictions presented in this paper.

The reason why the total processing cost remains similar at a higher L_p can be explained by a larger average CP and a lower average k_{mt} (Figure 6.3) at a higher L_p, which limit further increases in R_r or flux as L_p increases. Moreover, the combined two factors (i.e., larger CP and lower k_{mt}) could lead to a larger tendency of scaling/fouling and decreased water flux, even though those effects are not being considered in the calculation in this paper.
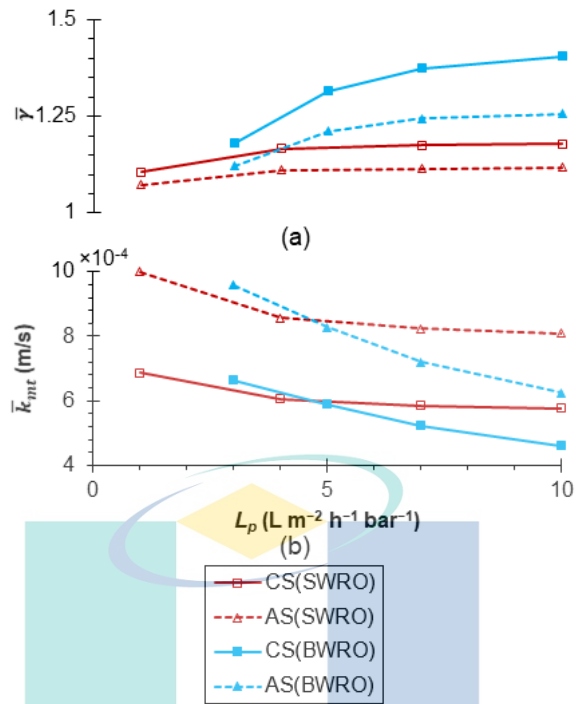
Figure 6.3   Effect of intrinsic membrane permeance on (a) area-averaged concentration polarisation ($\bar{\gamma}$) and (b) mass transfer coefficient ($\bar{k}_{mt}$) at the same inlet TMP ($\Delta p_{tm,in,\,SW} = 6.5$ MPa and $\Delta p_{tm,in,\,BW} = 1.5$ MPa)
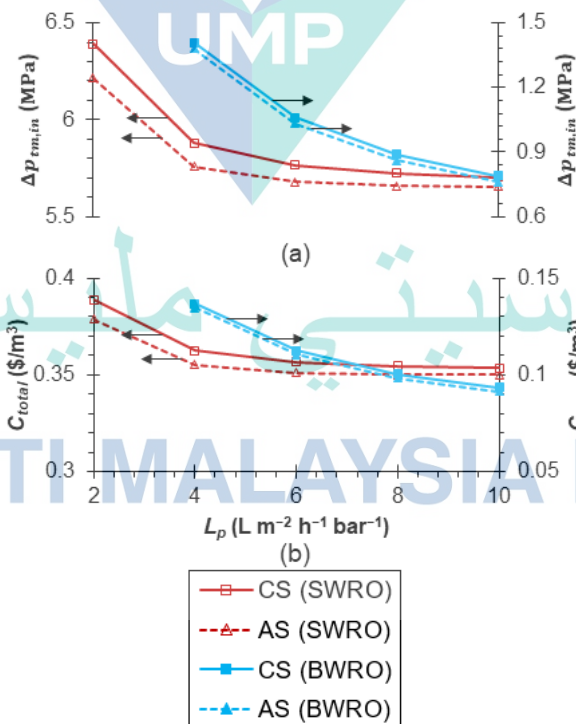
Figure 6.4   Effect of intrinsic membrane permeance on (a) inlet transmembrane pressure ($\Delta p_{tm,in}$) and (b) total processing cost (C_{total}) at fixed R_r of 50% for SWRO and 70% for BWRO

Figure 6.4 shows the effect of membrane permeance on the corresponding total processing cost (C_{total}) when the membrane is operated at a fixed membrane length and recovery rate (50% for SWRO, and 70% for BWRO). As expected, the total processing cost decreases when permeance increases. This is because, at the same recovery, a higher membrane permeance requires a lower inlet pressure and hence lower energy cost (Figure 6.4a). However, the rate of decrease in cost decreases as the permeance increases (Figure 6.4b), and this is more evident for SWRO than for BWRO. As a consequence, the cost obtained when using the highest permeance membrane with a conventional spacer can be achieved at a lower permeance using an advanced spacer. This is particularly evident for SWRO, for which the total processing cost using the advanced spacer with a membrane permeance of 5 L m^{-2} h^{-1} bar^{-1} would require an almost doubling of the permeance (to about 10 L m^{-2} h^{-1} bar^{-1}) if using a conventional spacer. For BWRO, on the other hand, the advanced spacer shows less of an impact because relatively larger cost reductions are still possible by increasing membrane permeance. Nevertheless, the relevance of increasing membrane permeance (i.e., above 3 L m^{-2} h^{-1} bar^{-1}) is likely to remain in the near future, given that the current TFC RO membranes operate within the range of 1–3 L m^{-2} h^{-1} bar^{-1} (Chong et al., 2018; Chowdhury et al., 2018; Elimelech & Phillip, 2011). Hence, there are still some prospects to reduce C_{total} by increasing membrane permeance, especially for BWRO. For SWRO, however, improving spacer performance is more likely to yield cost reductions than membrane permeance increases beyond 6 L m^{-2} h^{-1} bar^{-1}.

To ascertain whether the reported trends depend on the economic assumptions employed in this work, the sensitivity of the equivalent permeance ($L_{p,eq}$) to amortization factor, energy and membrane cost is analysed. The equivalent permeance is defined as the membrane permeance that, when using the advanced spacer, yields the same total cost as the highest permeance tested for the conventional spacer (10 L m^{-2} h^{-1} bar^{-1}). Figure 6.5 shows that change in equivalent L_p is barely sensitive to the change in energy cost, and practically does not change despite large changes in amortization factor or membrane cost. Therefore, it is clear that the cost benefits of coupling advanced spacers to high-permeance membranes are independent of the economic assumptions.
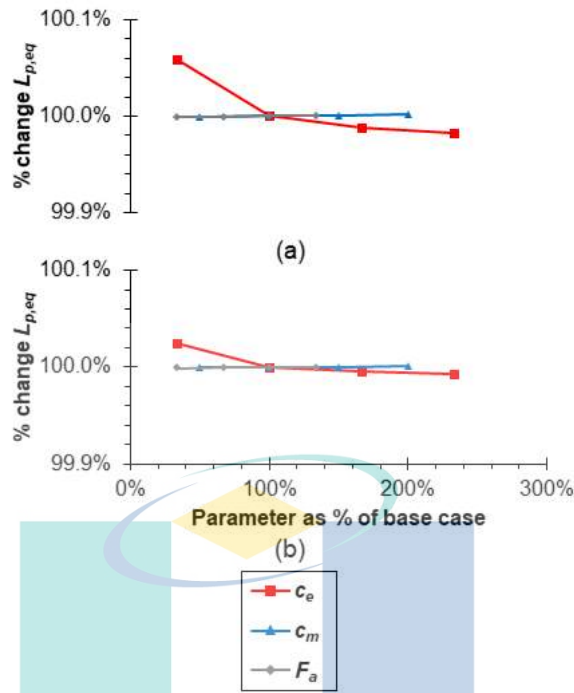
Figure 6.5   Sensitivity analysis of the effect of amortization factor (F_a), energy (c_e) and membrane costs (c_m) on the percentage change in equivalent L_p when using the advanced spacer for (a) SWRO and (b) BWRO

6.2   Effect of Inlet Transmembrane Pressure ($\Delta p_{tm,in}$)

In general, C_{total} tends to increase with increasing $\Delta p_{tm,in}$ because of a larger driving force that requires higher energy consumption. However, this is not the trend for low-permeance BWRO (Figure 6.6), where it can be seen that C_{total} decreases by 5% despite a 33% increase in the $\Delta p_{tm,in}$ when using a conventional spacer. This can be explained by the cost breakdown presented in Figure 6.7, where it is shown that the operating pressure unit cost (C_{op}) remains almost constant despite increases in $\Delta p_{tm,in}$. This is because the rate of recovery increases faster than the cost due to the driving force, as $\Delta p_{tm,in}$ increases. Thus, C_{total} for low-permeance BWRO is mostly driven by the pre-treatment cost (C_{pt}), whereas a larger recovery increases the basis for the unit cost, thus decreasing C_{pt} and the overall total cost. It is worth noting that the decreasing trend in C_{total} is not applicable for low-permeance SWRO because the driving force required for SWRO is significantly larger than for BWRO (at least 4 times higher). Thus, C_{op} for SWRO is driven by the $\Delta p_{tm,in}$ rather than by the recovery rate.

73
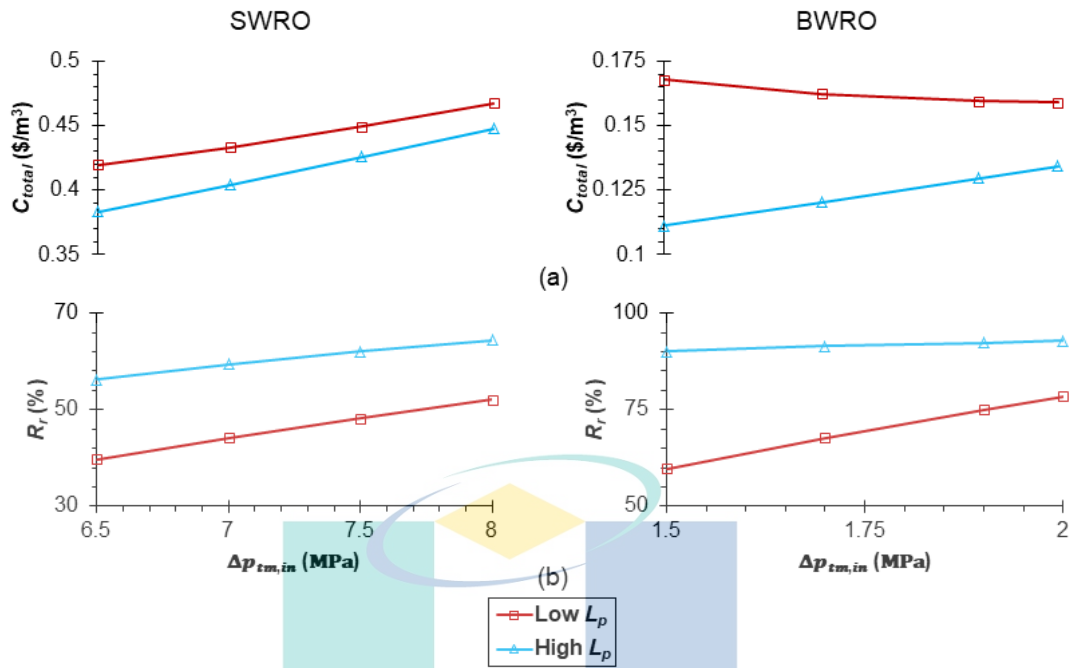
Figure 6.6   Effect of $\Delta p_{tm,in}$ on (a) total processing cost (C_{total}) and (b) recovery rate (R_r) using conventional spacer for low ($L_{p,SW} = 1$ L m^{-2} h^{-1} bar^{-1} and $L_{p,BW} = 3$ L m^{-2} h^{-1} bar^{-1}) and high intrinsic membrane permeance ($L_{p,SW} = L_{p,BW} = 10$ L m^{-2} h^{-1} bar^{-1}), respectively
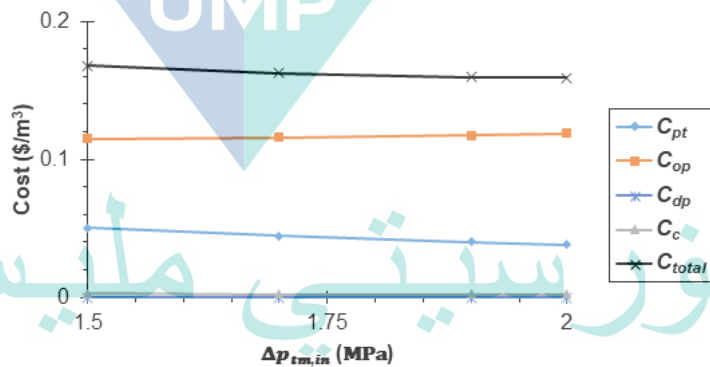
Figure 6.7 Cost breakdown for low-permeance BWRO (using conventional spacer) as a function of $\Delta p_{tm,in}$.

6.3   Effect of Feed Conditions

This section investigates the feed flow conditions, i.e., feed concentration and velocity, on the total processing cost and recovery rate using a conventional spacer. As expected (see Figure 6.8), an increase in feed concentration results in an increase of solute concentration near the membrane wall which in turn reduces flux and recovery rate,

leading to an increase in C_{total} regardless of the value of membrane permeance at the same cross-flow velocity and driving force.
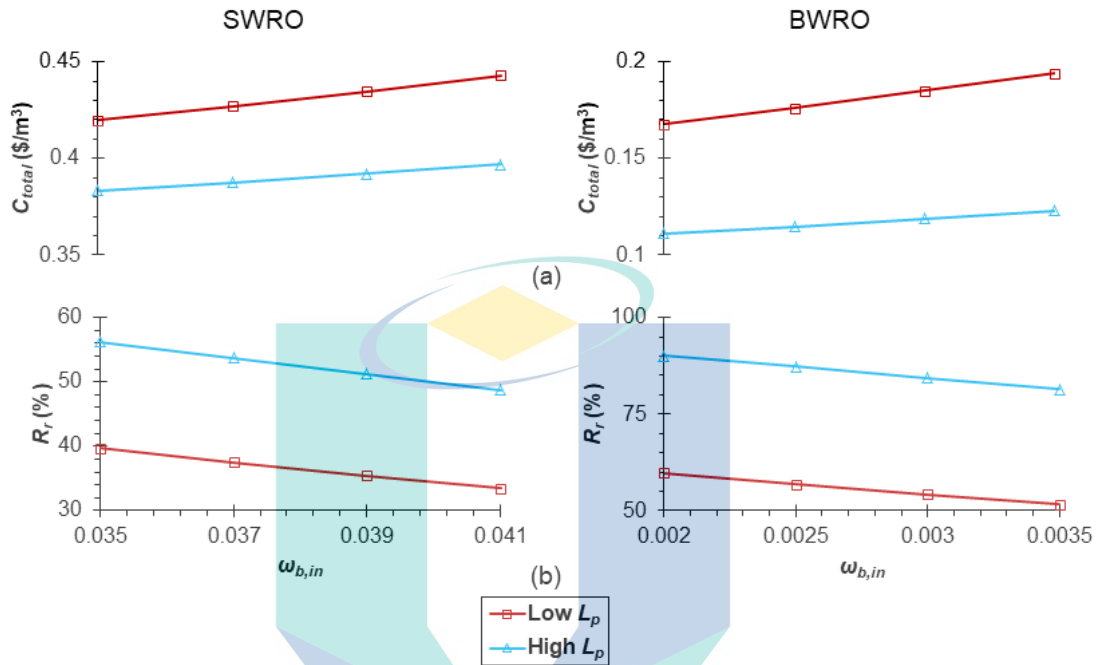
Figure 6.8 Effect of feed concentration ($w_{b,in}$) on (a) total processing cost (C_{total}) and (b) recovery rate (R_r) using conventional spacer for low ($L_{p,SW} = 1$ L m^{-2} h^{-1} bar^{-1} and $L_{p,BW} = 3$ L m^{-2} h^{-1} bar^{-1}) and high intrinsic membrane permeance low ($L_{p,SW} = L_{p,BW} = 10$ L m^{-2} h^{-1} bar^{-1}), respectively.

On the other hand, Figure 6.9 presents the impact of inlet velocity on C_{total} and R_r for both the low and high-permeance membranes. It is interesting to note that C_{total} and R_r for high-permeance SWRO and BWRO remains basically unchanged within the range of feed velocity values typically encountered in RO operations. This is because, for a high-permeance membrane, the mass transfer coefficient ($k_{mt,per}$) and productivity of downstream module regions that were previously ineffective due to low flow rate and k_{mt} can be increased at a larger feed flow rate, as evidenced from Figure 6.10. These results also show that the membrane flux approaches zero faster for the lower inlet velocity (i.e. 0.07 m/s, approaching zero flux at around 2 m from the inlet) than for the larger inlet velocity (i.e., 0.135 m/s, with near-zero flux after 3 m) for both high-permeance BWRO and SWRO.
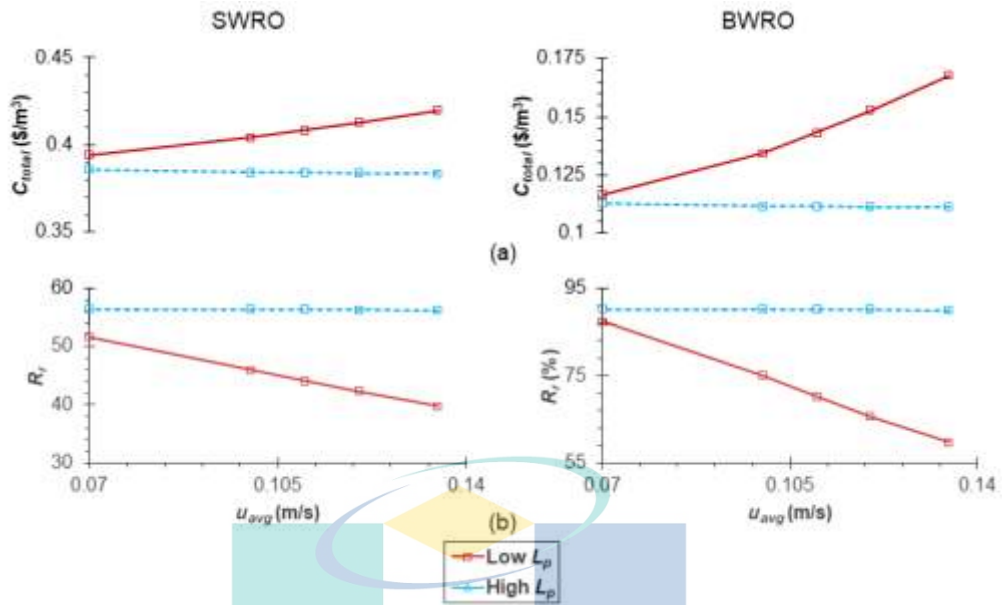
Figure 6.9 Effect of inlet velocity (u_{avg}) on (a) total processing cost (C_{total}) and (b) recovery rate (R_r) using conventional spacer for low ($L_{p,\text{SW}} = 1$ L m^{-2} h^{-1} bar^{-1} and $L_{p,\text{BW}} = 3$ L m^{-2} h^{-1} bar^{-1}) and high intrinsic membrane permeance ($L_{p,\text{SW}} = L_{p,\text{BW}} = 10$ L m^{-2} h^{-1} bar^{-1}), respectively.
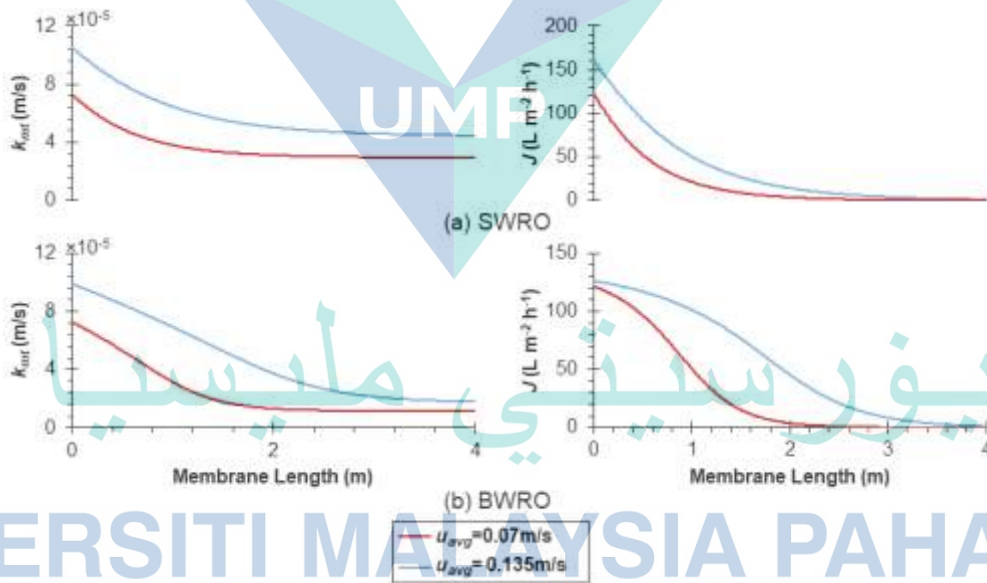
Figure 6.10 Effect of inlet velocity (u_{avg}) on mass transfer coefficient ($k_{mt,per}$) for (a) SWRO and (b) BWRO under high intrinsic membrane permeance ($L_{p,\text{SW}} = L_{p,\text{BW}} = 10$ L m^{-2} h^{-1} bar^{-1})

6.4 Conclusion

The results of this techno-economic study show that, when operating at constant feed pressure, an advanced spacer that doubles mass transfer and reduces energy losses in a SWM module can only enhance flux more than the conventional spacer within the region close to the module inlet. This is because of the fast decrease in Reynolds number associated with a larger flux, which in turn results in a reduction in mass transfer downstream. Likewise, a high-permeance membrane also increases flux more toward the module inlet, which reduces the performance of the latter part of the module. This suggests that lower length modules in a tapered-array configuration might be the best configuration used for high-permeance membrane.

This paper also found that when the membrane permeance is increased, the total processing cost can be reduced more for BWRO than for SWRO. Nevertheless, the effects are limited with further reductions in total processing cost when the membrane permeance exceeds 4 L m^{-2} h^{-1} bar^{-1} for SWRO and 7 L m^{-2} h^{-1} bar^{-1} for BWRO, owing to the high CP and lower mass transfer coefficient. This trend is similar to the SEC data reported in the literature (Cohen-Tanugi et al., 2014; Shrivastava et al., 2015) in which energy savings are negligible when L_p exceeds 4 and 5 L m^{-2} h^{-1} bar^{-1} for seawater and brackish water, respectively. Moreover, and despite not being included in the calculations presented in this paper, the tendency for fouling to occur (particularly scaling) is larger for high-permeance membranes, which could further reduce permeate flux and increase total processing costs if long modules are used.

When operating at constant recovery, it was shown that a higher membrane permeance requires less pumping energy. However, there are diminishing returns in terms of cost reductions as the permeance increases. This means that an advanced spacer can achieve significant cost reductions at much lower permeance values than the conventional spacer, particularly for SWRO. For example, achieving the same total cost as the advanced spacer at a permeance of 5 L m^{-2} h^{-1} bar^{-1} required a near doubling of permeance if the conventional spacer was used. The use of an advanced spacer for BWRO, on the other hand, shows less potential because cost reductions are still possible as membrane permeance is increased. A sensitivity analysis revealed that the equivalent permeance ($L_{p,eq}$) is barely sensitive to the change in energy cost, and does not vary with

changes in the amortization factor or membrane cost. Thus, the trends observed were practically independent of the economic assumptions made.

For low-permeance BWRO, the results reveal that the operating pressure unit cost is similar for any $\Delta p_{tm,in}$. This is because the associated $\Delta p_{tm,in}$ for BWRO is smaller compared to SWRO. Thus, the recovery rate increases at a faster rate than for an increase in cost due to a higher driving force. With respect to feed conditions, the results show that the total processing cost is similar for any feed velocity typically encountered for RO operations when using a high-permeance membrane. This is because, for a high-permeance membrane, the mass transfer coefficient or enhancement at a latter part of the module regions that were previously found ineffective due to low flow rate and k_{mt} can be enhanced at a larger feed velocity.

The main finding from this study is that when operating at constant recovery, improved spacer designs are more likely to yield cost reductions for SWRO than further increases in membrane permeance. These types of insights are gained through the use of the simplified techno-economic analysis method presented in this paper, which can be used to predict trends or relative changes in the magnitude of the total processing cost as the different operating and economic parameters are varied.

CHAPTER 7

CONCLUSION

This thesis systematically investigates effect of feed spacer on RO membrane performance through computational fluid dynamics (CFD) and techno-economic modelling. The CFD study analyses the effect of different perforation aspects of spacers on the membrane performance and investigates the mechanisms that result in shear stress and mass transfer enhancement for spacer with different degrees of "floating" characteristics. This thesis also investigates the techno-economic case for coupling advanced spacers to high-permeance seawater RO (SWRO) and brackish water RO (BWRO).

7.1   Conclusion

The conclusion of the studies in this thesis are as below:

i.   The study on perforated spacer shows that spacers with perforations near the membrane surface demonstrate similar mass transfer and pressure loss to the case where the perforation is in the middle of the channel (i.e., bulk flow) and the case that considers spacers without perforation, for a Re_h range of $50 – 200$. Moreover, a large perforation size decreases mass transfer by over 10% through weakening of the flow velocity or suppression of vortex shedding. The main finding is that spacer perforation does not improve mass transfer for the cases simulated using conventional spacers.

ii. The study on spacer with "floating" characteristics reveals that the floating ratio (R_f) is not a determining factor for mass transfer enhancement, as the transport mechanism is more strongly dependent on other geometric characteristics, such as a 2- or 3-layer design. The λ_2 analysis confirms our hypothesis, as the middle filament in a 3-layer design disrupts the formation of the large streamwise vortex located downstream of the intersection between the top and bottom filaments at

Re_h 200. This explains why 3-layer spacers (both woven and non-woven) show lower Sherwood number (Sh) than a 2-layer woven (2LW) spacer at Re_h 200. However, at a smaller Re_h (<100), the vortical flow for 2LW is rather weak as a result of reduced membrane region with fluid mixing caused by creeping flow. This has led to the smaller Sh of 2LW compared to the 3-layer spacer.

iii.   In the study of techno-economic case, it is found that for high-permeance membranes, advanced spacers are more effective than conventional spacers in improving flux in the region close to the inlet, due to a fast decrease in Reynolds number along the channel. The total cost for seawater RO (SWRO) and brackish water RO (BWRO) could be reduced by 7.5% and 32%, respectively by increasing the membrane permeance to 10 L/m^2.h.bar regardless of the spacer type used. However, as feed velocity has negligible effects on total cost for high-permeance membrane systems, further cost reductions with larger membrane permeances are limited due to significant concentration polarisation and lower mass transfer. Nevertheless, when operating SWRO at constant recovery, those levels of cost reduction can be achieved with an advanced spacer at half of that membrane permeance value. This highlights that more cost-effectiveness can be gained by improving the spacer efficacy than by increasing membrane permeance.

7.2   Recommendations

The recommendation for future works includes:

i.   The study on perforated spacer is restricted to only one single spacer geometry (i.e., conventional spacer). Thus, the effect of perforation using other spacer geometry designs remains unclear. Future work should be conducted to further address this topic.

ii.   It is worth noting that only simple cylindrical spacer filaments are considered in the present work. It may be possible that wall shear and mass transfer could be increased through the modification of the spacer filament profile. As the impact of spacer filament profile is not yet well understood, future investigation on this subject is thus needed.

iii.   The techno-economic methodology is restricted to steady-flow analysis, without any time-dependent fouling effects. Nevertheless, the question on the effect of fouling on the flux and cost-effectiveness of SWM RO modules when membrane permeance or mass transfer is increased remains important, and future work is still required to address these issues.
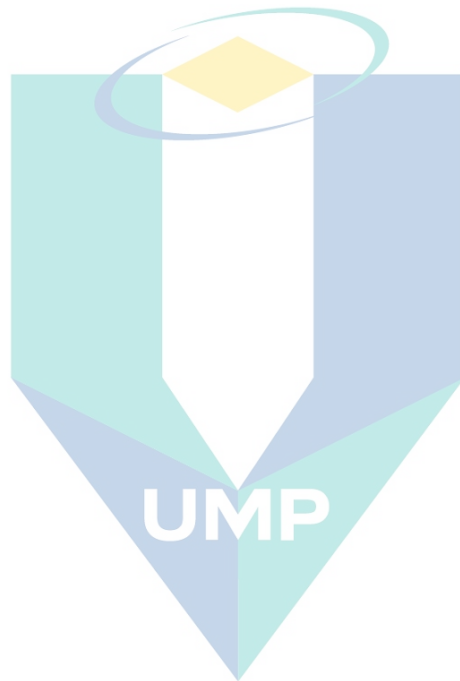
REFERENCES

Abid, H. S., Johnson, D. J., Hashaikeh, R., & Hilal, N. (2017). A review of efforts to reduce membrane fouling by control of feed spacer characteristics. *Desalination, 420*, 384-402. doi:https://doi.org/10.1016/j.desal.2017.07.019

Achilli, A., Cath, T. Y., & Childress, A. E. (2009). Power generation with pressure retarded osmosis: An experimental and theoretical investigation. *Journal of Membrane Science, 343*(1), 42-52. doi:https://doi.org/10.1016/j.memsci.2009.07.006

Al-Anzi, B., Thomas, A., & Fernandes, J. (2016). Lab scale assessment of power generation using pressure retarded osmosis from wastewater treatment plants in the state of Kuwait. *Desalination, 396*, 57-69. doi:https://doi.org/10.1016/j.desal.2016.06.005

Al-Obaidi, M. A., Filippini, G., Manenti, F., & Mujtaba, I. M. (2019). Cost evaluation and optimisation of hybrid multi effect distillation and reverse osmosis system for seawater desalination. *Desalination, 456*, 136-149. doi:https://doi.org/10.1016/j.desal.2019.01.019

Al-Shemmeri, T. T. (1988). Fundamentals of fluid mechanics: by Philip M. Gerhart and Richard J. Gross, Addison Wesley, 1985. ISBN 0-201-11410-0, 856 pages, illustrated, hard-back, £39.95. *Journal of Mechanical Working Technology, 16*(2), 227-228. doi:https://doi.org/10.1016/0378-3804(88)90174-X

Alexiadis, A., Wiley, D. E., Fletcher, D. F., & Bao, J. (2007). Laminar Flow Transitions in a 2D Channel with Circular Spacers. *Industrial & Engineering Chemistry Research, 46*(16), 5387-5396. doi:10.1021/ie0607797

Ali, S. M., Qamar, A., Kerdi, S., Phuntsho, S., Vrouwenvelder, J. S., Ghaffour, N., & Shon, H. K. (2019). Energy efficient 3D printed column type feed spacer for membrane filtration. *Water Research, 164*, 114961. doi:https://doi.org/10.1016/j.watres.2019.114961

Alsarayreh, A. A., Al-Obaidi, M. A., Al-Hroub, A. M., Patel, R., & Mujtaba, I. M. (2020). Evaluation and minimisation of energy consumption in a medium-scale reverse osmosis brackish water desalination plant. *Journal of Cleaner Production, 248*, 119220. doi:https://doi.org/10.1016/j.jclepro.2019.119220

Amokrane, M., Sadaoui, D., Dudeck, M., & Koutsou, C. (2015). New spacer designs for the performance improvement of the zigzag spacer configuration in spiral-wound membrane modules. *Desalination and Water Treatment*. doi:10.1080/19443994.2015.1022003

Anis, S. F., Hashaikeh, R., & Hilal, N. (2019). Reverse osmosis pretreatment technologies and future trends: A comprehensive review. *Desalination, 452*, 159-195. doi:https://doi.org/10.1016/j.desal.2018.11.006

Avlonitis, S. A., Pappas, M., & Moutesidis, K. (2007). A unified model for the detailed investigation of membrane modules and RO plants performance. *Desalination, 203*(1), 218-228. doi:https://doi.org/10.1016/j.desal.2006.04.009

Baker, R. W. (2004). *Membrane Technology and Applications*: John Wiley & Sons, Ltd.

Balogun, H. A., Sulaiman, R., Marzouk, S. S., Giwa, A., & Hasan, S. W. (2019). 3D printing and surface imprinting technologies for water treatment: A review. *Journal of Water Process Engineering, 31*, 100786. doi:https://doi.org/10.1016/j.jwpe.2019.100786

Balster, J., Punt, I., Stamatialis, D. F., & Wessling, M. (2006). Multi-layer spacer geometries with improved mass transport. *Journal of Membrane Science, 282*, 351-361.

Bartman, A. R., Zhu, A., Christofides, P. D., & Cohen, Y. (2010). Minimizing energy consumption in reverse osmosis membrane desalination using optimization-based control. *Journal of Process Control, 20*(10), 1261-1269. doi:https://doi.org/10.1016/j.jprocont.2010.09.004

Bucs, S. S., Farhat, N., Kruithof, J. C., Picioreanu, C., van Loosdrecht, M. C. M., & Vrouwenvelder, J. S. (2018). Review on strategies for biofouling mitigation in spiral wound membrane systems. *Desalination, 434*, 189-197. doi:https://doi.org/10.1016/j.desal.2018.01.023

Bucs, S. S., Valladares Linares, R., Marston, J. O., Radu, A. I., Vrouwenvelder, J. S., & Picioreanu, C. (2015). Experimental and numerical characterization of the water flow in spacer-filled channels of spiral-wound membranes. *Water Research, 87*, 299-310. doi:https://doi.org/10.1016/j.watres.2015.09.036

Castillo, E. H. C., Thomas, N., Al-Ketan, O., Rowshan, R., Abu Al-Rub, R. K., Nghiem, L. D., . . . Naidu, G. (2019). 3D printed spacers for organic fouling mitigation in membrane distillation. *Journal of Membrane Science, 581*, 331-343. doi:10.1016/j.memsci.2019.03.040

Cath, T. Y., Childress, A. E., & Elimelech, M. (2006). Forward osmosis: Principles, applications, and recent developments. *Journal of Membrane Science, 281*(1), 70-87. doi:https://doi.org/10.1016/j.memsci.2006.05.048

Choi, W., Lee, C., Yoo, C. H., Shin, M. G., Lee, G. W., Kim, T.-S., . . . Lee, J.-H. (2020). Structural tailoring of sharkskin-mimetic patterned reverse osmosis membranes for optimizing biofouling resistance. *Journal of Membrane Science, 595*, 117602. doi:https://doi.org/10.1016/j.memsci.2019.117602

Chong, C. Y., Lau, W. J., Yusof, N., Lai, G. S., Othman, N. H., Matsuura, T., & Ismail, A. F. (2018). Studies on the properties of RO membranes for salt and boron removal: Influence of thermal treatment methods and rinsing treatments. *Desalination, 428*, 218-226. doi:https://doi.org/10.1016/j.desal.2017.11.009

Chowdhury, M., Steffes, J., Huey, B., & McCutcheon, J. (2018). 3D printed polyamide membranes for desalination. *Science (New York, N.Y.), 361*, 682-686. doi:10.1126/science.aar2122

Cohen-Tanugi, D., McGovern, R., Dave, S., Lienhard, J., & Grossman, J. (2014). Quantifying the potential of ultra-permeable membranes for water desalination. *Energy & Environmental Science, 7*, 1134-1141. doi:10.1039/C3EE43221A

Day, M. A. (1990). The no-slip condition of fluid dynamics. *Erkenntnis, 33*(3), 285-296. doi:10.1007/BF00717588

DOW. (2018). DOW FILMTEC^{TM} SW30-8040 Seawater Reverse Osmosis Element. In T. D. C. Company (Ed.), *Product information* (Vol. 609-00616-0808).

Elazhar, F., Touir, J., Elazhar, M., Belhamidi, S., El Harrak, N., Zdeg, A., . . . Elmidaoui, A. (2015). Techno-economic comparison of reverse osmosis and nanofiltration in desalination of a Moroccan brackish groundwater. *Desalination and Water Treatment, 55*(9), 2471-2477. doi:10.1080/19443994.2014.959739

Elimelech, M., & Phillip, W. (2011). The Future of Seawater Desalination: Energy, Technology, and the Environment. *Science (New York, N.Y.), 333*, 712-717. doi:10.1126/science.1200488

Fane, A. G. (2018). A grand challenge for membrane desalination: More water, less carbon. *Desalination, 426*, 155-163. doi:https://doi.org/10.1016/j.desal.2017.11.002

Filippini, G., Al-Obaidi, M. A., Manenti, F., & Mujtaba, I. M. (2019). Design and economic evaluation of solar-powered hybrid multi effect and reverse osmosis system for seawater desalination. *Desalination, 465*, 114-125. doi:https://doi.org/10.1016/j.desal.2019.04.016

Fimbres-Weihs, G. A., & Wiley, D. E. (2007). Numerical study of mass transfer in three-dimensional spacer-filled narrow channels with steady flow. *Journal of Membrane Science, 306*(1–2), 228-243. doi:10.1016/j.memsci.2007.08.043

Fimbres Weihs, G. A., & Wiley, D. E. (2007). Numerical study of mass transfer in three-dimensional spacer-filled narrow channels with steady flow. *Journal of Membrane Science, 306*, 228-243.

Fimbres Weihs, G. A., & Wiley, D. E. (2008). Numerical study of two-dimensional multi-layer spacer designs for minimum drag and maximum mass transfer. *Journal of Membrane Science, 325*, 809-822.

Fimbres Weihs, G. A., & Wiley, D. E. (2010). Review of 3D CFD modeling of flow and mass transfer in narrow spacer-filled channels in membrane modules. *Chemical Engineering and Processing: Process Intensification, 49*, 759-781.

Fimbres Weihs, G. A., Wiley, D. E., & Fletcher, D. F. (2006). Unsteady Flows with Mass Transfer in Narrow Zigzag Spacer-Filled Channels: A Numerical Study. *Industrial & Engineering Chemistry Research, 45*(19), 6594-6603. doi:10.1021/ie060243l

Fletcher, D. F., & Wiley, D. E. (2004). A computational fluids dynamics study of buoyancy effects in reverse osmosis. *Journal of Membrane Science, 245*, 175-181.

Foo, K., Liang, Y. Y., & Fimbres Weihs, G. A. (2020). CFD study of the effect of SWM feed spacer geometry on mass transfer enhancement driven by forced transient slip velocity. *Journal of Membrane Science, 597*, 117643. doi:https://doi.org/10.1016/j.memsci.2019.117643

Gastelum Reyes, M., & Fimbres Weihs, G. A. (2016). *CFD study of optimal frequency pulsatile flow for mass transfer enhancement in spacer-filled Ro membrane channels*. Paper presented at the Memorias del Congreso de la Sociedad Mexicana de Ciencia y Tecnología de Membranas.

Geraldes, V., & Afonso, M. D. (2006). Generalized Mass-Transfer Correction Factor for Nanofiltration and Reverse Osmosis. *AIChE Journal, 52*, 3353-3362.

Ghernaout, D., Naceur, W., Aichouni, M., Aït-Messaoudène, N., & Alghamdi, A. (2018). On the Validation Perspectives of the Proposed Novel Dimensionless Fouling Index. *International Journal of ADVANCED AND APPLIED SCIENCES, 5*, 116-122. doi:10.21833/ijaas.2018.07.014

Gill, W. N., Wiley, D. E., Fell, C. J. D., & Fane, A. G. (1988). Effect of Viscosity on Concentration Polarization in Ultrafiltration. *AIChE Journal, 34*(9), 1563-1567.

Glater, J. (1998). The early history of reverse osmosis membrane development. *Desalination, 117*(1), 297-309. doi:https://doi.org/10.1016/S0011-9164(98)00122-2

Goh, P. S., Lau, W. J., Othman, M. H. D., & Ismail, A. F. (2018). Membrane fouling in desalination and its mitigation strategies. *Desalination, 425*, 130-155. doi:https://doi.org/10.1016/j.desal.2017.10.018

Greenlee, L. F., Lawler, D. F., Freeman, B. D., Marrot, B., & Moulin, P. (2009). Reverse osmosis desalination: Water sources, technology, and today's challenges. *Water Research, 43*, 2317-2348.

Gu, B., Adjiman, C. S., & Xu, X. Y. (2017). The effect of feed spacer geometry on membrane performance and concentration polarisation based on 3D CFD simulations. *Journal of Membrane Science, 527*, 78-91. doi:https://doi.org/10.1016/j.memsci.2016.12.058

Gu, B., Xu, X. Y., & Adjiman, C. S. (2017). A predictive model for spiral wound reverse osmosis membrane modules: The effect of winding geometry and accurate geometric details. *Computers & Chemical Engineering, 96*, 248-265. doi:https://doi.org/10.1016/j.compchemeng.2016.07.029

Guillen, G., & Hoek, E. M. V. (2009). Modeling the impacts of feed spacer geometry on reverse osmosis and nanofiltration processes. *Chemical Engineering Journal, 149*, 221-231.

Guo, Y., Al-Jubainawi, A., & Ma, Z. (2019). Mathematical modelling and simulation analysis of electrodialysis regeneration for LiCl liquid desiccant air conditioning systems. *International Journal of Refrigeration, 107*, 234-245. doi:https://doi.org/10.1016/j.ijrefrig.2019.08.006

Haaksman, V. A., Siddiqui, A., Schellenberg, C., Kidwell, J., Vrouwenvelder, J. S., & Picioreanu, C. (2017). Characterization of feed channel spacer performance using geometries obtained by X-ray computed tomography. *Journal of Membrane Science, 522*, 124-139. doi:https://doi.org/10.1016/j.memsci.2016.09.005

Haddadi, B., Jordan, C., Miltner, M., & Harasek, M. (2018). Membrane modeling using CFD: Combined evaluation of mass transfer and geometrical influences in 1D and 3D. *Journal of Membrane Science, 563*, 199-209. doi:https://doi.org/10.1016/j.memsci.2018.05.040

Haidari, A. H., Heijman, S. G. J., Uijttewaal, W. S. J., & van der Meer, W. G. J. (2019). Determining effects of spacer orientations on channel hydraulic conditions using PIV. *Journal of Water Process Engineering, 31*, 100820. doi:https://doi.org/10.1016/j.jwpe.2019.100820

Haidari, A. H., Heijman, S. G. J., & van der Meer, W. G. J. (2016). Visualization of hydraulic conditions inside the feed channel of Reverse Osmosis: A practical comparison of velocity between empty and spacer-filled channel. *Water Research, 106*, 232-241. doi:https://doi.org/10.1016/j.watres.2016.10.012

Haidari, A. H., Heijman, S. G. J., & van der Meer, W. G. J. (2018a). Effect of spacer configuration on hydraulic conditions using PIV. *Separation and Purification Technology, 199*, 9-19. doi:https://doi.org/10.1016/j.seppur.2018.01.022

Haidari, A. H., Heijman, S. G. J., & van der Meer, W. G. J. (2018b). Optimal design of spacers in reverse osmosis. *Separation and Purification Technology, 192*, 441-456. doi:https://doi.org/10.1016/j.seppur.2017.10.042

Han, Z., Terashima, M., Liu, B., & Yasui, H. (2018). CFD Investigation of the Effect of the Feed Spacer on Hydrodynamics in Spiral Wound Membrane Modules. *Mathematical and Computational Applications, 23*(4), 17. doi:10.3390/mca23040080

Holland, F. A., & Bragg, R. (1995). 3 - Flow of incompressible non-Newtonian fluids in pipes. In F. A. Holland & R. Bragg (Eds.), *Fluid Flow for Chemical Engineers (Second Edition)* (pp. 96-139). Oxford: Butterworth-Heinemann.

Horstmeyer, N., Lippert, T., Schön, D., Schlederer, F., Picioreanu, C., Achterhold, K., . . . Drewes, J. E. (2018). CT scanning of membrane feed spacers – Impact of spacer model accuracy on hydrodynamic and solute transport modeling in membrane feed channels. *Journal of Membrane Science, 564*, 133-145. doi:10.1016/j.memsci.2018.07.006

Hu, M., & Mi, B. (2013). Enabling Graphene Oxide Nanosheets as Water Separation Membranes. *Environmental Science & Technology, 47*. doi:10.1021/es400571g

Hui, Y., Xing, Y., Rong, W., & Fane, A. G. (2011). Numerical simulation of heat and mass transfer in direct membrane distillation in a hollow fiber module with laminar flow. *Journal of Membrane Science, 384*, 107-116.

Im, S. J., Jeong, G., Jeong, S., Cho, J., & Jang, A. (2020). Fouling and transport of organic matter in cellulose triacetate forward-osmosis membrane for wastewater reuse and seawater desalination. *Chemical Engineering Journal, 384*. doi:10.1016/j.cej.2019.123341

Im, S. J., Jeong, S., Jeong, S., & Jang, A. (2020). Techno-economic evaluation of an element-scale forward osmosis-reverse osmosis hybrid process for seawater desalination. *Desalination, 476*, 114240. doi:https://doi.org/10.1016/j.desal.2019.114240

Ismail, A. F., Khulbe, K. C., & Matsuura, T. (2019). Chapter 5 - RO Membrane Module. In A. F. Ismail, K. C. Khulbe, & T. Matsuura (Eds.), *Reverse Osmosis* (pp. 117-141): Elsevier.

Jeong, K., Park, M., Oh, S., & Kim, J. H. (2020). Impacts of flow channel geometry, hydrodynamic and membrane properties on osmotic backwash of RO membranes—CFD modeling and simulation. *Desalination, 476*, 114229. doi:https://doi.org/10.1016/j.desal.2019.114229

Karabelas, A. J., Kostoglou, M., & Koutsou, C. P. (2015). Modeling of spiral wound membrane desalination modules and plants – review and research priorities. *Desalination, 356*, 165-186. doi:https://doi.org/10.1016/j.desal.2014.10.002

Karabelas, A. J., Koutsou, C. P., Kostoglou, M., & Sioutopoulos, D. C. (2018). Analysis of specific energy consumption in reverse osmosis desalination processes. *Desalination, 431*, 15-21. doi:https://doi.org/10.1016/j.desal.2017.04.006

Kavianipour, O., Ingram, G. D., & Vuthaluru, H. B. (2017). Investigation into the effectiveness of feed spacer configurations for reverse osmosis membrane modules using Computational Fluid Dynamics. *Journal of Membrane Science, 526*, 156-171. doi:https://doi.org/10.1016/j.memsci.2016.12.034

Kavianipour, O., Ingram, G. D., & Vuthaluru, H. B. (2019). Studies into the mass transfer and energy consumption of commercial feed spacers for RO membrane modules using CFD: Effectiveness of performance measures. *Chemical Engineering Research and Design, 141*, 328-338. doi:https://doi.org/10.1016/j.cherd.2018.10.041

Kedem, O., & Katchalsky, A. (1958). Thermodynamic analysis of the permeability of biological membranes to non-electrolytes. *Biochimica et Biophysica Acta, 27*, 229-246.

Kerdi, S., Qamar, A., Vrouwenvelder, J. S., & Ghaffour, N. (2018). Fouling resilient perforated feed spacers for membrane filtration. *Water Research, 140*, 211-219. doi:https://doi.org/10.1016/j.watres.2018.04.049

Kim, D. I., Kim, J., Shon, H. K., & Hong, S. (2015). Pressure retarded osmosis (PRO) for integrating seawater desalination and wastewater reclamation: Energy consumption and fouling. *Journal of Membrane Science, 483*, 34-41. doi:https://doi.org/10.1016/j.memsci.2015.02.025

Kim, J. E., Phuntsho, S., Chekli, L., Choi, J. Y., & Shon, H. K. (2018). Environmental and economic assessment of hybrid FO-RO/NF system with selected inorganic draw solutes for the treatment of mine impaired water. *Desalination, 429*, 96-104. doi:https://doi.org/10.1016/j.desal.2017.12.016

Kook, S., Lee, C., Nguyen, T. T., Lee, J., Shon, H. K., & Kim, I. S. (2018). Serially connected forward osmosis membrane elements of pressure-assisted forward osmosis-reverse osmosis hybrid system: Process performance and economic analysis. *Desalination, 448*, 1-12. doi:https://doi.org/10.1016/j.desal.2018.09.019

Koutsou, C. P., & Karabelas, A. J. (2015). A novel retentate spacer geometry for improved spiral wound membrane (SWM) module performance. *Journal of Membrane Science, 488*, 129-142. doi:https://doi.org/10.1016/j.memsci.2015.03.064

Koutsou, C. P., Karabelas, A. J., & Kostoglou, M. (2018). Fluid dynamics and mass transfer in spacer-filled membrane channels: Effect of uniform channel-gap reduction due to fouling. *Fluids, 3*(1). doi:10.3390/fluids3010012

Koutsou, C. P., Kritikos, E., Karabelas, A. J., & Kostoglou, M. (2020). Analysis of temperature effects on the specific energy consumption in reverse osmosis desalination processes. *Desalination, 476*, 114213. doi:https://doi.org/10.1016/j.desal.2019.114213

Koutsou, C. P., Yiantsios, S. G., & Karabelas, A. J. (2007). Direct numerical simulation of flow in spacer-filled channels: Effect of spacer geometrical characteristics. *Journal of Membrane Science, 291*, 53-69.

Lau, W. J., Goh, P., Ismail, A., & Lai, S.-O. (2014). Ultrafiltration as a pretreatment for seawater desalination: A review. *Membrane Water Treatment, 5*. doi:10.12989/mwt.2014.5.1.015

Lee, J.-Y., Tan, W. S., An, J., Chua, C. K., Tang, C. Y., Fane, A. G., & Chong, T. H. (2016). The potential to enhance membrane module design with 3D printing technology. *Journal of Membrane Science, 499*, 480-490.

Li, F., Meindersma, W., de Haan, A. B., & Reith, T. (2002). Optimization of commercial net spacers in spiral wound membrane modules. *Journal of Membrane Science, 208*, 289-302.

Li, F., Meindersma, W., de Haan, A. B., & Reith, T. (2004). Experimental validation of CFD mass transfer simulations in flat channels with non-woven net spacers. *Journal of Membrane Science, 232*, 19-30.

Li, F., Meindersma, W., de Haan, A. B., & Reith, T. (2005). Novel spacers for mass transfer enhancement in membrane separations. *Journal of Membrane Science, 253*, 1-12.

Li, Y.-L., Tung, K.-L., Chen, Y.-S., & Hwang, K.-J. (2012). CFD analysis of the initial stages of particle deposition in spiral-wound membrane modules. *Desalination, 287*, 200-208.

Liang, Y. Y., Chapman, M. B., Fimbres Weihs, G. A., & Wiley, D. E. (2014). CFD modelling of electro-osmotic permeate flux enhancement on the feed side of a membrane module. *Journal of Membrane Science, 470*, 378-388.

Liang, Y. Y., Fimbres Weihs, G. A., & Fletcher, D. F. (2018). CFD study of the effect of unsteady slip velocity waveform on shear stress in membrane systems. *Chemical Engineering Science, 192*, 16-24. doi:https://doi.org/10.1016/j.ces.2018.07.009

Liang, Y. Y., Fimbres Weihs, G. A., Setiawan, R., & Wiley, D. (2016). CFD modelling of unsteady electro-osmotic permeate flux enhancement in membrane systems. *Chemical Engineering Science, 146*, 189-198. doi:https://doi.org/10.1016/j.ces.2016.02.028

Liang, Y. Y., Fimbres Weihs, G. A., & Wiley, D. E. (2016). CFD modelling of electro-osmotic permeate flux enhancement in spacer-filled membrane channels. *Journal of Membrane Science, 507*, 107-118. doi:https://doi.org/10.1016/j.memsci.2016.02.012

Liang, Y. Y., Fimbres Weihs, G. A., & Wiley, D. E. (2020). Comparison of oscillating flow and slip velocity mass transfer enhancement in spacer-filled membrane channels: CFD analysis and validation. *Journal of Membrane Science, 593*, 117433. doi:https://doi.org/10.1016/j.memsci.2019.117433

Lim, S. Y., Liang, Y. Y., Fimbres Weihs, G. A., Wiley, D. E., & Fletcher, D. F. (2018). A CFD study on the effect of membrane permeance on permeate flux enhancement generated by unsteady slip velocity. *Journal of Membrane Science, 556*, 138-145. doi:https://doi.org/10.1016/j.memsci.2018.03.070

Liu, N., Zhang, Q., Chin, G.-L., Ong, E.-H., Lou, J., Kang, C.-W., . . . Jordan, E. (2010). Experimental investigation of hydrodynamic behavior in a real membrane bio-reactor unit. *Journal of Membrane Science, 353*, 122-134.

Mansouri, N., Moghimi, M., & Taherinejad, M. (2019). Investigation on hydrodynamics and mass transfer in a feed channel of a spiral-wound membrane element using response surface methodology. *Chemical Engineering Research and Design, 149*, 147-157. doi:10.1016/j.cherd.2019.07.006

Manth, T., Gabor, M., & Oklejas, E. (2003). Minimizing RO energy consumption under variable conditions of operation. *Desalination, 157*(1), 9-21. doi:https://doi.org/10.1016/S0011-9164(03)00377-1

Matthiasson, E., & Sivik, B. (1980). Concentration polarization and fouling. *Desalination, 35*, 59-103. doi:https://doi.org/10.1016/S0011-9164(00)88604-X

Mazlan, N. M., Peshev, D., & Livingston, A. G. (2016). Energy consumption for desalination — A comparison of forward osmosis with reverse osmosis, and the potential for perfect membranes. *Desalination, 377*, 138-151. doi:https://doi.org/10.1016/j.desal.2015.08.011

McGovern, R. K., & Lienhard V, J. H. (2016). On the asymptotic flux of ultrapermeable seawater reverse osmosis membranes due to concentration polarisation. *Journal of Membrane Science, 520*, 560-565. doi:https://doi.org/10.1016/j.memsci.2016.07.028

Mi, B. (2014). Graphene Oxide Membranes for Ionic and Molecular Sieving. *Science (New York, N.Y.), 343*, 740-742. doi:10.1126/science.1250247

Mirza, S. (2008). Reduction of energy consumption in process plants using nanofiltration and reverse osmosis. *Desalination, 224*(1), 132-142. doi:https://doi.org/10.1016/j.desal.2007.04.084

Mistry, K., & Lienhard, J. (2012). *Effect of Nonideal Solution Behavior on Desalination of a Sodium Chloride (NaCl) Solution and Comparison to Seawater* (Vol. 135).

Nagy, E. (2019). Chapter 15 - Nanofiltration. In E. Nagy (Ed.), *Basic Equations of Mass Transport Through a Membrane Layer (Second Edition)* (pp. 417-428): Elsevier.

Nanan, K., Thianpong, C., Promvonge, P., & Eiamsa-ard, S. (2014). Investigation of heat transfer enhancement by perforated helical twisted-tapes. *International Communications in Heat and Mass Transfer, 52*, 106-112. doi:https://doi.org/10.1016/j.icheatmasstransfer.2014.01.018

Nuntadusit, C., Wae-hayee, M., Bunyajitradulya, A., & Eiamsa-ard, S. (2012). Thermal visualization on surface with transverse perforated ribs. *International Communications in Heat and Mass Transfer, 39*, 634-639.

Oh, H.-J., Hwang, T.-M., & Lee, S. (2009). A simplified simulation model of RO systems for seawater desalination. *Desalination, 238*(1), 128-139. doi:https://doi.org/10.1016/j.desal.2008.01.043

Okamoto, Y., & Lienhard, J. H. (2019). How RO membrane permeability and other performance factors affect process cost and energy use: A review. *Desalination, 470*, 114064. doi:https://doi.org/10.1016/j.desal.2019.07.004

Ouyang, H., Bao, J., Fimbres Weihs, G. A., & Wiley, D. E. (2013). Control study on mixing enhancement in boundary layers of membrane systems. *Journal of Process Control, 23*(8), 1197-1204. doi:https://doi.org/10.1016/j.jprocont.2013.07.005

Picioreanu, C., Blauert, F., Horn, H., & Wagner, M. (2018). Determination of mechanical properties of biofilms by modelling the deformation measured using optical coherence tomography. *Water Research, 145*, 588-598. doi:https://doi.org/10.1016/j.watres.2018.08.070

Plata, S. L., & Childress, A. E. (2019). Limiting power density in pressure-retarded osmosis: Observation and implications. *Desalination, 467*, 51-56. doi:https://doi.org/10.1016/j.desal.2019.05.013

Qamar, A., Bucs, S., Picioreanu, C., Vrouwenvelder, J., & Ghaffour, N. (2019). Hydrodynamic flow transition dynamics in a spacer filled filtration channel using direct numerical simulation. *Journal of Membrane Science, 590*, 117264. doi:https://doi.org/10.1016/j.memsci.2019.117264

Qasim, M., Badrelzaman, M., Darwish, N. N., Darwish, N. A., & Hilal, N. (2019). Reverse osmosis desalination: A state-of-the-art review. *Desalination, 459*, 59-104. doi:https://doi.org/10.1016/j.desal.2019.02.008

Qing, L., Bilad, M. R., Sun, G., Jaafar, J., & Fane, A. G. (2020). Flow uneven-distribution and its impact on performances of forward osmosis module. *Journal of Water Process Engineering, 33*, 101014. doi:https://doi.org/10.1016/j.jwpe.2019.101014

Qiu, T., & Davies, P. (2012). Comparison of Configurations for High-Recovery Inland Desalination Systems. *Water, 4*, 690. doi:10.3390/w4030690

Quinn, J. C., & Davis, R. (2015). The potentials and challenges of algae based biofuels: A review of the techno-economic, life cycle, and resource assessment modeling. *Bioresource Technology, 184*, 444-452.

Radu, A. I., Bergwerff, L., van Loosdrecht, M. C. M., & Picioreanu, C. (2015). Combined biofouling and scaling in membrane feed channels: a new modeling approach. *Biofouling, 31*(1), 83-100. doi:10.1080/08927014.2014.996750

Radu, A. I., van Steen, M. S. H., Vrouwenvelder, J. S., van Loosdrecht, M. C. M., & Picioreanu, C. (2014). Spacer geometry and particle deposition in spiral wound membrane feed channels. *Water Research, 64*, 160-176. doi:https://doi.org/10.1016/j.watres.2014.06.040

Radu, A. I., Vrouwenvelder, J. S., van Loosdrecht, M. C. M., & Picioreanu, C. (2010). Modeling the effect of biofilm formation on reverse osmosis performance: Flux, feed channel pressure drop and solute passage. *Journal of Membrane Science, 365*(1), 1-15. doi:https://doi.org/10.1016/j.memsci.2010.07.036

Radu, A. I., Vrouwenvelder, J. S., van Loosdrecht, M. C. M., & Picioreanu, C. (2012). Effect of flow velocity, substrate concentration and hydraulic cleaning on biofouling of reverse osmosis feed channels. *Chemical Engineering Journal, 188*, 30-39. doi:https://doi.org/10.1016/j.cej.2012.01.133

Ruiz-García, A., & Pestana, I. N. (2019). Feed spacer geometries and permeability coefficients. Effect on the performance in BWRO spriral-wound membrane modules. *Water (Switzerland), 11*(1). doi:10.3390/w11010152

Ryerson, W. G., & Schwenk, K. (2011). A Simple, Inexpensive System for Digital Particle Image Velocimetry (DPIV) in Biomechanics. *Journal of Experimental Zoology Part A Ecological Genetics and Physiology, 313A*.

Saeed, A., Vuthaluru, R., & Vuthaluru, H. B. (2015). Investigations into the effects of mass transport and flow dynamics of spacer filled membrane modules using CFD. *Chemical Engineering Research and Design, 93*, 79-99. doi:https://doi.org/10.1016/j.cherd.2014.07.002

Saeed, A., Vuthaluru, R., Yang, Y., & Vuthaluru, H. B. (2012). Effect of feed spacer arrangement on flow dynamics through spacer filled membranes. *Desalination, 285*, 163-169.

Santos, J. L. C., Geraldes, V., Velizarov, S., & Crespo, J. G. (2007). Investigation of flow patterns and mass transfer in membrane module channels filled with flow-aligned spacers using computational fluid dynamics (CFD). *Journal of Membrane Science, 305*, 103-117.

Sarai Atab, M., Smallbone, A. J., & Roskilly, A. P. (2016). An operational and economic study of a reverse osmosis desalination system for potable water and land irrigation. *Desalination, 397*, 174-184. doi:https://doi.org/10.1016/j.desal.2016.06.020

Schwinge, J., Neal, P. R., Wiley, D. E., Fletcher, D. F., & Fane, A. G. (2004). Spiral wound modules and spacers: Review and analysis. *Journal of Membrane Science, 242*, 129-153.

Schwinge, J., Wiley, D. E., & Fane, A. G. (2004). Novel spacer design improves observed flux. *Journal of Membrane Science, 229*, 53-61.

Schwinge, J., Wiley, D. E., & Fletcher, D. F. (2002). Simulation of the Flow around Spacer Filaments between Channel Walls. 2. Mass-Transfer Enhancement. *Industrial & Engineering Chemistry Research, 41*, 4879-4888.

Scott, K. (1995). INTRODUCTION TO MEMBRANE SEPARATIONS. In K. Scott (Ed.), *Handbook of Industrial Membranes* (pp. 3-185). Amsterdam: Elsevier Science.

Seader, J. D., & Henley, E. J. (1998). *Separation process principles*. New York: Wiley.

Shakaib, M., Hasani, S. M. F., & Mahmood, M. (2009). CFD modelling for flow and mass transfer in spacer-obstructed membrane feed channels. *Journal of Membrane Science, 326*, 270-284.

Sharma, M., Mondal, P., Chakraborty, A., Kuttippurath, J., & Purkait, M. (2019). Effect of different molecular weight polyethylene glycol on flat sheet cellulose acetate membranes for evaluating power density performance in pressure retarded osmosis study. *Journal of Water Process Engineering, 30*, 100632. doi:https://doi.org/10.1016/j.jwpe.2018.05.011

Sherwood, T. K., Pigford, R. L., & Wilke, C. R. (1975). *Mass transfer*. New York: Mcgraw-Hill.

Shi, B., Marchetti, P., Peshev, D., Zhang, S., & Livingston, A. G. (2017). Will ultra-high permeance membranes lead to ultra-efficient processes? Challenges for molecular separations in liquid systems. *Journal of Membrane Science, 525*, 35-47. doi:https://doi.org/10.1016/j.memsci.2016.10.014

Shrivastava, A., Rosenberg, S., & Peery, M. (2015). Energy efficiency breakdown of reverse osmosis and its implications on future innovation roadmap for desalination. *Desalination, 368*, 181-192. doi:https://doi.org/10.1016/j.desal.2015.01.005

Siddiqui, A., Lehmann, S., Haaksman, V., Ogier, J., Schellenberg, C., van Loosdrecht, M. C. M., . . . Vrouwenvelder, J. S. (2017). Porosity of spacer-filled channels in spiral-wound membrane systems: Quantification methods and impact on hydraulic characterization. *Water Research, 119*, 304-311. doi:https://doi.org/10.1016/j.watres.2017.04.034

Sivertsen, E., Holt, T., Thelin, W., & Brekke, G. (2013). Pressure retarded osmosis efficiency for different hollow fibre membrane module flow configurations. *Desalination, 312*, 107-123. doi:https://doi.org/10.1016/j.desal.2012.11.019

Sreedhar, N., Thomas, N., Al-Ketan, O., Rowshan, R., Hernandez, H., Abu Al-Rub, R. K., & Arafat, H. A. (2018a). 3D printed feed spacers based on triply periodic minimal surfaces for flux enhancement and biofouling mitigation in RO and UF. *Desalination, 425*, 12-21. doi:https://doi.org/10.1016/j.desal.2017.10.010

Sreedhar, N., Thomas, N., Al-Ketan, O., Rowshan, R., Hernandez, H. H., Abu Al-Rub, R. K., & Arafat, H. A. (2018b). Mass transfer analysis of ultrafiltration using spacers based on triply periodic minimal surfaces: Effects of spacer design, directionality and voidage. *Journal of Membrane Science, 561*, 89-98. doi:10.1016/j.memsci.2018.05.028

Su, X., Li, W., Palazzolo, A., & Ahmed, S. (2018). Concentration polarization and permeate flux variation in a vibration enhanced reverse osmosis membrane module. *Desalination, 433*, 75-88. doi:https://doi.org/10.1016/j.desal.2018.01.001

Su, X., Li, W., Palazzolo, A., & Ahmed, S. (2019). Permeate flux increase by colloidal fouling control in a vibration enhanced reverse osmosis membrane desalination system. *Desalination, 453*, 22-36. doi:https://doi.org/10.1016/j.desal.2018.12.003

Suwaileh, W., Pathak, N., Shon, H., & Hilal, N. (2020). Forward osmosis membranes and processes: A comprehensive review of research trends and future outlook. *Desalination, 485*, 114455. doi:https://doi.org/10.1016/j.desal.2020.114455

Tang, C. Y., Chong, T. H., & Fane, A. G. (2011). Colloidal interactions and fouling of NF and RO membranes: A review. *Advances in Colloid and Interface Science, 164*(1), 126-143. doi:https://doi.org/10.1016/j.cis.2010.10.007

Thomas, N., Sreedhar, N., Al-Ketan, O., Rowshan, R., Abu Al-Rub, R. K., & Arafat, H. (2018). 3D printed triply periodic minimal surfaces as spacers for enhanced heat and mass transfer in membrane distillation. *Desalination, 443*, 256-271. doi:10.1016/j.desal.2018.06.009

Thomas, N., Sreedhar, N., Al-Ketan, O., Rowshan, R., Abu Al-Rub, R. K., & Arafat, H. (2019). 3D printed spacers based on TPMS architectures for scaling control in membrane distillation. *Journal of Membrane Science, 581*, 38-49. doi:10.1016/j.memsci.2019.03.039
93

Uppu, A., Chaudhuri, A., & Prasad Das, S. (2019). Numerical modeling of particulate fouling and cake-enhanced concentration polarization in roto-dynamic reverse osmosis filtration systems. *Desalination, 468*, 114053. doi:https://doi.org/10.1016/j.desal.2019.06.019

Usta, M., Anqi, A. E., & Oztekin, A. (2017). Reverse osmosis desalination modules containing corrugated membranes – Computational study. *Desalination, 416*, 129-139. doi:https://doi.org/10.1016/j.desal.2017.05.005

Van der Bruggen, B. (2018). Chapter 2 - Microfiltration, ultrafiltration, nanofiltration, reverse osmosis, and forward osmosis. In P. Luis (Ed.), *Fundamental Modelling of Membrane Systems* (pp. 25-70): Elsevier.

Verma, N., Vaidh, S., Vishwakarma, G. S., & Pandya, A. (2020). Chapter 18 - Antimicrobial nanomaterials for water disinfection. In S. Rajendran, A. Mukherjee, T. A. Nguyen, C. Godugu, & R. K. Shukla (Eds.), *Nanotoxicity* (pp. 365-383): Elsevier.

Vrouwenvelder, J. S., Picioreanu, C., Kruithof, J. C., & van Loosdrecht, M. C. M. (2010). Biofouling in spiral wound membrane systems: Three-dimensional CFD model based evaluation of experimental data. *Journal of Membrane Science, 346*(1), 71-85. doi:https://doi.org/10.1016/j.memsci.2009.09.025

Wei, Q., McGovern, R., & V, J. (2017). Saving energy with an optimized two-stage reverse osmosis system. *Environ. Sci.: Water Res. Technol., 3*. doi:10.1039/C7EW00069C

Werber, J. R., Deshmukh, A., & Elimelech, M. (2016). The Critical Need for Increased Selectivity, Not Increased Water Permeability, for Desalination Membranes. *Environmental Science & Technology Letters, 3*(4), 112-120. doi:10.1021/acs.estlett.6b00050

Wiley, D. E., & Fletcher, D. F. (2002). Computational fluid dynamics modelling of flow and permeation for pressure-driven membrane processes. *Desalination, 145*(1–3), 183-186. doi:10.1016/s0011-9164(02)00406-x

Xie, M., Tang, C. Y., & Gray, S. R. (2016). Spacer-induced forward osmosis membrane integrity loss during gypsum scaling. *Desalination, 392*, 85-90. doi:https://doi.org/10.1016/j.desal.2016.04.017

Xie, P., Murdoch, L. C., & Ladner, D. A. (2014). Hydrodynamics of sinusoidal spacers for improved reverse osmosis performance. *Journal of Membrane Science, 453*, 92-99.

Xu, Y., Peng, X., Tang, C. Y., Fu, Q. S., & Nie, S. (2010). Effect of draw solution concentration and operating conditions on forward osmosis and pressure retarded osmosis performance in a spiral wound module. *Journal of Membrane Science, 348*(1), 298-309. doi:https://doi.org/10.1016/j.memsci.2009.11.013

Yang, Z., Zhou, Y., Feng, Z., Rui, X., Zhang, T., & Zhang, Z. (2019). A Review on Reverse Osmosis and Nanofiltration Membranes for Water Purification. *Polymers, 11*(8), 1252. doi:10.3390/polym11081252

Yazgan-Birgi, P., Hassan Ali, M. I., & Arafat, H. A. (2018). Estimation of liquid entry pressure in hydrophobic membranes using CFD tools. *Journal of Membrane Science, 552*, 68-76. doi:https://doi.org/10.1016/j.memsci.2018.01.061

Zhang, H., Cheng, S., & Yang, F. (2014). Use of a spacer to mitigate concentration polarization during forward osmosis process. *Desalination, 347*, 112-119. doi:https://doi.org/10.1016/j.desal.2014.05.026
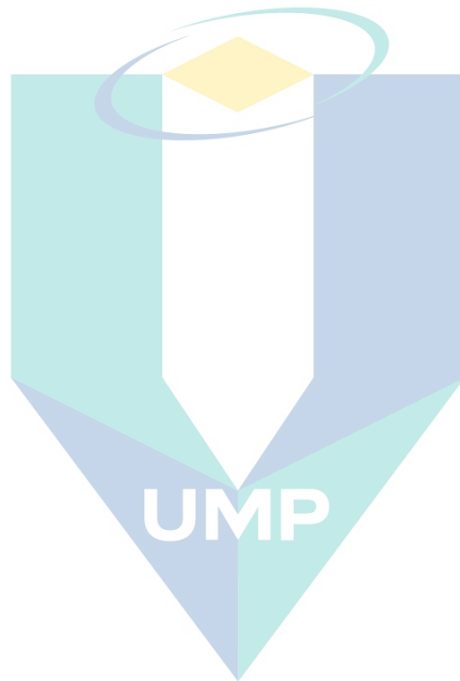
APPENDIX A
FLUX CALCULATION

In order to determine the permeate flux at each point of the SWM module, the CFD data for an impermeable dissolving wall case must first be converted to a permeable membrane case. The permeate mass flux (J) is determined based on the model of Kedem and Katchalsky (1958):

$$u_{y,w} = -\frac{J}{\rho} = -L_p \left(\Delta p_{tm} - \sigma \varphi R_{int} w_w \right) \qquad \text{A.1}$$

The mass balance on the membrane surface relates the permeate flux and mass fraction of solute at both sides of the membrane:

$$J\, w_w = \rho D \left(\frac{\partial w}{\partial y} \right)_w + J\, w_p \qquad \text{A.2}$$

The mass transfer coefficient can also be related with the interplay between the back-diffusion flux and its driving force, the mass fraction difference between the bulk and the membrane surface:

$$k_{mt} = \frac{D}{\left(w_w - w_b \right)} \left(\frac{\partial w}{\partial y} \right)_w \qquad \text{A.3}$$

Combining Equations (A.1-A.3) and the definition of intrinsic rejection (R_{int}) gives a quadratic equation for w_w that can be solved as follows:

$$w_w = w_p + \frac{1}{2\sigma\varphi} \left(\Delta p_{tm} - \frac{k_{mt}}{L_p} \right) + \sqrt{ \left[\frac{1}{2\sigma\varphi} \left(\Delta p_{tm} - \frac{k_{mt}}{L_p} \right) \right]^2 + \frac{k_{mt}}{\sigma\varphi L_p} \left(w_b - w_p \right) } \qquad \text{A.4}$$

where w_p, σ, φ, Δp_{tm}, k_{mt}, L_p and w_b refer to permeate solute concentration, reflection coefficient ($\sigma = 1$), osmotic pressure coefficient ($\varphi = 8.051 \times 10^7$ Pa), transmembrane pressure ($\Delta p_{tm,in} = 6.50$ MPa for seawater; 1.50 MPa for brackish water), mass transfer coefficient for permeable wall, membrane permeance and bulk solute concentration, respectively.
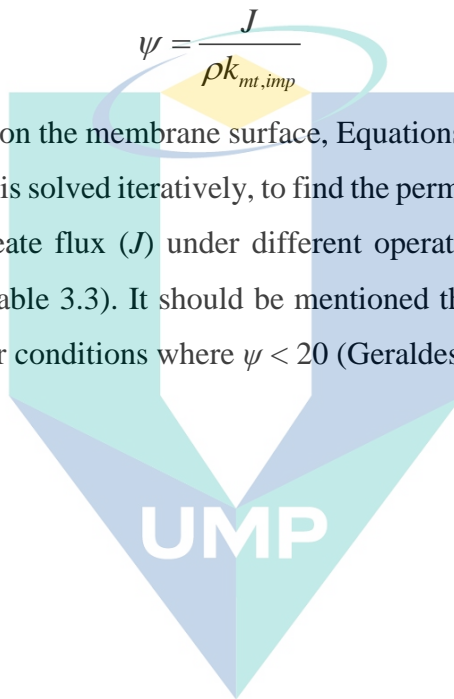
The *Sh_imp* obtained from impermeable wall correlations (Table 3.2) can be used for predicting the flux values for a permeable membrane ($k_{mt,per}$) using the correlation proposed by Geraldes & Afonso (Geraldes & Afonso, 2006):

$$\frac{Sh_{per}}{Sh_{imp}} = \frac{k_{mt,per}}{k_{mt,imp}} = \psi + \left(1 + 0.26\psi^{1.4}\right)^{-1.7} \qquad \text{A.5}$$

where ψ is the ratio of volumetric flux to impermeable mass transfer coefficient:

$$\psi = \frac{J}{\rho k_{mt,imp}} \qquad \text{A.6}$$

For each point on the membrane surface, Equations A.1, A.4, A.5 and A.6 form a non-linear system that is solved iteratively, to find the permeable mass transfer coefficient ($k_{mt,per}$) and the permeate flux (J) under different operating conditions and membrane intrinsic properties (Table 3.3). It should be mentioned that the correlation in Equation A.5 is only valid under conditions where $\psi < 20$ (Geraldes & Afonso, 2006).